UNIVERSITA' DEGLI STUDI "G. d'Annunzio" di Chieti-Pescara

DOTTORATO DI RICERCA IN PROGETTAZIONE ED INGEGNERIA DEL SOTTOSUOLO E DELL'AMBIENTE COSTRUITO - CICLO XXVIII

UNIVERSITAT POLITÈCNICA DE CATALUNYA - BARCELONATECH

DOCTORAT EN ANÀLISI ESTRUCTURAL

Computational Multiscale Analysis of Masonry Structures

Ph.D. Candidate:
Massimo Petracca

Directors:
Prof. Luca Pelà

Prof. Guido Camata

Co-director:
Prof. Riccardo Rossi

Coordinators of the Ph.D. programs:
Prof. Nicola Sciarra

Prof. Miguel Cervera

Academic Years 2013/2015

This page is intentionally left blank

UNIVERSITAT POLITÈCNICA DE CATALUNYA
BARCELONATECH
Escola de Doctorat

Assessment results for the doctoral thesis

Academic year: 2015

Full name: MASSIMO PETRACCA

Doctoral programme: ANÁLISI ESTRUCTURAL

Structural unit in charge of the programme: DECA

Decision of the committee

In a meeting with the examination committee convened for this purpose, the doctoral candidate presented the topic of his/her doctoral thesis entitled

COMPUTATIONAL MULTISCALE ANALYSIS OF MASONRY STRUCTURES.

Once the candidate had defended the thesis and answered the questions put to him/her, the examiners decided to award a mark of:

☐ UNSATISFACTORY ☐ SATISFACTORY ☐ GOOD ☐ VERY GOOD

(Full name and signature) Chairperson		(Full name and signature) Secretary
(Full name and signature) Member	(Full name and signature) Member	(Full name and signature) Member

_____, _____

The votes of the members of the examination committee were counted by the Doctoral School at the behest of the Doctoral Studies Committee of the UPC, and the result is to award the CUM LAUDE DISTINCTION:

☐ YES ☐ NO

(Full name and signature) Chair of the Standing Committee of the Doctoral School	(Full name and signature) Secretary of the Standing Committee of the Doctoral School

Barcelona, _____

This page is intentionally left blank

Contents

List of Figures

List of Tables

This page is intentionally left blank

Acknowledgments

The research presented in this thesis was carried out at the Department of Civil and Environmental Engineering of the Technical University of Catalonia (UPC) and at the Department of Engineering and Geology of the University "G. d'Annunzio" of Chieti-Pescara (UNICH). The two Universities subscribed a co-tutoring agreement, formalizing the international co-tutorship of this Doctoral Thesis.

This research has been primarily possible thanks to the scholarship made available by the UNICH. Additional financial support from the MINECO (Ministerio de Economia y Competitividad of the Spanish Government) through the MULTIMAS project (Multi-scale techniques for the experimental and numerical analysis of the reliability of masonry structures, ref. num. BIA2015-63882-P), the MICROPAR project (Identification of mechanical and strength parameters of structural masonry by experimental methods and numerical micro-modelling, ref num. BIA2012-32234), the EACY project (Enhanced accuracy computational and experimental framework for strain localization and failure mechanisms, ref. MAT2013-48624-C2-1-P), and from the ReLUIS project (Network of Earthquake Engineering Experimental Laboratories, funded by the Prime Minister Office - Civil Protection Department) is acknowledged and greatly appreciated.

These studies were carried out during alternated research stays at the UNICH under the guidance of the Thesis Director Prof. Guido Camata, and at the UPC under the guidance of the Thesis Director Prof. Luca Pelà, and Co-director Prof. Riccardo Rossi. I would like to express my gratitude to all of them. To Prof. Guido Camata for his help during my research and particularly for introducing me to the world of engineering and finite element method, and for proposing to me an international Ph.D.; to Prof. Luca Pelà for his continuous help and guidance during the many steps of my studies, and particularly for sharing with me his knowledge on numerical modeling of masonry structures and constitutive modeling; to Prof. Riccardo Rossi for introducing me to

the open-source Finite Element code Kratos Multiphysics, and for helping me through the implementation of the numerical method proposed in this research. But above all I would like to thank them for being friends and not just professors. I also have to thank Prof. Sergio Oller and Prof. Enrico Spacone for the fruitful suggestions they gave me on many occasions.
Thanks also to Tea Taraborelli, Rosa Maria Olea Sanchis and Rosa Sanchez Haba, for the work spent on the co-tutoring agreement, and to the coordinator of the Ph.D. Program "INGEO" at UNICH, Prof. Nicola Sciarra, and to the coordinator of the Ph.D. Program "Análisis Estructural" at UPC, Prof. Miguel Cervera.
I would also like to thank all the friends I met in Barcelona, particularly Stefano, Savvas and Lorenzo, and all my friends in Italy. A special thanks goes out to my family and my wife's family, Francesco, Loredana, Michele, Marta, Franco, Maria, Luigi, Cinzia, Valentino e Gina. But above all I have to express my gratitude to my dear wife Elena, who, patiently and lovingly, took care of our children Alessio, Lorenzo, Marco and Arianna, during my long stays in Spain.

Abstract

Masonry is an ancient building material that has been used throughout the history, and it is still used nowadays. Masonry constitutes the main building technique adopted in historical constructions, and a deep understanding of its behavior is of primary importance for the preservation of our cultural heritage.
Despite its extensive usage, masonry has always been used following a trial and error approach and rules-of-thumb, due to a poor understanding of the complex mechanical behavior of such a composite material.
Advanced numerical methods are therefore attractive tools to understand and predict the behavior of masonry up to and including its complete failure, allowing to estimate the residual strength and safety of structures. Several numerical methods have been proposed in recent years, either based on a full micro-modeling of masonry constituents, or on phenomenological macro models. In-between these two approaches, computational homogenization techniques have recently emerged as a promising tool joining their advantages. The problem is split into two scales: the structural scale is treated as an equivalent homogeneous medium, while the complex behavior of the heterogeneous micro-structure is taken into account solving a micro-scale problem on a representative sample of the micro-structure.
The aim of this research is the development of a computational multiscale homogenization technique for the analysis of masonry structure, subjected to quasi-static in-plane and out-of-plane loadings. Classical Cauchy continuum theory is used at both scales, thus using the so-called first order computational homogenization. Due to the brittle nature of masonry constituents, particular attention is given to the problem of strain localization. In this context, the present research proposes an extension of the fracture-energy-based regularization to the two-scale homogenization problem, allowing the use of first order computational homogenization in problems involving strain localization.

The method is first stated for the standard continuum case, and it is applied to the two-dimensional analysis of in-plane loaded shear walls made of periodic brick masonry. Then, the aforementioned method is extended to the case of shell structures for the analysis of out-of-plane loaded masonry walls. For this purpose, a novel homogenization technique based on thick shell theory is developed. Both in the in-plane and in the out-of-plane loading conditions, the accuracy of the proposed method is validated comparing it with experimental evidences and with micro-model analyses. The regularization properties are also assessed.

The obtained results show how computational homogenization is an ideal tool for an accurate evaluation of the structural response of masonry structures, accounting for the complex behavior of its micro-structure.

Resumen

La obra de fábrica es un material de construcción tradicional que ha sido utilizado a lo largo de la historia y que sigue siendo utilizado hoy en día. La obra de fábrica constituye la principal técnica de construcción adoptada en estructuras históricas, y una comprensión profunda de su comportamiento es de vital importancia para la conservación de nuestro patrimonio cultural.

A pesar de su amplio uso, la obra de fábrica ha sido utilizada frecuentemente adoptando un enfoque empírico, debido a un escaso conocimiento del comportamiento mecánico complejo de este tipo de material compuesto.

Los métodos numéricos avanzados son herramientas atractivas para entender y predecir el comportamiento de la obra de fábrica hasta su fallo, permitiendo estimar la resistencia residual y la seguridad de las estructuras. Durante los últimos años, han sido propuestos diferentes modelos computacionales, basados bien en una micro-modelización completa de los constituyentes del material (ladrillos y juntas de mortero), o bien en macro-modelos fenomenológicos. A partir de estos dos enfoques, los métodos de homogenización computacional han emergido recientemente como una herramienta prometedora que puede combinar las ventajas de la micro- y macro-modelización. El problema se divide en dos pasos: la escala estructural se trata como un medio homogéneo equivalente, mientras el comportamiento complejo de la microestructura heterogénea se tiene en cuenta mediante la resolución de un problema micro-mecánico reconducible a una muestra representativa de la microestructura.

El objetivo de esta investigación es el desarrollo de una técnica de homogenización computacional multi-escala para el análisis de estructuras de obra de fábrica sometidas a cargas horizontales cuasi-estáticas que actúan en el plano y fuera del plano. Se adopta la teoría clásica del medio continuo de Cauchy en ambas las escalas, utilizando así la homogeneización computacional del primer orden. Debido a la naturaleza frágil de los

componentes de la obra de fábrica, el estudio contempla también el problema de la localización de la deformación en el marco del enfoque numérico de fisura distribuida. En este contexto, la presente investigación propone una extensión de la regularización basada en la energía de fractura para el problema de homogenización en dos escalas, permitiendo el uso de la homogenización computacional del primer orden en problemas que implican la localización de la deformación.

El método se plantea en primer lugar para el caso continuo general, y a continuación se aplica al análisis de muros de corte cargados en su plano y hechos de fábrica de ladrillos con aparejo periódico. Posteriormente, el método se extiende al caso de estructuras tipo placa para el análisis de muros de obra de fábrica cargados fuera de su plano. Para este propósito, se desarrolla una nueva técnica de homogenización basada en la teoría de placas gruesas. En ambos los casos de carga en el plano y fuera del plano, la precisión del método propuesto se valida mediante la comparación con ensayos experimentales y análisis de micro-modelización. También se validan las propiedades de regularización.

Los resultados obtenidos muestran cómo la homogeneización computacional pueda resultar una herramienta válida para una evaluación precisa de la respuesta estructural de las estructuras de obra de fábrica, teniendo en cuenta el comportamiento complejo de la micro-estructura.

Sommario

La muratura è un antico materiale da costruzione che è stato utilizzato in special modo nel corso della storia, ma che è ancora oggi piuttosto diffuso. La muratura è la tecnica principale di costruzione adottata in edifici storici, e una profonda comprensione del suo comportamento è di vitale importanza per la conservazione del nostro patrimonio culturale.
Nonostante il suo ampio utilizzo, la muratura è sempre stata utilizzata seguendo un approccio empirico, a causa di una scarsa comprensione del complesso comportamento meccanico di tale materiale composito.
I metodi numerici avanzati sono, quindi, strumenti attraenti per studiare e comprendere il comportamento della muratura fino al suo collasso, permettendo di stimare la resistenza residua e la sicurezza delle strutture. Diversi metodi numerici sono stati proposti negli ultimi anni, basati o sulla completa micro-modellazione dei componenti della muratura (mattoni e giunti di malta), o su macro-modelli fenomenologici. A metà strada tra questi due approcci, le tecniche di omogeneizzazione computazionale sono emerse recentemente come uno strumento promettente che unisce i vantaggi della micro- e macro-modellazione. Il problema viene diviso in due scale: la scala strutturale viene trattata come un mezzo omogeneo equivalente, mentre il complesso comportamento della microstruttura eterogenea viene preso in considerazione risolvendo un problema di micro-scala su un volume rappresentativo della microstruttura.
Lo scopo di questa ricerca è lo sviluppo di una tecnica di omogeneizzazione computazionale multiscala per l'analisi di strutture in muratura, sottoposte a carichi orizzontali quasi-statici agenti nel piano e fuori dal piano. La teoria classica del continuo di Cauchy è adottata in entrambe le scale, utilizzando quindi la cosiddetta omogeneizzazione computazionale del primo ordine. A causa della natura fragile dei costituenti della muratura, particolare attenzione viene dedicata al problema della local-

izzazione delle deformazioni nel modello numerico a danneggiamento distribuito. In questo contesto, la presente ricerca propone un'estensione della regolarizzazione basata sull'energia di frattura al problema di omogeneizzazione a due scale, permettendo l'uso dell'omogeneizzazione computazionale di primo ordine in problemi che coinvolgono localizzazione delle deformazioni.

Il metodo viene prima impostato per il caso continuo generale, e viene in seguito applicato all'analisi bidimensionale di pareti a taglio, caricate nel piano, fatte di muratura di mattoni a disposizione periodica. Poi, il suddetto metodo viene esteso al caso di strutture tipo piastra per l'analisi di pareti in muratura caricate fuori dal piano. A questo scopo, si sviluppa una nuova tecnica di omogeneizzazione basata sulla teoria delle piastre spesse. In entrambi i casi di carico nel piano e fuori dal piano, l'accuratezza del metodo proposto è validata mediante il confronto con evidenze sperimentali e con analisi di micro-modellazione. Allo stesso modo, le proprietà di regolarizzazione vengono validate.

I risultati ottenuti evidenziano come l'omogeneizzazione computazionale sia uno strumento valido per una valutazione accurata della risposta strutturale delle strutture in muratura, tenendo conto del comportamento complesso della sua microstruttura.

This page is intentionally left blank

Chapter 1

Introduction

This chapter gives a brief introduction to numerical modeling of masonry structures, highlighting the motivation and objectives of the present research, as well as the organization of the thesis. Section 1.1 briefly reports the background in numerical modeling of masonry structures, pointing out the motivations for the present research. Section 1.2 explains the principal features of the masonry "material". Section 1.3 gives a review on the state-of-the-art of micro-modeling techniques for the analysis of masonry structures, in order to identify the available discretization techniques and constitutive models for masonry constituents. Section 1.4 gives a review on computational homogenization methods, with special focus on the issues related to the modeling of brittle materials, and the recently proposed methods to overcome these issues.

1.1 Background and motivation

Masonry is an ancient building material that have been extensively used throughout the history, and it is still used nowadays. Being the main building technique adopted in historical constructions, a deep understanding of masonry mechanical behavior is therefore of primary importance for the preservation of our cultural heritage. However, despite its extensive usage, masonry has always been used following a trial and error approach and rules-of-thumb. This is mainly due to the poor understanding of the complex mechanical behavior of such a composite material: Masonry can be considered a composite material, with a micro-structure consisting of units (bricks or stones) and joints, with or without mortar. These micro-structural constituents, their very different

elastic and inelastic properties, and their arrangement, lead to very complex behaviors and different failure mechanisms. The evolution of the structural response is highly influenced by the complex behavior of micro-structural phenomena such as damaged-induced anisotropy, stress redistribution among micro-structural constituents or strain localization. Advanced numerical methods are therefore attractive tools to understand and predict the behavior of masonry up to its complete failure, allowing to estimate the residual strength and safety of structures.

Several computational strategies were proposed to deal with the numerical analysis of such a complex material Roca et al. (2010). Macro-models were developed to study masonry structures. The most recent macro-models regard the material as a fictitious homogeneous orthotropic continuum, without making any distinction between units and joints in the discrete model Pelà et al. (2011, 2013, 2014b). This approach presents some intrinsic difficulties mainly related to the identification of the mechanical parameters of the continuum and the definition of realistic phenomenological failure criteria. It is particularly difficult to take into account the influence of the evolving micro-structure on the macroscopic properties, especially when strain localizations occur in the micro-structure leading to complex dissipation mechanisms at the structural level. However, macro-models are still a suitable option for the numerical analysis of large and complex structures (see Figure 1.1, Figure 1.2) due to their limited computational cost Endo et al. (2015), Saloustros et al. (2015b), Pelà et al. (2014a), Roca et al. (2013, 2012), Pelà (2009).

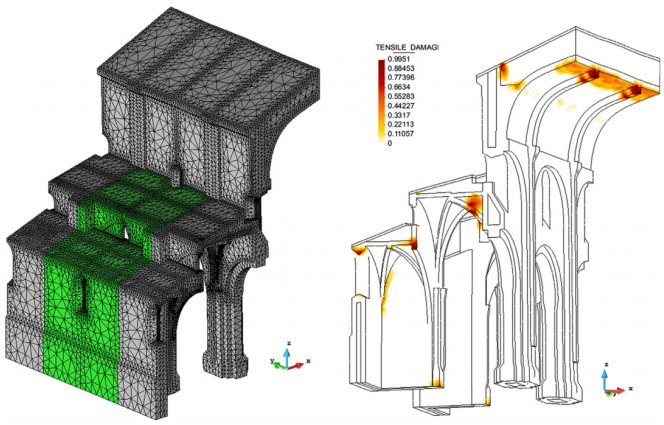

Figure 1.1: Simulation of the demolition of the southern aisle of the Poblet Monastery, from Saloustros et al. (2015b)

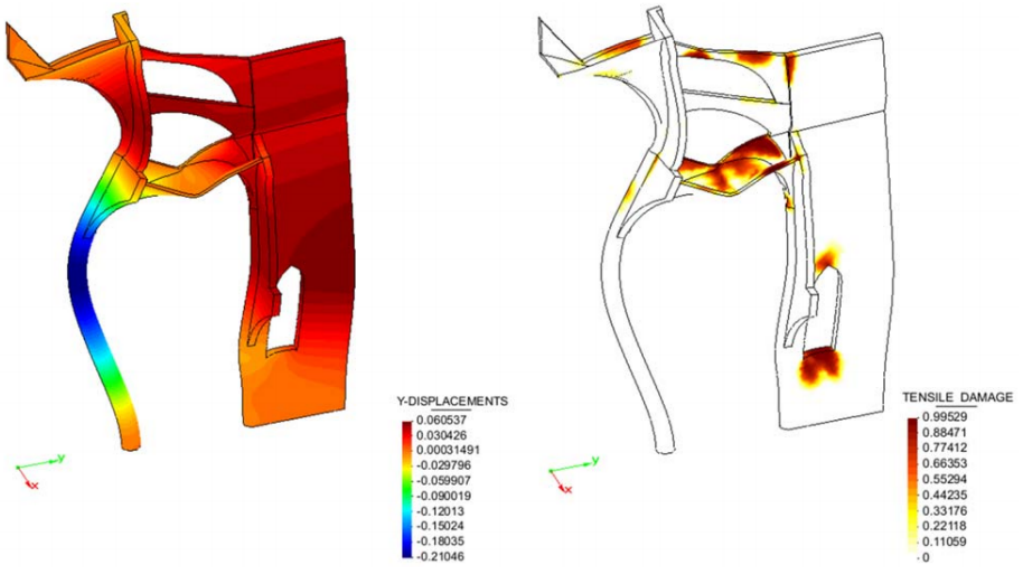

Figure 1.2: Mallorca Cathedral. FE simulation of long-term deformation. Deformed shape and tensile damage, from Pelà et al. (2014a)

Very popular approaches used nowadays to study masonry, including its heterogeneous micro-structure in the discretization, are micro/meso-modeling Lourenço and Rots (1997), Lourenço (1996), Oliveira and Lourenço (2004), Drougkas et al. (2014), Citto (2008), Gambarotta and Lagomarsino (1997), Raffa et al. (2013), Sacco and Toti (2010), Lotfi and Shing (1994). In these approaches, the complete micro-structure (or a simplified version of it) is directly modeled, thus the complex interaction between the masonry constituents is naturally taken into account. However, this requires a complex model generation and high computational costs. Therefore they are suitable to model in detail small structural members, but their usage soon becomes unaffordable for large scale structures.

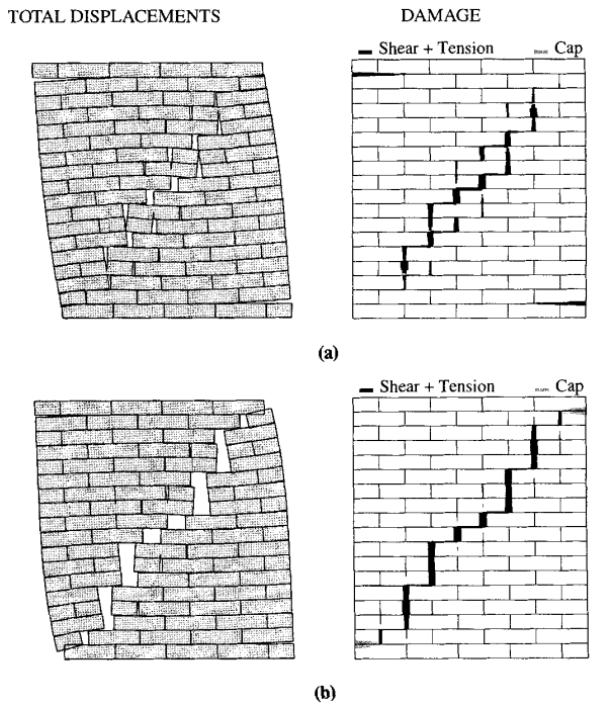

Figure 1.3: Micro-modeling simulation of a shear wall, from Lourenço and Rots (1997)

In-between macro- and micro-modeling techniques, computational homogenization techniques recently emerged as a promising tool joining their advantages Addessi et al. (2010), Bosco et al. (2015), De Bellis (2009), De Bellis and Addessi (2011), De Souza Neto and Feijóo (2006), Geers et al. (2003), Hernández et al. (2012), Kouznetsova et al. (2004, 2002), Massart (2003), Massart et al. (2007), Mercatoris et al. (2009), Mercatoris and Massart (2011), Oliver et al. (2014b,c,a), Oller et al. (2005), Ortolano et al. (2013), Otero et al. (2012, 2015), Badillo (2012), Quinteros et al. (2012), Trovalusci and Masiani (2003), Zucchini and Lourenço (2002, 2009). The problem is split into two scales: The structural scale is treated as an equivalent homogeneous medium, while the complex behavior of the heterogeneous micro-structure is taken into account solving a micro-scale problem on a representative sample of the micro-structure (see Figure 1.4, Figure 1.5). Although very attractive, classical homogenization procedures are known to behave poorly when strain localization occurs in the micro-structure, and thus they need to be adapted to be used in such a context.

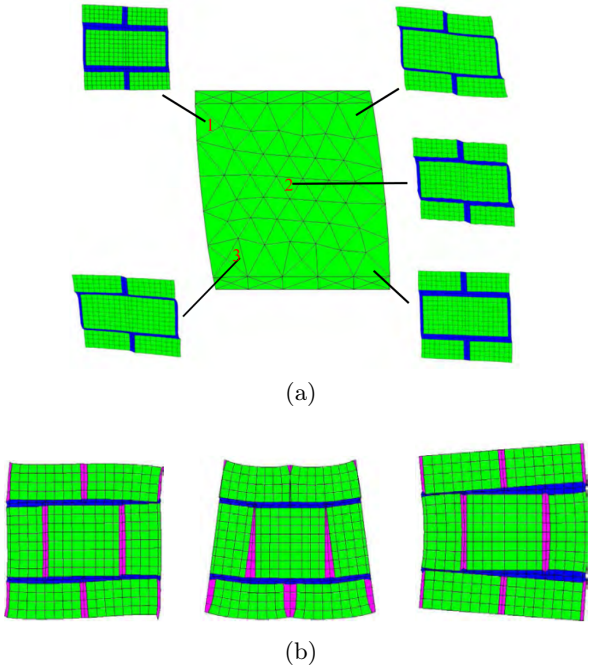

(a)

(b)

Figure 1.4: (a) Cosserat-based computational homogenization analysis of a shear wall, and (b) Cosserat additional deformation modes, from De Bellis (2009)

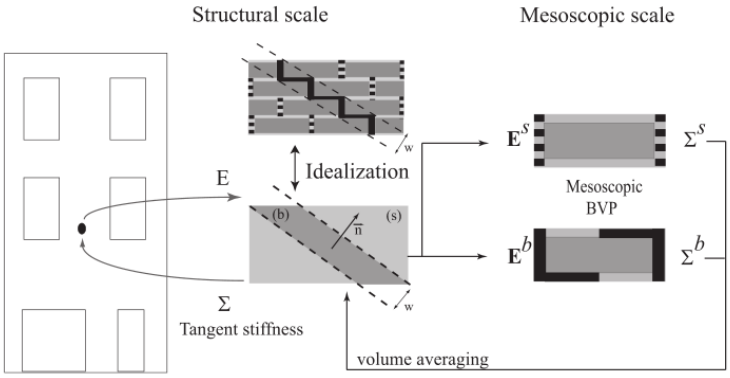

Figure 1.5: Enhanced first-order multi-scale scheme with embedded strain discontinuity for localized behavior, from Massart (2003)

1.2 Mechanical behavior of masonry

Masonry is a heterogeneous material made of units and joints, characterized by a large variety (see Figure 1.6) in geometry, nature, arrangement of units and characteristics of mortars.

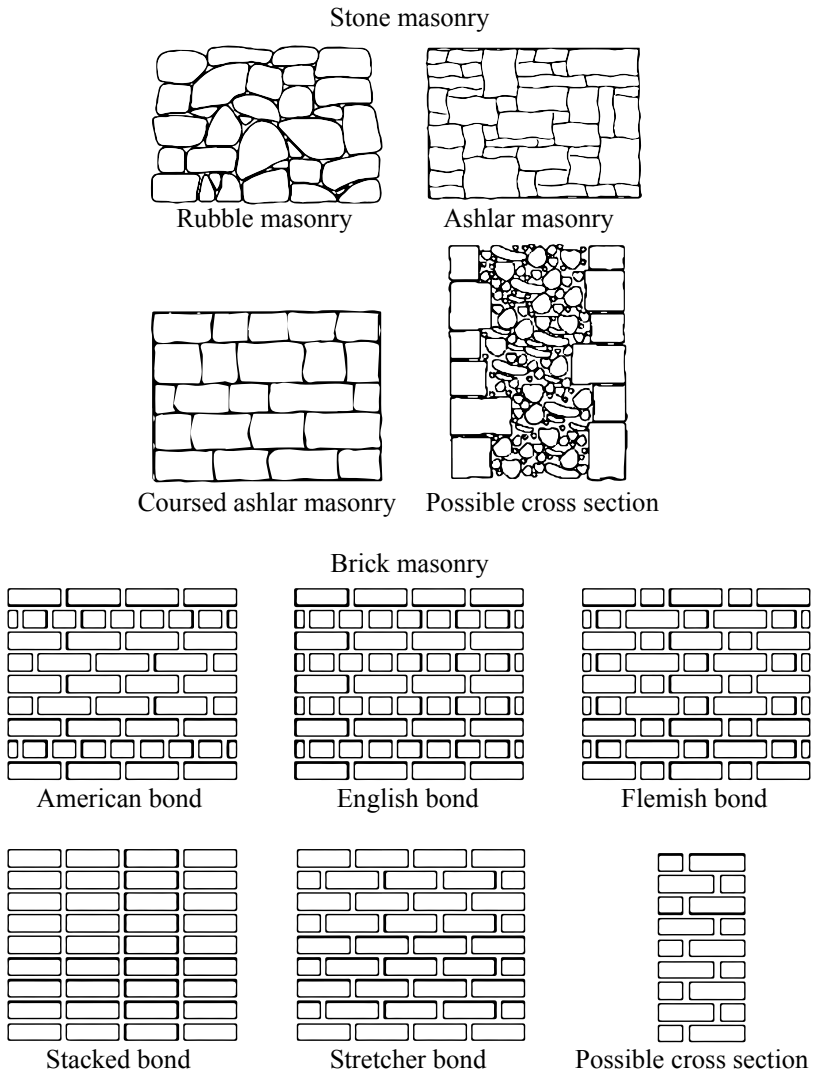

Figure 1.6: Variability of stone and brick masonry

Despite the large number of typologies, the overall mechanical behavior shows several recurrent features that will be briefly recalled here, while for further details the reader is referred to Drysdale et al. (1994) and Hendry (1990). From a phenomenological point of view, masonry can be considered as a composite material with an overall orthotropic behavior. The orthotropy in the elastic response is related to the different elastic mechanical properties of mortar and units as well as their geometrical arrangement. Moreover, mortar joints typically act as weak planes, and the structural response is strongly dependent on their orientation.

The uniaxial compressive strength of masonry in the direction normal to the bed joints has been traditionally regarded as the most relevant structural material property. Uniaxial compression tests in the direction parallel to the bed joints received less attention from the masonry community. However, masonry is an anisotropic material and, particularly in the case of low longitudinal compressive strength of the units due to high perforation, the resistance to compressive loads parallel to the bed joints can have a decisive effect on the load bearing capacity.

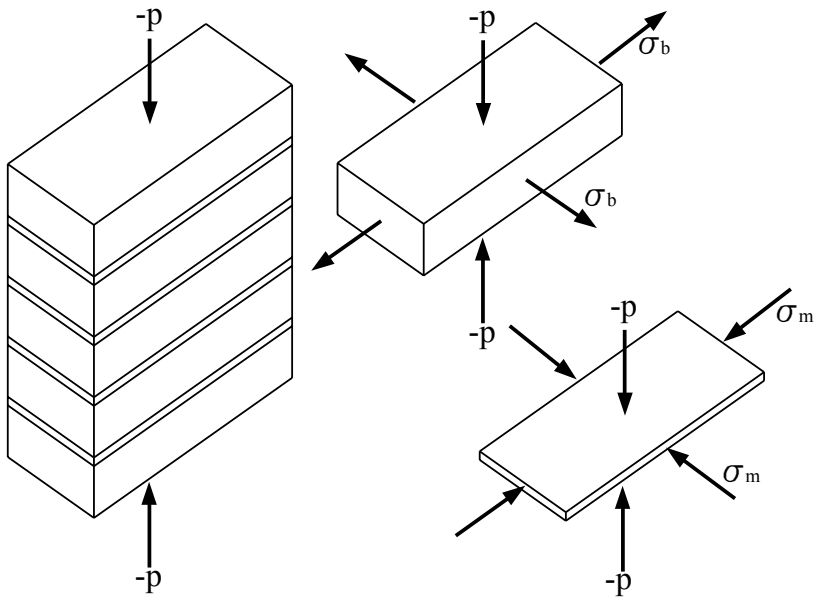

Figure 1.7: Local state of stress in masonry prisms under vertical compression

Hilsdorf (1969) demonstrated that the significant difference in elastic properties of units and mortar is the precursor of failure. When mortar is substantially softer than units, as it typically happens, the uniaxial compression of masonry in direction perpendicular to bed joints leads to a state of triaxial compression in the mortar and of compression/biaxial tension in the unit, see Figure 1.7. Units confine the mortar layer avoiding its lateral expansion, and, as a consequence, vertical cracks appear in the units. Upon increasing deformation, additional vertical cracks appear, finally leading to the collapse. The strength and the failure mode change with different inclinations of bed joints Samarasinghe and Hendry (1982), Page (1981, 1983) because of the anisotropic nature of the material. If loading direction is parallel to bed joints, the splitting of the bed joints in tension occurs. For intermediate inclinations, a mixed mechanism is encountered, see Figure 1.8.

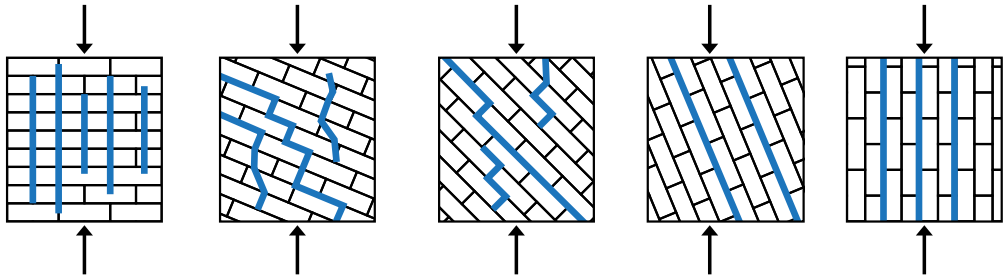

Figure 1.8: Local state of stress in masonry prisms under vertical compression, from Page (1981, 1983)

For tensile loading perpendicular to the bed joints, failure is generally caused by debonding between the bed joint and the unit. In this case, the masonry tensile strength can be considered equal to the tensile bond strength between the joint and the unit. On the contrary, in masonry with low strength units and high tensile bond strength between the bed joint and the unit, e.g. high-strength mortar and units with numerous small perforations, which produce a dowel effect, failure may occur as a result of stresses exceeding the unit tensile strength. In this case, the masonry tensile strength in this case can be considered equal to the tensile strength of the unit. For tensile loading parallel to the bed joints a complete test program was set-up by Backes (1985). The author tested masonry wallets under direct tension finding that tension failure was affected by

the type of the mortar and the masonry units. For stronger mortar and weaker masonry units, the tension cracks passed along the head mortar joints and through the center of the bricks at the intervening courses, as shown in Figure 1.9a. For weaker mortar and stronger masonry units, the tension crack passed along the head joints of the masonry units and along the portion of bed joints interconnecting the head joints, as shown in Figure 1.9b.

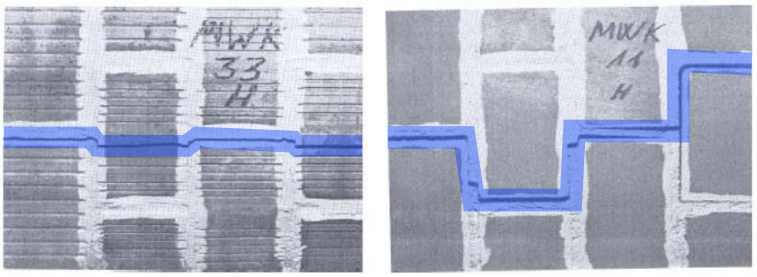

(a) (b)

Figure 1.9: Failure modes of masonry walls under direct tension, from Backes (1985): through type (a), zigzag type (b).

Figure 1.10shows the different failure modes obtained by Page (1983) on solid clay units masonry walls subjected to uniaxial tension. For intermediate inclinations of bed joints, the failure is concentrated on joints.

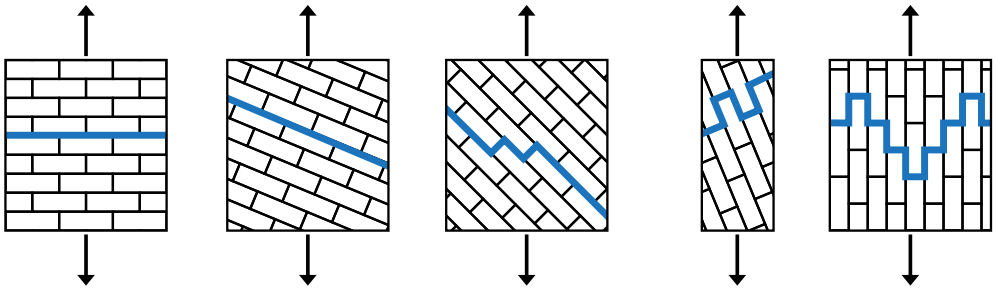

Figure 1.10: Failure modes of solid clay units masonry under uniaxial tension, from Page (1983)

The constitutive behavior of masonry under biaxial stress states is somehow more complex, and it cannot be completely deduced from the constitutive behavior under uniaxial loading conditions. The biaxial strength envelope cannot be described solely in terms of principal stresses, because masonry is an anisotropic material. The biaxial failure surface of masonry must be either described in terms of the full stress vector in a fixed set of material axes or, in terms of principal stresses and the rotation angle θ between the principal stresses and the material axes. A complete set of experimental data of masonry subjected to proportional biaxial loading was provided by Page (1981, 1983), see Figure 1.11. The tests were carried out with half scale solid clay units. Both the orientation of the principal stresses with respect to the material axes and the principal stress ratio considerably influenced the failure mode and strength.

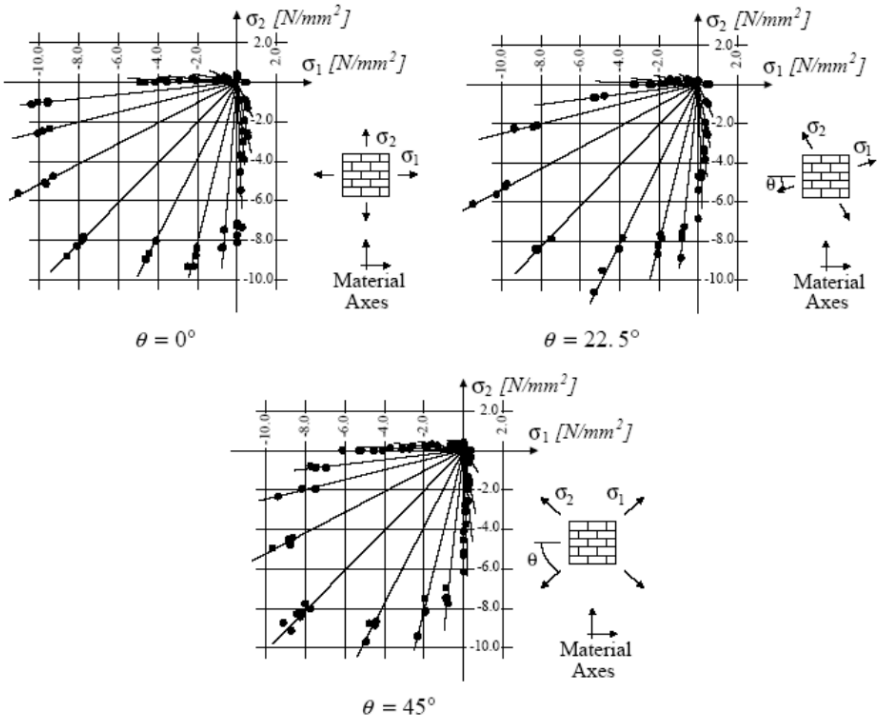

Figure 1.11: Biaxial strength of solid clay units masonry, from Page (1981, 1983).

The influence of the lateral tensile stress in the tensile strength is not known because no experimental results are available. A lateral compressive stress decreases the tensile strength. The minimum value is attained when tension direction is perpendicular to the bed joints. In tension-compression Page (1983), the failure occurs either by cracking and sliding of the joints or in a combined mechanism involving both units and joints, see Figure 1.12.

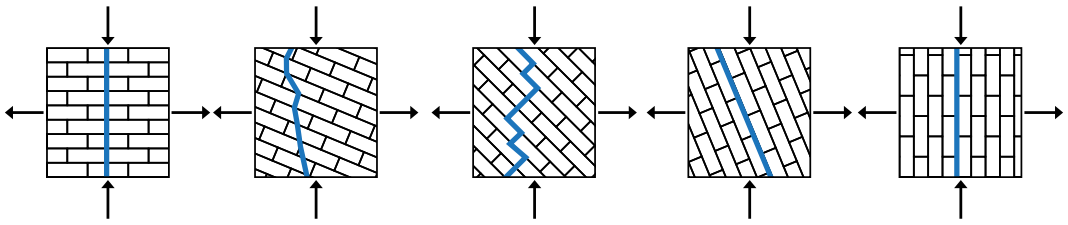

Figure 1.12: Failure modes of solid clay units masonry under biaxial tension-compression, from Page (1983).

In biaxial compression, failure typically occurs by splitting of the specimen at mid-thickness, in a plane parallel to the external free surfaces, regardless of the orientation of the principal stresses, see Figure 1.13. The orientation of principal stresses plays an important role when the compression in one direction is much greater than the compression in the perpendicular direction. In this case, failure occurs in a combined mechanism involving both joint failure and lateral splitting. Increasing compressive strength under biaxial compression can be explained by friction in the joints and internal friction in the units and mortar. It is further noted that the strength envelope shown in Figure 1.11 is of limited applicability for other types of masonry. Different strength envelopes and different failure modes can be found for different materials, unit shapes and geometry. Comprehensive programs to characterize the biaxial strength of different masonry types were carried using full scale specimens in Ganz and Thürlimann (1982) for hollow clay units masonry, in Guggisberg and Thürlimann (1987) for clay and calcium-silicate units masonry and in Lurati et al. (1990) for concrete units masonry.

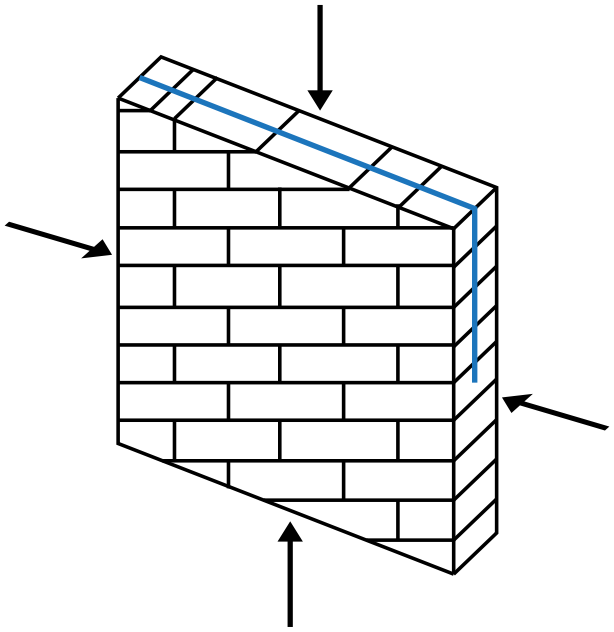

Figure 1.13: Failure modes of solid clay units masonry under biaxial compression-compression, from Page (1981).

As regarding the shear strength of masonry, it can be observed that the determination of the shear response of masonry joints is a complex task, since it depends on the ability of the test set-up to generate a uniform state of stress in the joints. Different test configurations are possible, and the reader is referred to Pluijm (1993, 1998), Hofmann and Stockl (1986), Atkinson et al. (1989) for further details on this subject. Obviously, the shear strength increases with the confining compression stress, because of the frictional behavior of masonry. Moreover, the real behavior of a joint is generally non-associative, i.e. $\delta_n \neq \delta_t \tan\phi$, where δ_n and δ_t are respectively the normal and tangential relative displacements between sliding surfaces of a masonry joint, and ϕ is the angle of friction. Experimental evidence indicates that the real joint behavior is quite complex, with the amount of dilatancy being dependent on the micro-scale geometrical and mechanical features of the masonry joint van Zijl (2004). A recurrent behavior is the reduction of dilatancy angle both with increasing relative tangential displacement, as a consequence of progressive smoothing of asperities, and also under the action of increasing normal stresses, see Figure 1.14.

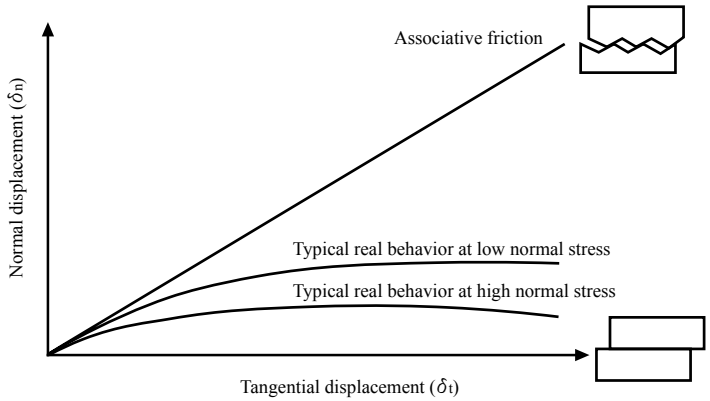

Figure 1.14: Masonry joint behavior: associative idealisation and typical real behaviors

A characteristic feature of masonry is the softening behavior, which is typical of quasi-brittle materials. Softening describes a progressive loss of strength upon increasing deformation, and it is due to a process of growing of internal crack. Such mechanical behavior is commonly related to the heterogeneity of the material, due to the presence of different phases and material defects, like flaws and voids. Even prior to loading, mortar contains micro-cracks due to shrinkage during curing and due to the presence of the aggregates. Likewise, clay bricks contain inclusions and micro-cracks due to the shrinkage during the burning process. The initial stresses and cracks as well as variations of internal stiffness and strength cause progressive crack growth when the material is subjected to progressive deformation. Initially, the micro-cracks are stable, growing only as the load increases. Around the peak load an acceleration of crack formation takes place and the formation of macro-cracks starts. The macro-cracks are unstable, i.e. the load has to decrease to avoid their uncontrolled growth. In a deformation controlled test the macro-crack growth results in softening and localization of cracking in a small zone while the rest of the specimen unloads. Figure 1.15 shows characteristic stress-displacement diagrams for quasi-brittle materials in uniaxial tension, uniaxial compression and pure shear. The integral of the $\sigma - \delta$ diagram is the fracture energy , denoted by G_f and G_c , for tension and compression, respectively. In case of mode II failure mechanism, i.e. slip of the unit-mortar interface under shear loading, the inelastic behavior in shear can be described by the mode II fracture energy $G_{II,f}$, defined by the integral of the $\tau - \delta$ diagram.

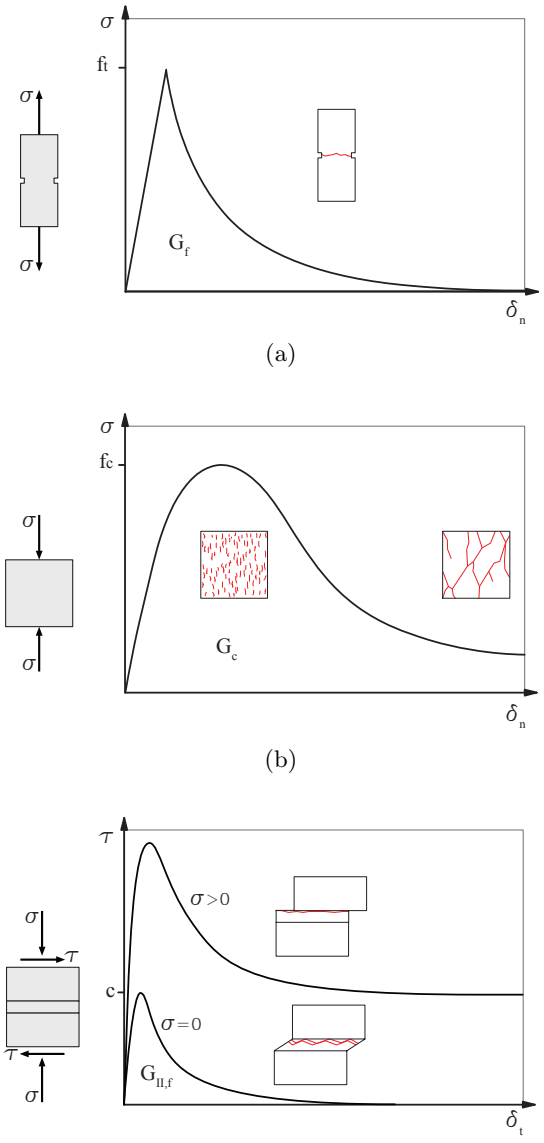

Figure 1.15: Typical behavior of quasi-brittle materials and definition of fracture energy: uniaxial tensile loading (a); uniaxial compressive loading (b); shear (c), from Lourenço (1996).

1.3 Micro-modeling

Micro/Meso-modeling techniques are very popular approaches used nowadays for the detailed analysis of single structural members Lourenço and Rots (1997), Lourenço (1996), Oliveira and Lourenço (2004), Drougkas et al. (2014), Citto (2008), Gambarotta and Lagomarsino (1997), Raffa et al. (2013), Sacco and Toti (2010), Lotfi and Shing (1994). In these approaches, all the information about the micro-structure is explicitly modeled, thus the complex interaction between the masonry constituents is naturally taken into account. These modeling techniques are very useful to understand the local behavior of structural members (see Figure 1.17, Figure 1.18), as opposed to macro-models that are generally preferred in large-scale time-consuming simulations. A complete and detailed description of masonry micro-structure would require the full three-dimensional discretization of bricks, mortar joints, and the interface between them (Figure 1.16a). In this way all masonry constituents and their complex interaction are explicitly accounted for. This modeling strategy is referred to as detailed micro-modeling. However, this requires a complex model generation and high computational costs.

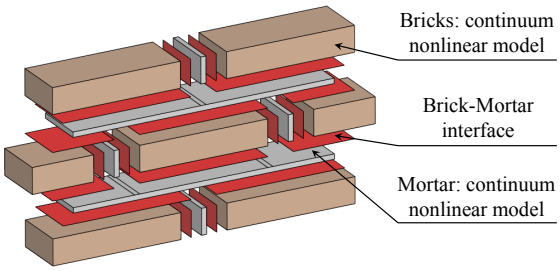

(a) Detailed micro-model

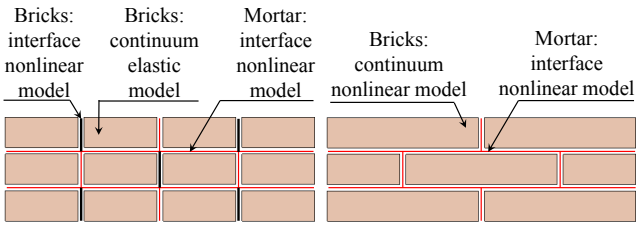

(b) simplified micro-model (c) simplified micro-model

Figure 1.16: Typical masonry modeling strategies

One of the first approaches to simulate the cracking of masonry can be traced back to the work of Page Page (1978, 1982), where a non-linear interface elements was used to represent mortar joints, accounting for high compressive strength, low tensile strength and limited shear strength dependent on the level of compression and the bond strength of the composite material. For the bricks, linear-elastic continuum finite elements were used. The non-linear stress-strain relationships, as well as the failure criteria, were derived by experimental tests carried out by the author. This model was used to reproduce an in-plane bending test on a deep masonry beam under vertical load.
A widely used interface constitutive model was proposed in Lourenço (1996), Lourenço and Rots (1997). The interface constitutive model is formulated in the framework of multisurface plasticity. The composite surface consists of a tensile cut-off to simulate the tensile failure of the mortar joints, a Coulomb's friction law for the shear response of the mortar joints, and an elliptical cap to simulate the compressive crushing of the whole masonry, and the combined shear-compression failure of joints and units due to shear under high compressive stresses. In this way all the non-linearity of mortar joints and mortar-unit interaction is lumped into a single interface element. Units are modeled as an elastic continuum. The only failure mode not taken into account by the interface model is the tensile splitting of the units. To achieve this, the author proposed to include a single potential crack in the units via an extra interface element (Figure 1.16b). This modeling approach is referred to as simplified micro-modeling. Alternatively, units can be modeled as a continuum equipped with an appropriate nonlinear constitutive model, without making assumptions on the cracks in the units (Figure 1.16c).

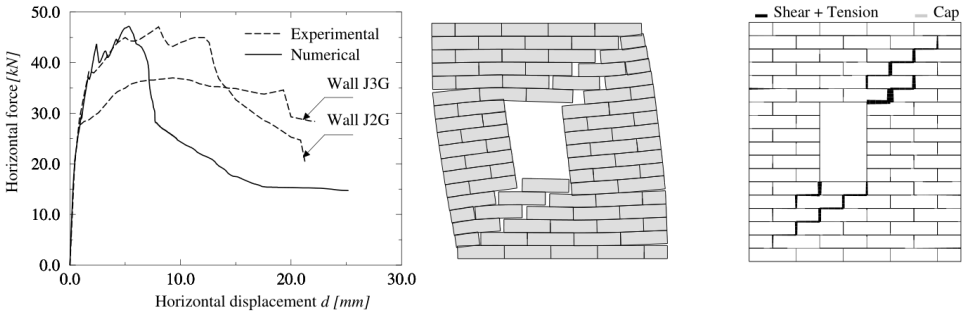

Figure 1.17: Micro-modeling of a shear wall with opening, from Lourenço (1996)

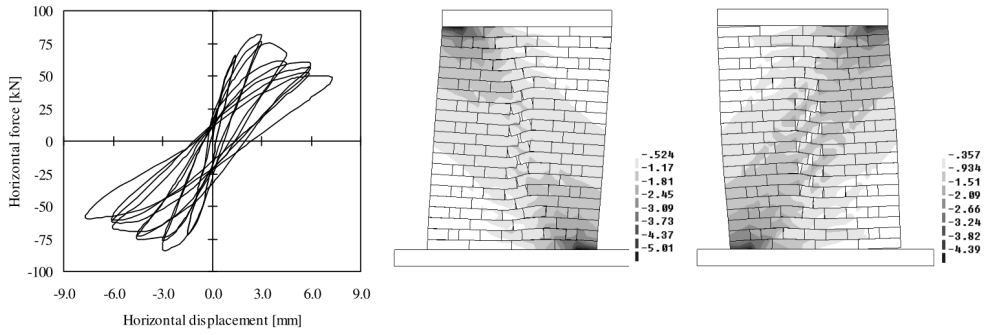

(a)

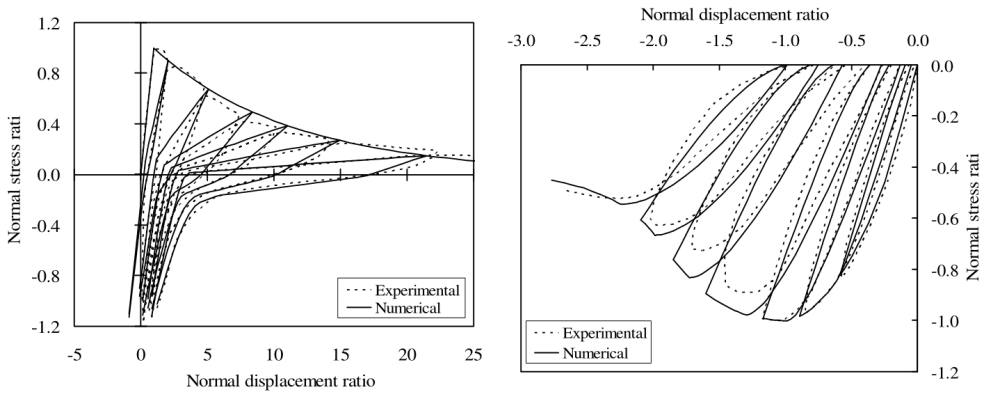

(b)

Figure 1.18: Micro-modeling of a shear wall under cyclic loading, from Oliveira and Lourenço (2004)

1.4 Multiscale methods and computational homogenization

In the context of macro-modeling, the formulation of phenomenological closed-form constitutive laws for the analysis of heterogeneous quasi-brittle materials such as masonry is still a challenging task Pelà et al. (2011, 2013). The evolution of macroscopic properties is highly influenced by the complex behavior of micro-structural phenomena such as damaged-induced anisotropy, stress redistribution among micro-structural constituents or strain localization. In this context, it is difficult to take into account the influence of the evolving micro-structure on the macroscopic properties, especially when strain localizations occur in the micro-structure leading to complex dissipation mechanisms at

the structural level. On the contrary, micro-model simulations, also known as Direct Numerical Simulation (DNS), use a classical 1-scale FE model, and all the information about the micro-structure is explicitly modeled. This method provides the best accuracy in taking into account the micro-structure influence on the structural behavior. However, when dealing with large-scale analysis, the computational cost soon becomes unaffordable, as well as the effort required to prepare the geometrical model.

In the last decades, with the ever-growing computational power, multiscale methods became very popular in the simulation of material with complex micro-structure. These methods take into account, to different extents and in different ways, all the relevant length scales the analyst is interested in. Multiscale methods can be seen as an intermediate approach between standard macro-modeling and micro-modeling. Computational multiscale methods can be roughly grouped into two classes:

A first approach is known as Concurrent Multiscale Method (CMM). As a multiscale model, it involves the study of multiple length scales as well as the exchange of information among them. In this particular approach the micro-structural scale is adaptively inserted and resolved on the structural model, thus establishing a strong coupling between macro and micro scales (see Figure 1.19). Works on this subject can be found in Lloberas-Valls et al. (2011, 2012), Lloberas-Valls (2013), among others.

A second approach is known as Computational Homogenization Method (CHM). Similar to the CMM, it is based on multiscale modeling, in that information is obtained from multiple length scales. Assuming that the length scales are separated, this approach establishes a weak coupling between them. The micro-structural features are not physically inserted in the structural model, as in the case of CMM, but they are modeled into a so called representative volume element (RVE) which is associated to each integration point of the macroscopic mesh (see Figure 1.20). This RVE, considered as a representative sample of the micro-structure, is then used to obtain a homogenized response to the macroscopic strain field, thus emulating an equivalent homogeneous medium. Due to its flexibility (no assumption has to be made on the homogenized constitutive response) this model has been used to model a large class of materials characterized by complex micro-structures, with linear and nonlinear behaviors Miehe et al. (1999), Fritzen et al. (2013), Otero et al. (2012, 2015), Quinteros et al. (2012), Oller et al. (2005), Car et al. (2002), Zucchini and Lourenço (2002, 2009). This method is the one that will be used in the present research.

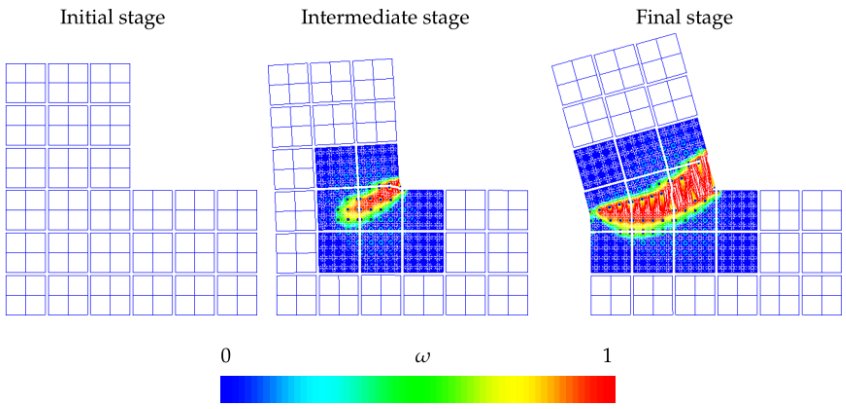

Figure 1.19: Example of Concurrent Multiscale Method, from Lloberas-Valls (2013)

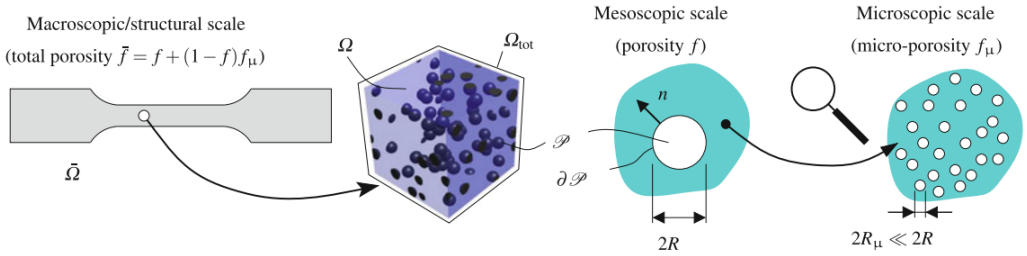

Figure 1.20: Example of a three-scale Computational Homogenization Method, from Fritzen et al. (2013)

Although classical first order CHM has been successfully used to model micro-structures exhibiting stable behaviors, it was soon recognized to give non-objective results when dealing with strain-softening materials. In fact the RVE looses its representativeness upon strain localization. In the last years, several modifications to the classical CHM were proposed, and a review on recent developments can be found in Nguyen et al. (2011) and in the references therein. Some approaches regularize the response of the RVE by using a higher order theory at the macro-scale, such that the information about a material characteristic length is naturally taken into account Geers et al. (2003), Kouznetsova et al. (2004, 2002), De Bellis (2009), De Bellis and Addessi (2011), Trovalusci and

Masiani (2003), Addessi et al. (2010) (see Figure 1.21). Others, known as continuous-discontinuous approaches, up-scale the RVE response to a traction-separation law (upon strain localization) used by a discontinuity inserted into the macro-scale model Massart (2003), Massart et al. (2007), Mercatoris et al. (2009), Mercatoris and Massart (2011), Oliver et al. (2014b,a), Belytschko et al. (2008), Bosco et al. (2015) (see Figure 1.22). Another issue related to the loss of representativeness of the RVE is the choice of proper boundary conditions to be applied on the RVE. A study on this topic has been done in Coenen et al. (2012), where a novel boundary condition has been proposed, using the concept of rotating periodicity to avoid constraining the crack propagation orientation. In the context of masonry modeling, works on continuous-discontinuous computational homogenization can be found in Massart et al. (2007), Massart (2003) for modeling the in-plane behavior of masonry structures, and later on extended to the study of shell elements for the analysis of the out-of-plane behavior Mercatoris et al. (2009), Mercatoris and Massart (2011), while works on computational homogenization using a Cosserat continuum at the macro-scale can be found in De Bellis (2009), De Bellis and Addessi (2011).

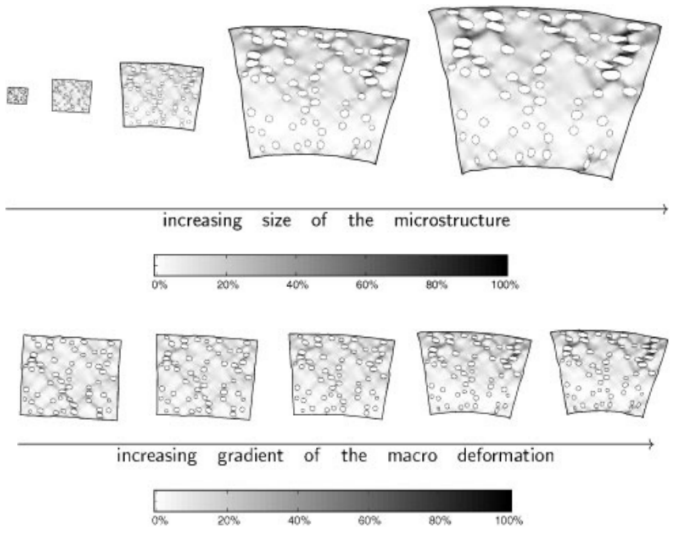

Figure 1.21: Example of higher order Computational Homogenization Method, from Kouznetsova et al. (2002)

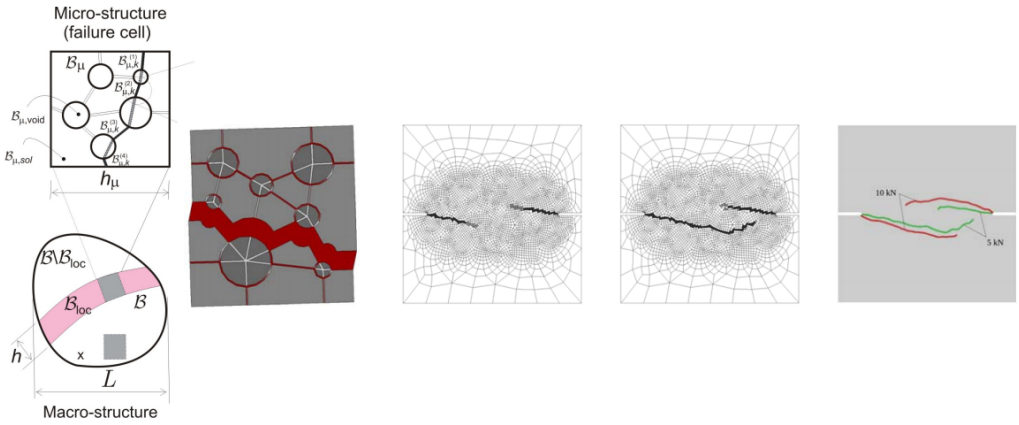

Figure 1.22: Example of continuous-discontinuous Computational Homogenization Method, from Oliver et al. (2014b,a)

1.5 Aims and objectives of the thesis

The aim of this research is the development of a computational multiscale homogenization technique for the analysis of masonry structure, subjected to quasi-static in-plane and out-of-plane loadings. Classical Cauchy continuum theory is used at both scales, thus using the so-called first order computational homogenization. Due to the brittle nature of masonry constituents, particular attention is given to the problem of strain localization. A review is done on the state-of-the-art of computational homogenization methods, focusing on the recently proposed extensions of classical homogenization for the study of problems involving strain localization. In this context, the present research proposes an extension of the fracture-energy-based regularization to the two-scale homogenization problem, allowing the usage of first order computational homogenization in problems involving strain localization. Moreover, due to the multiscale nature of the method, a review is also done on different micro-modeling strategies, in order to have a complete scenario of the available constitutive models and modeling techniques for the characterization of the micro-structure.

The proposed method is first stated for the standard continuum case, and it is applied to the two-dimensional analysis of in-plane loaded shear walls made of periodic brick masonry. Then, the aforementioned method is extended to the case of shells based on the

Reissner-Mindlin theory for the analysis of out-of-plane loaded masonry walls. The aim here is to obtain a method that can be used to analyze the majority of loading conditions a masonry structure can undergo. In both case (two-dimensional continuum and three-dimensional shell), the accuracy of the proposed method is validated comparing it with experimental evidences and with micro-model analyses.
To achieve the aforementioned aims, a set of main objectives has been drawn:

1. Review of micro-modeling techniques for masonry structures. Comparison of continuum and discrete micro-modeling approaches and identification of advantages and disadvantages. The objective is to obtain micro-modeling results to be used as a reference for the multiscale simulation, and to identify the available modeling techniques for the micro-structural samples (RVE) in multiscale simulations. This first stage of the research also includes the formulation of a tension/compression damage model able to take into account the dilatant behavior of mortar joints.

2. Review and formulation of classical first order computational homogenization. Review of available adaptations for problems involving strain-localization. Formulation of a novel regularized homogenization method. Extension of the fracture-energy-based regularization to the two-scale homogenization problem. Assessment of the methodology through simple benchmark problems. Study on the effects of different boundary conditions for the RVE.

3. Application of the proposed regularized homogenization method to the two-dimensional problem of in-plane loaded shear walls made of periodic brick-masonry.

4. Extension of the proposed method to the thick shell problem. Formulation and homogenization settings.

5. Application of the proposed method to the thick shell problem of out-of-plane loaded walls made of periodic brick-masonry.

1.6 Outline and organization of the thesis

The present thesis is organized as follows: Chapter 2 presents an investigation on three different micro-modeling techniques typically used to analyze masonry structures. The results obtained from these micro-models are used as a basis to characterize the RVE

micro-structure for the multiscale analyses. In the same context a continuum damage model, able to represent the dilatant effect of mortar joints, is formulated and described. Chapter 3 gives the main equations governing the classical First Order Computational Homogenization Method. It also presents the proposed regularization method to allow the usage of first order homogenization for the analysis of micro-structures undergoing strain localization. Chapter 4 shows the application of the proposed method for the analysis of in-plane loaded shear walls, under the 2D-plane stress assumptions. A comparison is made with the results obtained from the micro-models and from experimental tests. Chapter 5 presents the proposed extension of Computational Homogenization for the analysis of shell structures. Chapter 6 shows the application of the proposed homogenization for shells to the numerical simulation of out-of-plane loaded masonry walls. Chapter 7 gives some conclusions about the proposed numerical approach, and draws some possible new lines of research for future works. Finally, Appendix A, Appendix B and Appendix C focus on some detailed numerical aspects related to the concepts explained in the preceding chapters.

This page is intentionally left blank

Chapter 2

Continuum and discrete micro-modeling strategies for masonry structures

This chapter presents a numerical investigation on the behavior of three different micro-modeling strategies for the analysis of in-plane loaded masonry shear walls.
A novel damage mechanics-based meso-model for the analysis of masonry-walls is presented and compared with two well-known micro-models. The two micro-models discretize masonry micro-structure with nonlinear interfaces for mortar-joints, and continuum elements for units. The proposed meso-model discretizes both units and mortar-joints with continuum elements, making use of a tension/compression damage model, here refined to properly reproduce the nonlinear response under shear and to control the dilatancy. The three investigated models are validated against experimental results. They all prove to be similarly effective, with the proposed model being less time-consuming, due to the efficient format of the damage model.
Masonry is a heterogeneous material, with a micro-structure made of bricks and joints, with or without mortar. The heterogeneity of the micro-structure, in terms of mechanical properties and geometrical arrangement, lead to very complex behaviors and different failure mechanisms. Several computational strategies were proposed to deal with the numerical analysis of such a complex material Roca et al. (2010). Several macro-models, also known as continuum finite element models, are available in the ex-

isting literature to study masonry structures. The most recent macro-models regard the material as a fictitious homogeneous orthotropic continuum, without making any explicit distinction between units and joints in the discrete model Pelà et al. (2011, 2013, 2014b). This approach presents some intrinsic difficulties mainly related to the identification of the mechanical parameters of the continuum and the definition of realistic phenomenological failure criteria. However, macro-models are still a suitable option for the numerical analysis of large and complex structures due to their limited computational cost. More sophisticated numerical strategies were proposed by several authors for detailed analysis of single structural members, where a full description of the interaction between units and mortar is necessary (Figure 2.1a). Very popular approaches used nowadays to study masonry, including its heterogeneous micro-structure in the discretization, are micro/meso-modeling Lourenço and Rots (1997), Lourenço (1996), Oliveira and Lourenço (2004), Drougkas et al. (2014), Lotfi and Shing (1994), Sacco and Toti (2010), Raffa et al. (2013), Gambarotta and Lagomarsino (1997), Citto (2008). Midway between macro- and micro/meso-modeling there are the homogenization methods Petracca et al. (2016), Quinteros et al. (2012), Zucchini and Lourenço (2002, 2009), De Bellis (2009), De Bellis and Addessi (2011), Massart (2003), Massart et al. (2007), Mercatoris et al. (2009), Mercatoris and Massart (2011).

A complete and detailed description of masonry micro-structure would require the full three-dimensional discretization of bricks, mortar joints, and the interface between them. In this way all masonry constituents and their complex interaction would be explicitly accounted for. However, three-dimensional modeling requires a complex model generation and high computational costs. For the case of a wall made of one layer of bricks with a regular pattern, the 2D plane stress assumption can be made to simplify the problem.

The objective of the work described in this chapter is to propose a novel damage-mechanics based meso-model able to represent the mechanical behaviors of masonry constituents. The proposed meso-model is based on a tension-compression continuum damage model Cervera et al. (1995), Faria et al. (1998), Wu et al. (2006), here refined in order to accurately reproduce the nonlinear response of masonry constituents, especially in shear. The adoption of appropriate failure criteria enables the analyst to control the dilatant behavior of the material, even though this aspect is not generally associated to continuum damage models as it is for plasticity models. The study proposes a simple solution to this issue, consisting in the appropriate definition of the failure surfaces

under shear stress states together with the formulation of proper evolution laws for damage variables. For this aim, a failure criterion for quasi-brittle materials Lubliner et al. (1989) is suitably enhanced under shear conditions and a novel hardening-softening law based on quadratic Bézier curves is established. The model keeps the simple and efficient format of classical damage models, where the explicit evaluation of the internal variables avoids nested iterative procedures, thus increasing computational performance and robustness.

Another purpose of this research is to carry out a critical comparison of a meso- and two micro-modeling strategies for the numerical simulation of shear walls made of periodic masonry, where the interaction between units and mortar joints is explicitly taken into account by their distinct discretization.The distinction made here between meso- and micro-modeling is referred to the different types of finite elements and constitutive models used for the discretization of masonry micro-structure. Micro-modeling has been widely adopted by several authors in literature Lourenço and Rots (1997), Oliveira and Lourenço (2004), Raffa et al. (2013), Sacco and Toti (2010), Citto (2008), Gambarotta and Lagomarsino (1997), Lotfi and Shing (1994) and it uses a discrete description of masonry micro-structure, mixing continuum and interface elements for bricks and mortar joints, respectively. On the contrary, meso-modeling uses a continuum discretization of all components of the masonry micro-structure, without resorting to interface elements. The investigated approaches are validated against experimental tests of masonry shear walls under different level of vertical compression Raijmakers and Vermeltfoort (1992), proving to be similarly effective and accurate in predicting the global strength of shear walls up to their collapse. Both micro- and meso-modeling techniques are able to properly reproduce the main failure mechanisms of the material, such as tensile cracking, sliding, shear and crushing. However, each one of the selected models introduces approximations that lead to slight differences in accuracy, robustness and computational cost.

The validation of the novel meso-model, together with the critical review of available micro-models, leads to a fruitful discussion on advanced computational strategies for the analysis of masonry structures at the level of material constituents. Finally, the results obtained and described here, are used as a reference for comparison with the multiscale analyses presented in the next chapters of this thesis. Furthermore all the considerations made here for the different discretization techniques and the different constitutive models, are used to model the RVE micro-structure for the multiscale analyses.

2.1 Adopted modeling strategies

The three selected modeling strategies are :

1. **2D Continuum micro-model (2D-C)**: Both units and mortar joints are modeled using 2D plane-stress continuum elements with nonlinear behavior (see Figure 2.1b).

2. **2D Discrete micro-model (2D-D)**: All non-linearity is lumped into mortar joints using interface elements. Units are considered elastic with vertical interfaces for potential splitting cracks (see Figure 2.1c).

3. **2D mixed Continuum/Discrete micro-model (2D-CD):** Mortar joints are represented by nonlinear interface elements, whereas units are modeled with 2D plane-stress continuum elements with nonlinear behavior, to avoid forcing the crack pattern inside the units, differently from 2D-D approach (see Figure 2.1d).

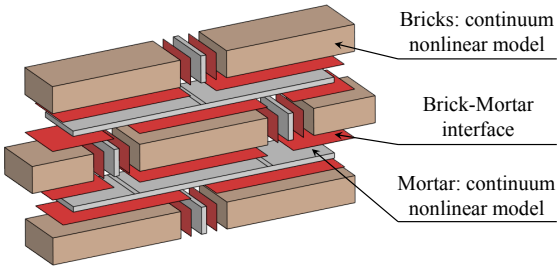

(a) Masonry micro-structure

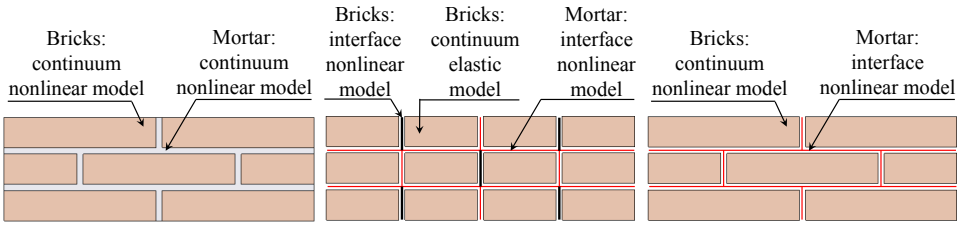

(b) 2D-C micro-model (c) 2D-D micro-model (d) 2D-CD micro-model

Figure 2.1: Masonry modeling strategies

The aforementioned 2D-D and 2D-CD modeling strategies for masonry structures are very well-known and they have been used by several authors in literature. In the present comparative study, the adopted constitutive model for interfaces is the one presented in Lourenço and Rots (1997). They are also known as "simplified micro-models", while "detailed micro-models" would consider a distinct discretization for units and mortar (by means of continuum finite elements) and unit-mortar interface (by means of interface elements).

On the other hand, the proposed 2D-C modeling strategy considers a more classical approach, discretizing both bricks and mortar joints with continuum elements. In this context, and to propose an efficient and robust numerical method, a constitutive law based on continuum damage mechanics is adopted, taking advantage of its explicit evaluation, thus avoiding local iterative procedures typically necessary to integrate plasticity-based models. In particular, the d^+/d^- tension-compression damage framework Cervera et al. (1995), Faria et al. (1998), Wu et al. (2006) has been used. This model introduces two failure criteria for tensile and compressive stress states, as well as two scalar damage indexes, allowing the description of different behaviors under tension and compression. A novel failure criterion for compression is presented in Section 2.2.2, and Section 2.3 describes how this criterion can be used to control the dilatant behavior of the damage model.

In the following, Section 2.2 describes the continuum damage model here proposed, and used for both bricks and mortar joints in the modeling strategy 2D-C, and for bricks in the modeling strategy 2D-CD, while Section 2.4 describes the constitutive model used for mortar interfaces in the modeling strategies 2D-D and 2D-CD.

2.2 Proposed tension/compression continuum damage model

2.2.1 Constitutive model

The bi-dissipative d^+/d^- damage model, based on the works in Cervera et al. (1995), Faria et al. (1998), Wu et al. (2006), defines the stress tensor as

$$\boldsymbol{\sigma} = \left(1 - d^+\right) \bar{\boldsymbol{\sigma}}^+ + \left(1 - d^-\right) \bar{\boldsymbol{\sigma}}^- \tag{2.1}$$

where $\bar{\boldsymbol{\sigma}}^+$and $\bar{\boldsymbol{\sigma}}^-$are the positive and negative parts of the effective stress tensor $\bar{\boldsymbol{\sigma}}$:

$$\bar{\boldsymbol{\sigma}} = \boldsymbol{C} : \boldsymbol{\varepsilon} \tag{2.2}$$

$$\bar{\boldsymbol{\sigma}}^{+} = \sum_{i=1}^{3} \langle \bar{\sigma}_i \rangle \, \boldsymbol{p}_i \otimes \boldsymbol{p}_i \tag{2.3}$$

$$\bar{\boldsymbol{\sigma}}^{-} = \bar{\boldsymbol{\sigma}} - \bar{\boldsymbol{\sigma}}^{+} \tag{2.4}$$

d^+ and d^- are respectively the tensile and compressive damage indexes, and they affect respectively the positive $\bar{\boldsymbol{\sigma}}^{+}$ and negative $\bar{\boldsymbol{\sigma}}^{-}$ part of the effective stress tensor $\bar{\boldsymbol{\sigma}}$. The damage indexes are scalar variables ranging from 0 (intact material) to 1 (completely damaged material).

2.2.2 Failure criteria

Two scalar measures are introduced, termed as equivalent stresses τ^+ and τ^-, in order to identify "loading", "unloading" or "reloading" situations for a general state of stress. The compressive surface employed in this research represents an improvement of the one described in Lubliner et al. (1989). The equivalent stress τ^- is computed as

$$\tau^{-} = \frac{1}{1-\alpha}\left(\alpha \bar{I}_1 + \sqrt{3\bar{J}_2} + k_1 \beta \, \langle \bar{\sigma}_{max} \rangle\right) \tag{2.5}$$

$$\alpha = \frac{k_b - 1}{2k_b - 1} \tag{2.6}$$

$$\beta = \frac{f_{cp}}{f_t}(1-\alpha) - (1+\alpha) \tag{2.7}$$

where $\bar{I}_1$ is the first invariant of the effective stress tensor, $\bar{J}_2$ is the second invariant of the effective deviatoric stress tensor, $\bar{\sigma}_{max}$ is the maximum effective principal stress, f_{cp} is the compressive peak stress and k_b is the ratio between bi-axial and uniaxial compressive strengths. The constant k_1 in Eq. (2.5) is proposed in this research to control the effect of the compressive surface on the dilatant behavior of the model, as described in Section 2.3. This constant can range from 0 (leading to the Drucker-Prager criterion) to 1 (leading to the criterion proposed in Lubliner et al. (1989)), as shown in Figure 2.2.

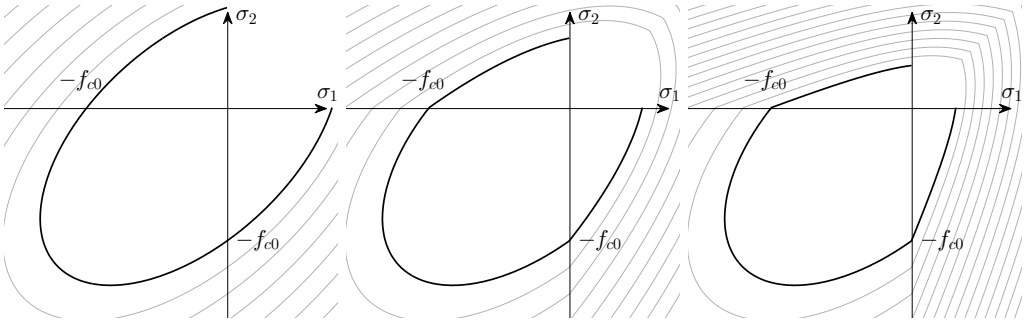

(a) $k_1 = 0$ (b) $k_1 = 0.16$ (c) $k_1 = 0.5$

Figure 2.2: Proposed compressive failure surface for the continuum model. Influence of the parameter k_1

The tensile surface is similar to the compressive one

$$\tau^+ = \frac{1}{1-\alpha}\left(\alpha\bar{I}_1 + \sqrt{3\bar{J}_2} + \beta\left\langle\bar{\sigma}_{max}\right\rangle\right)\frac{f_t}{f_{cp}} \tag{2.8}$$

but without the k_1 parameter. Here the term $\frac{f_t}{f_{cp}}$ has been introduced to relate τ^+ to the tensile strength f_t. A plot with the superposition of the two damage surfaces, in principal stress space for the 2D plane-stress case, is given in Figure 2.3. Since these surfaces are defined for any stress state, it is necessary to make them inactive under certain conditions:

1. compressive surface is allowed to evolve only if at least one principal stress is negative

2. tensile surface is allowed to evolve only if at least one principal stress is positive

These conditions can be taken into account by rewriting the damage surfaces as:

$$\tau^- = H\left(-\bar{\sigma}_{min}\right)\left[\frac{1}{1-\alpha}\left(\alpha\bar{I}_1 + \sqrt{3\bar{J}_2} + k_1\beta\left\langle\bar{\sigma}_{max}\right\rangle\right)\right] \tag{2.9}$$

$$\tau^+ = H\left(\bar{\sigma}_{max}\right)\left[\frac{1}{1-\alpha}\left(\alpha\bar{I}_1 + \sqrt{3\bar{J}_2} + \beta\left\langle\bar{\sigma}_{max}\right\rangle\right)\frac{f_t}{f_{cp}}\right] \tag{2.10}$$

where $H\left(x\right)$ is the Heaviside function, defined as

$$H(x) = \begin{cases} 0 & x < 0 \\ 1 & x > 0 \end{cases} \tag{2.11}$$

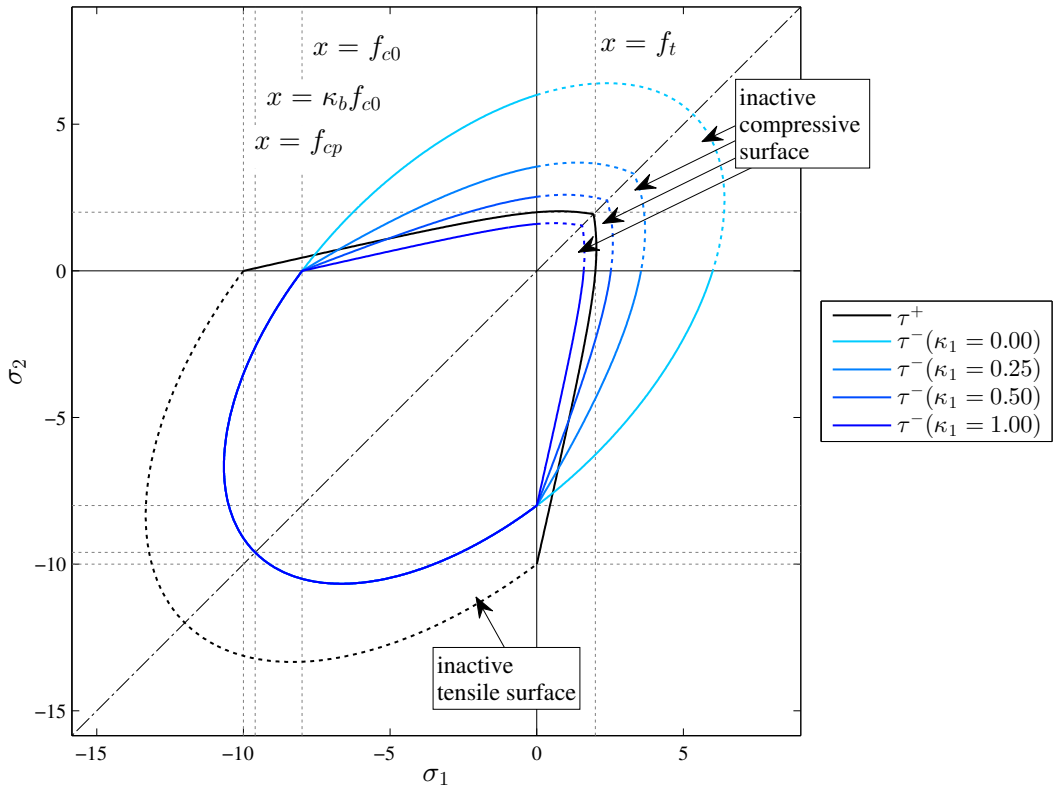

Figure 2.3: initial damage surfaces (2D plane-stress)

For the 3D case, the compressive damage surface can be further reworked Lubliner et al. (1989) to improve the compressive behavior of the model:

$$\tau^- = H(-\bar{\sigma}_{min}) \left[\frac{1}{1-\alpha} \left(\alpha \bar{I}_1 + \sqrt{3\bar{J}_2} + k_1 \beta \langle \bar{\sigma}_{max} \rangle + \gamma \langle -\bar{\sigma}_{max} \rangle \right) \right] \tag{2.12}$$

In Eq. (2.12) the additional term $\gamma \langle -\bar{\sigma}_{max} \rangle$, with the coefficient $\gamma > 0$, accounts for the increased strength under stress states of triaxial compression. It is obvious that this

term is nonzero only for the 3D case when the maximum principal stress is negative. Figure 2.4 and Figure 1.8 show the obtained failure surfaces in the full 3D principal stress space, superimposed to their intersection with the plane-stress plane. The portions of those surfaces drawn in transparency are those portions cut out by the Heaviside function previously described.

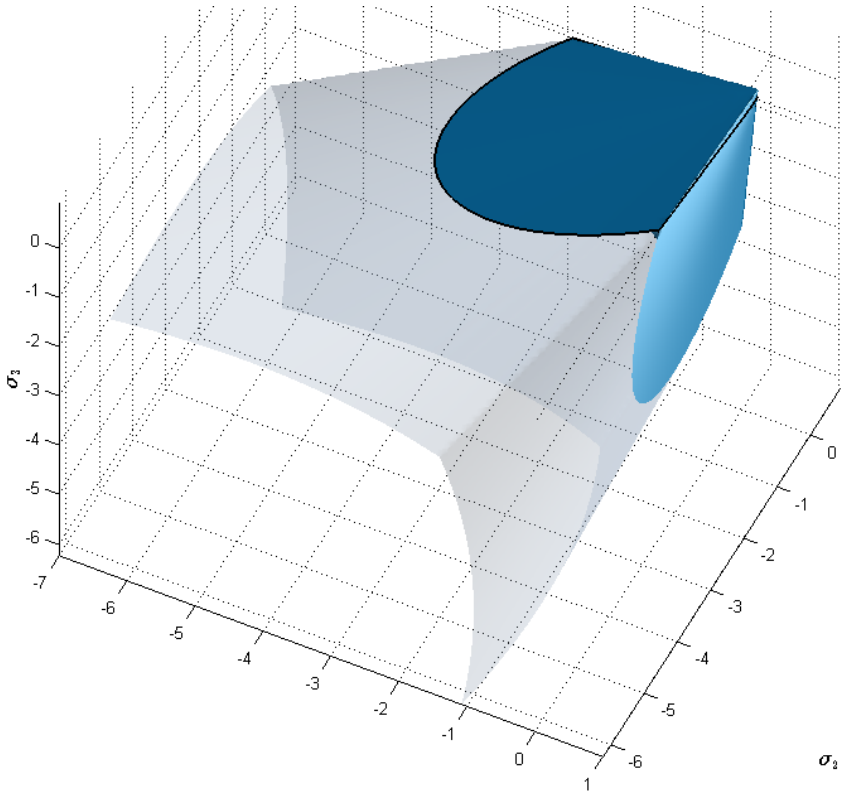

Figure 2.4: initial tensile damage surface (3D). Inactive surface in transparency

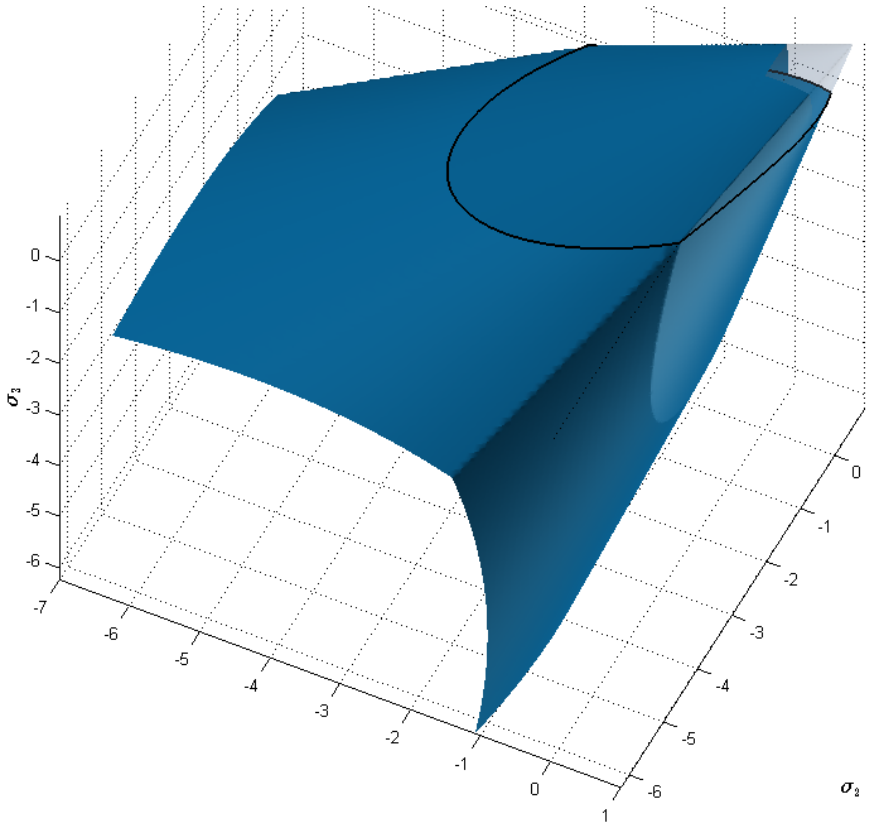

Figure 2.5: initial compressive damage surface (3D). Inactive surface in transparency

Being the damage an irreversible process, other two scalar quantities are introduced, termed as damage thresholds $r^{\pm}$, that represent the largest values ever reached by the equivalent stresses $\tau^{\pm}$ during the loading history. The damage thresholds $r^{\pm}$ at time $t + \Delta t$ can be explicitly evaluated as

$$r^{\pm} = max\left(r_0^{\pm}, \max_{0 \leq n \leq t} \tau_n^{\pm}\right)$$

$$r_0^{+} = f_t \tag{2.13}$$

$$r_0^{-} = f_{c0} \tag{2.14}$$

where r_0^+ and r_0^- represent the initial damage thresholds respectively in tension and compression (i.e. the elastic limits in uniaxial tension f_t and compression f_{c0}), and n denotes the time instant. Accordingly, the following damage criteria are introduced:

$$\Phi\left(\tau^{\pm}, r^{\pm}\right) = \tau^{\pm} - r^{\pm} \leq 0 \tag{2.15}$$

2.2.3 Evolution laws for damage variables

The tensile damage index d^+ is calculated according to the following equation:

$$d^+\left(r^+\right) = 1 - \frac{r_0^+}{r^+} exp\left\{2H_{dis}\left(\frac{r_0^+ - r^+}{r_0^+}\right)\right\} \tag{2.16}$$

where H_{dis} is the discrete softening parameter. In the discrete problem the softening law should be adjusted according to the size of the dissipative zone (l_{dis}) Bažant and Oh (1983), Oliver (1989), Oller (2001), in such a way that the following equation holds:

$$g_f\, l_{dis} = G_f \tag{2.17}$$

where the specific dissipated energy g_f, for the exponential softening law, can be calculated as:

$$g_f = \left(1 + \frac{1}{H_{dis}}\right)\frac{f_t^2}{2E} \tag{2.18}$$

The discrete softening parameter is calculated as

$$H_{dis} = \frac{l_{dis}}{l_{mat} - l_{dis}} \tag{2.19}$$

where $l_{mat} = 2EG_f/f_t^2$. l_{dis} is assumed equal to the characteristic length of the FE ($l_{dis} = l_{ch}$). The resulting tensile uniaxial law is given in Figure 2.6.

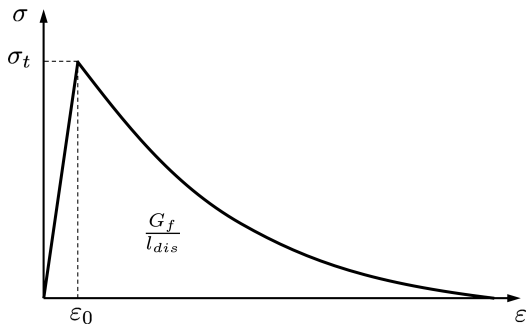

Figure 2.6: tensile uniaxial law

For the evaluation of the compressive damage index d^-an ad hoc formulation is proposed in this paper, in order to obtain a compressive uniaxial law like the one given in Figure 2.7.

This curve consists of a linear part $[(0,0)-(\varepsilon_0,\sigma_0)]$, a hardening part $[(\varepsilon_0,\sigma_0)-(\varepsilon_p,\sigma_p)]$ and two softening parts $[(\varepsilon_p,\sigma_p)-(\varepsilon_k,\sigma_k)]$ $[(\varepsilon_k,\sigma_k)-(\varepsilon_u,\sigma_u)]$, followed by a final residual part $[(\varepsilon_u,\sigma_u)-(+\infty,\sigma_u)]$. The hardening and softening parts are three quadratic bezier curves. Each one has three control points defining the shape of the curve, the end-positions, and the tangents to the curve at the end-positions.

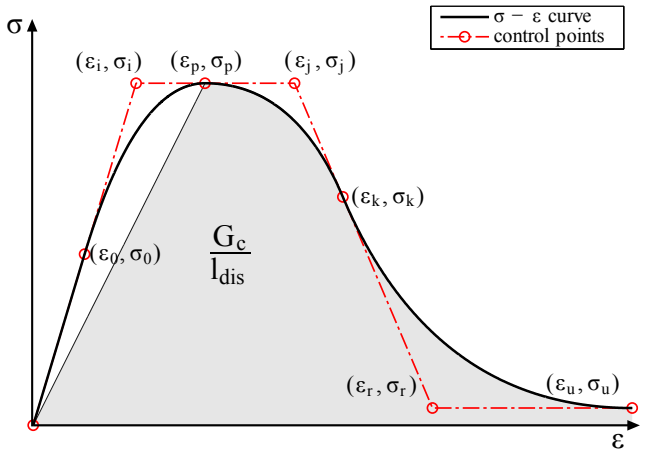

Figure 2.7: compressive uniaxial law

We can define a function $\mathscr{B}$ that evaluates the Y-coordinate of a bezier curve at a given X-abscissa, given the three control points, as follows:

$$\mathscr{B}\left(X,\ x_1, x_2, x_3,\ y_1, y_2, y_3\right) = \left(y_1 - 2y_2 + y_3\right) t^2 + 2\left(y_2 - y_1\right) t + y_1 \tag{2.20}$$

where

$$\begin{aligned} A &= x_1 - 2x_2 + x_3 \\ B &= 2\left(x_2 - x_1\right) \\ C &= x_1 - X \\ D &= B^2 - 4AC \\ t &= \frac{-B + \sqrt{D}}{2A} \end{aligned}$$

Given the current compressive damage threshold r^-, its strain-like counterpart ξ can be obtained

$$\xi = \frac{r^-}{E} \tag{2.21}$$

and then it is used to calculate the corresponding hardening variable $\Sigma\left(\xi\right)$:

$$\Sigma\left(\xi\right) = \begin{cases} \mathscr{B}\left(\xi,\ \varepsilon_0, \varepsilon_i, \varepsilon_p,\ \sigma_0, \sigma_i, \sigma_p\right) & \varepsilon_0 < \xi \leq \varepsilon_p \\ \mathscr{B}\left(\xi,\ \varepsilon_p, \varepsilon_j, \varepsilon_k,\ \sigma_p, \sigma_j, \sigma_k\right) & \varepsilon_p < \xi \leq \varepsilon_k \\ \mathscr{B}\left(\xi,\ \varepsilon_k, \varepsilon_r, \varepsilon_u,\ \sigma_k, \sigma_r, \sigma_u\right) & \varepsilon_k < \xi \leq \varepsilon_u \\ \sigma_u & \xi > \varepsilon_u \end{cases} \tag{2.22}$$

Finally the damage index d^- can be calculated as follows:

$$d^-\left(r^-\right) = 1 - \frac{\Sigma\left(\xi\right)}{r^-} \tag{2.23}$$

This novel formulation for the evolution law of the compressive damage parameter d^- is more flexible than conventional ones. In fact, the control points of the bezier curves may be set so that the curve can match the experimental response obtained from an uniaxial compressive test. Then the compressive fracture energy G_c (shaded area in Figure 2.7) is evaluated with the following relations:

$$G_{c,1} = \frac{\sigma_p \varepsilon_p}{2} \tag{2.24}$$

$$G_{c,2} = \mathscr{G}\left(\varepsilon_p, \varepsilon_j, \varepsilon_k,\ \sigma_p, \sigma_j, \sigma_k\right) \tag{2.25}$$

$$G_{c,3} = \mathscr{G}\left(\varepsilon_k, \varepsilon_r, \varepsilon_u,\ \sigma_k, \sigma_r, \sigma_u\right) \tag{2.26}$$

$$G_c = G_{c,1} + G_{c,2} + G_{c,3} \tag{2.27}$$

where the area $\mathscr{G}$ under each bezier curve reads:

$$\mathscr{G}\left(x_1, x_2, x_3,\ y_1, y_2, y_3\right) = \frac{x_2 y_1}{3} + \frac{x_3 y_1}{6} - \frac{x_2 y_3}{3} + \frac{x_3 y_2}{3} + \frac{x_3 y_3}{2} - x_1 \left(\frac{y_1}{2} + \frac{y_2}{3} + \frac{y_3}{6}\right) \tag{2.28}$$

It should be noted that here G_c is not referred to the total area under the uniaxial curve, but only to the part that needs to be regularized (post-peak regime).
In the discrete problem the compressive curve shown in Figure 2.7 needs to be regularized in such a way that the shaded area underneath be G_c/l_{dis}. This can be achieved by *"stretching"* the strain abscissas ε_j, ε_k, ε_r and ε_u (before using them in Eq. (2.22)):

$$\tilde{\varepsilon}_\alpha = \varepsilon_\alpha + \mathcal{S}\left(\varepsilon_\alpha - \varepsilon_p\right), \qquad \alpha = j, k, r, u \tag{2.29}$$

where $\mathcal{S}$ is a stretching factor calculated as

$$\mathcal{S} = \frac{\dfrac{G_c}{l_{dis}} - G_{c,1}}{G_c - G_{c,1}} - 1 \tag{2.30}$$

This factor should be greater than -1.0 to avoid a constitutive snap-back. In fact for a stretch factor $\mathcal{S} = -1.0$ every post-peak strain-abscissa would collapse to the peak strain ε_p, leading to a sudden fall of the uniaxial curve. To avoid this, the characteristic length l_{dis} should satisfy the following restriction:

$$l_{dis} < \frac{2G_c}{\sigma_p \varepsilon_p} \tag{2.31}$$

The effect of this regularization on the uniaxial law can be seen in Figure 2.8. Further details are described in Appendix B.

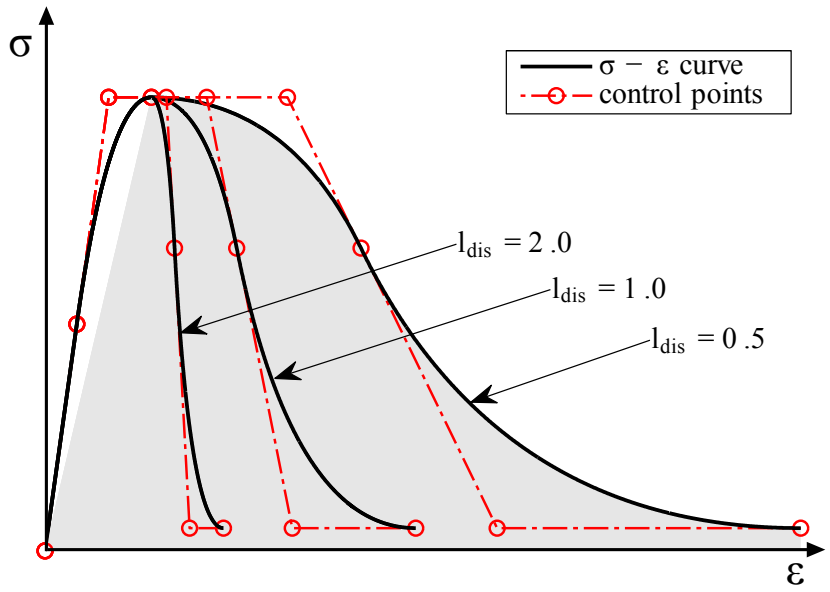

Figure 2.8: regularization of compressive uniaxial law

2.3 Shear behavior and dilatancy of the tension/compression continuum damage model

This section describes the shear behavior of the proposed d^+/d^- damage model. The present formulation includes the possibility to calibrate the dilatant behavior of the material under shear stresses. This crucial aspect has been usually disregarded by available models based on classical damage mechanics theory. Such disadvantage often favored the use of plasticity models since they can control explicitly the dilatancy through the definition of a proper plastic potential. This work proposes an improvement of the well-known d^+/d^- damage model Cervera et al. (1995), Faria et al. (1998), Wu et al. (2006) to control the dilatant behavior of the material. The material dilatancy is described without resorting to the formulation of a plastic potential, i.e. differently from well-established plasticity models (e.g. Eq. (2.37)). The objective of the proposed approach

is to describe phenomenologically the dilatant behavior without spoiling the simple and efficient format of the classical damage mechanics models.

2.3.1 Shear response of the tension/compression damage model

In the framework of the d^+/d^- damage model (and for the sake of conciseness let us consider the 2D plane stress case), when the two principal stresses have different sign, both tensile and compressive surfaces might be active. In this case the positive principal stress is affected by the tensile damage while the minimum principal stress is affected by the compressive damage. If the damage was isotropic, i.e. the tension and compression damage variables are equal, the damaged stress tensor would be an isotropic scaling of the effective (elastic) stress tensor. On the other hand, in the d^+/d^- damage model the damaged stress tensor is actually obtained by an anisotropic scaling of the effective (elastic) stress tensor, as it was already demonstrated in Pelà et al. (2011).
Figure 2.9 graphically shows this behavior for the simple case of a pure shear distortion, in an isotropic damage model (Figure 2.9a) and d^+/d^- damage model (Figure 2.9b). Let us suppose that the material point is subject to a given strain state whose components are ($\varepsilon_{xx} = 0$, $\varepsilon_{yy} = 0$, $\gamma_{xy} \neq 0$). Point A represents the effective stress state $\bar{\boldsymbol{\sigma}} = \boldsymbol{C} : \boldsymbol{\varepsilon}$ due to pure shear, with coordinates $(\bar{\sigma}_1, \bar{\sigma}_2 = -\bar{\sigma}_1)$ in the principal stresses reference system. Point B represents the damaged stress state $\boldsymbol{\sigma}$ denoted by coordinates $(\sigma_1, \sigma_2 = -\sigma_1)$ obtained in the case of an isotropic damage model, i.e. if $d^+ = d^-$. In this case the damaged stress tensor is an isotropic scaling of the effective stress tensor, since the isotropic scalar damage index scales the whole effective stress tensor $\bar{\boldsymbol{\sigma}}$. Consequently the damaged stress would stay in a pure shear state as the effective stress (Figure 2.9a). Point C, instead, corresponds to the damaged stress $\boldsymbol{\sigma}$ obtained by the d^+/d^-damage model. In this case, due to the existence of two different failure surfaces, the tensile and compressive damage indexes do not have in general the same value, being their evolution laws different. Consequently the damaged stress in not an isotropic scaling of the effective stress. In the specific example depicted in Figure 2.9b, the compressive damage increment is smaller then the tensile one. Thus, due the preassigned null values for ε_{xx} and ε_{yy}, the damaged stress $\boldsymbol{\sigma}$ must denote a shear-compression state.

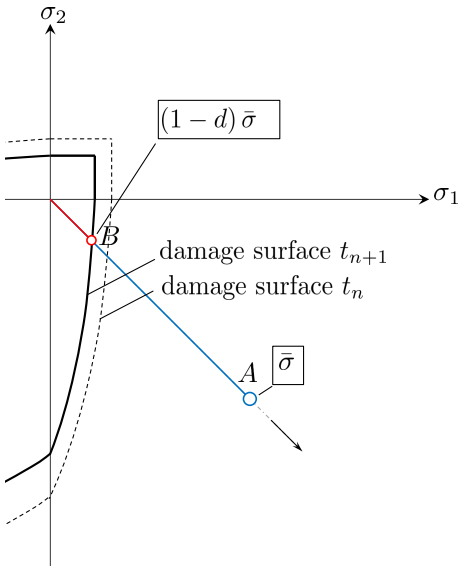

(a) isotropic damage

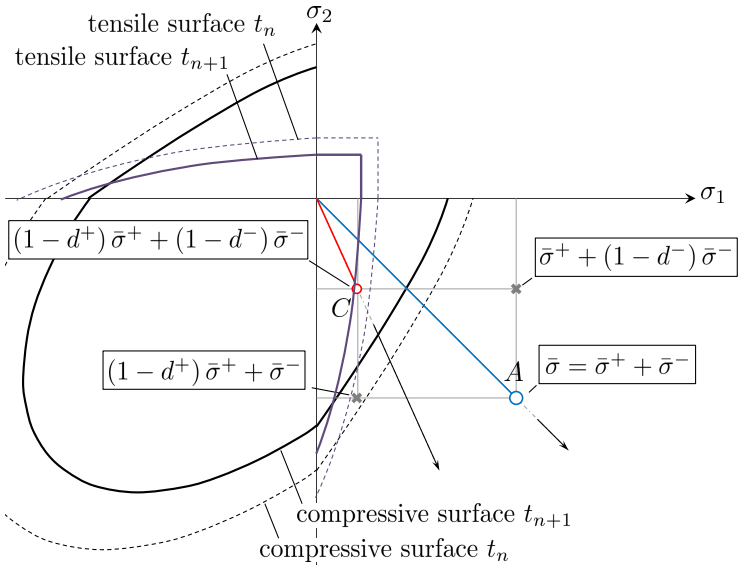

(b) d^+/d^- damage

Figure 2.9: behavior of isotropic and d^+/d^- damage models in tension/compression quadrants

In the definition of the compressive damage surface in Eq. (2.5), the parameter k_1 has been introduced to control the "weight" of the compressive surface on the constitutive shear response in the nonlinear range. As shown in Figure 2.2, the parameter k_1 controls the size of the compressive surface in tension/compression quadrants. As a consequence, this parameter controls implicitly also the dilatancy of the model, taking into account that the larger the compressive surface (with respect to the tensile surface), the higher the dilatancy. This effect is shown in Figure 2.10 for decreasing values of k_1, moving from Figure 2.10a to Figure 2.10c. It can be seen how decreasing k_1 from 1 to 0, the size of the compressive surface in the tension/compression quadrants increases. A a consequence, the increment of the compressive damage index d^- diminishes, thus predicting increasing compressive stresses.

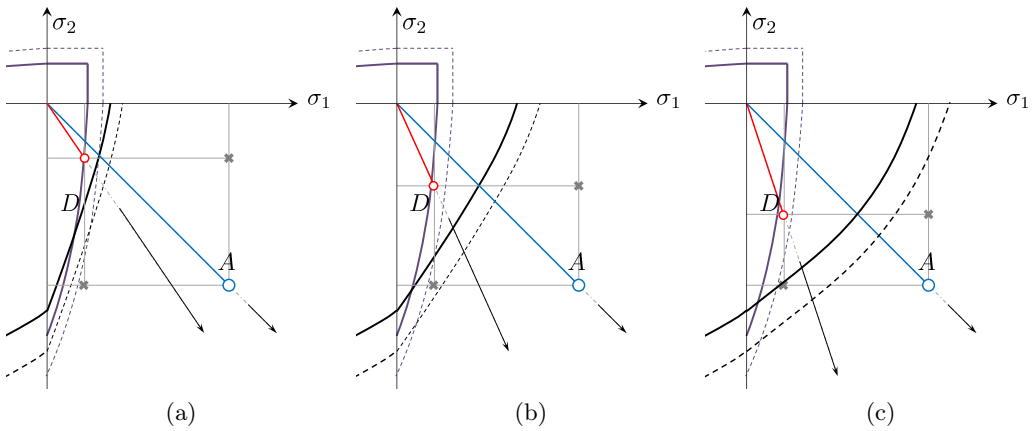

Figure 2.10: behavior of d^+/d^- damage model in tension/compression quadrants for values of k_1 decreasing from (a) to (c)

2.3.2 Numerical modeling of shear behavior of mortar joints

To assess the performance of the proposed constitutive model in shear, the experimental shear tests conducted in Pluijm (1993) are numerically reproduced here. These tests (the test set-up is shown in Figure 2.11a) aim at producing a constant stress state in the mortar joint. Mortar joints are subjected to shear under a constant confining stress.

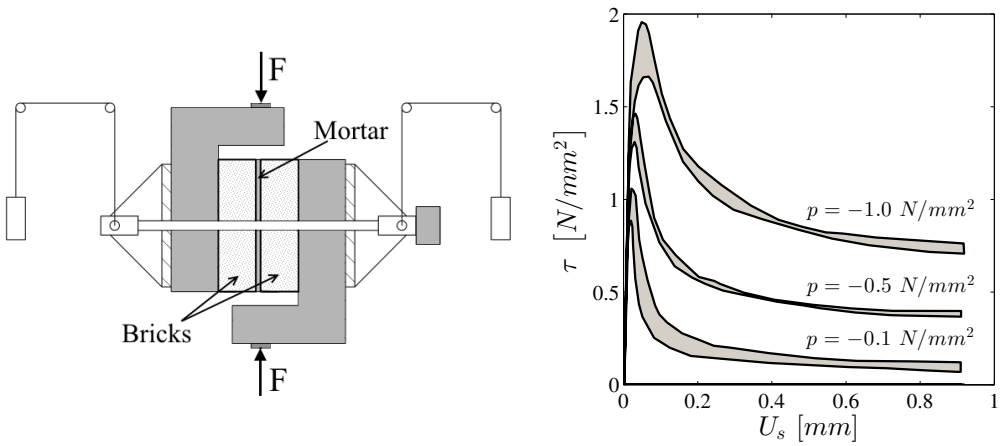

(a) (b)

Figure 2.11: Van Der Pluijm (1993). (a) test set-up; (b) test results for different values of confinement

The experimental tests were conducted with three different confining stress levels of -0.1, -0.5 and $-1.0\,N/mm^2$. Experimental results are given in Figure 2.11b in terms of envelope curves of shear stress τ vs. shear displacement U_s along the mortar joint. It can be seen how the maximum shear stress increases with increasing confining stress. After reaching a peak value, the shear stress decreases with increasing shear displacement, reaching a residual value due to dry friction. Another important aspect of this kind of experiment is the dilatancy of the mortar joint (Figure 2.12a), which describes the appearance (in the nonlinear range) of normal displacement perpendicular to the shear displacement. The ratio between the normal and shear displacements is denoted as the tangent to the dilatancy angle ψ. This behavior is related to the roughness of the crack surface. Experimental results show how dilatancy decreases with increasing normal stresses, as shown in Figure 2.12b. In the same way, for a constant normal stress, the dilatancy decreases to zero upon increasing shear displacement, as shown in Figure 2.12c.

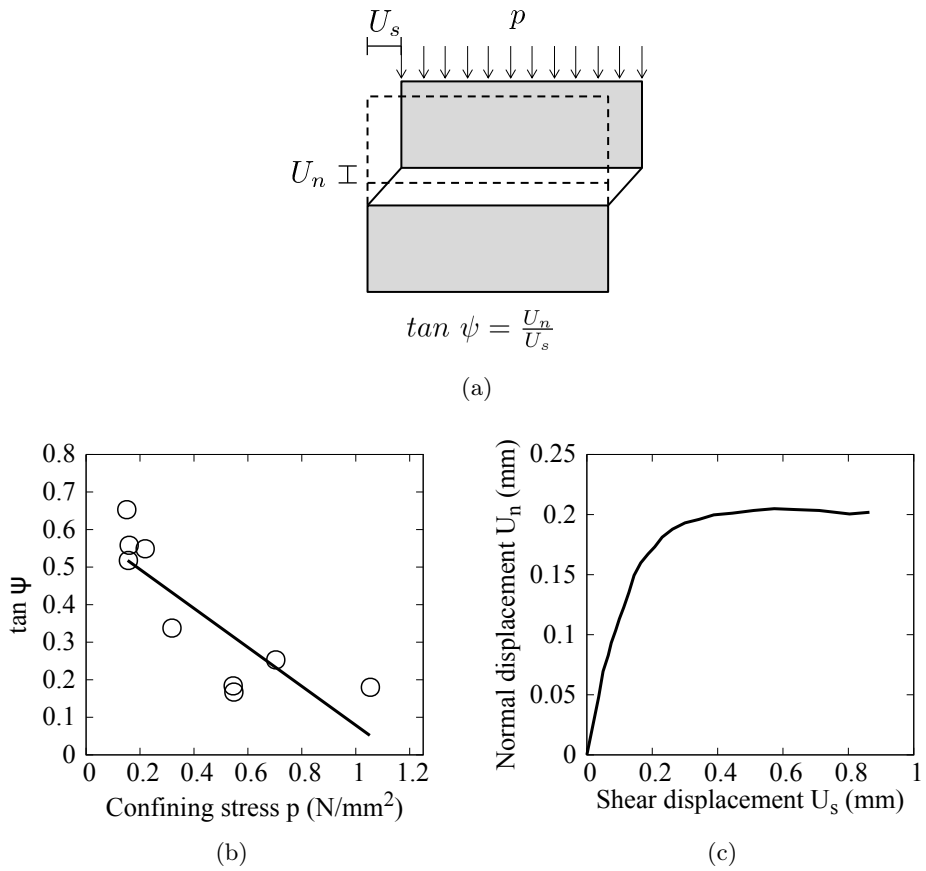

Figure 2.12: Van Der Pluijm (1993). (a) dilatancy of mortar joints; (b) dilatancy $tan\,\psi$ as a function of confining stress; (c) typical evolution of normal displacement for increasing values of shear displacement. Adapted from Lourenço (1996).

To study the control of the dilatancy in the proposed model, an elemental test was performed. The geometry and boundary conditions are shown in Figure 2.13. Material parameters are given in Table 2.1. For each level of confining stress ($p = -0.1$, $p = -0.5$, and $p = -1.0\,N/mm^2$) two analyses were conducted, using $k_1 = 0$, and $k_1 = 0.16$. The value $k_1 = 0.16$ was found as optimal for these tests as well as for the shear walls analyzed in Section 2.5.

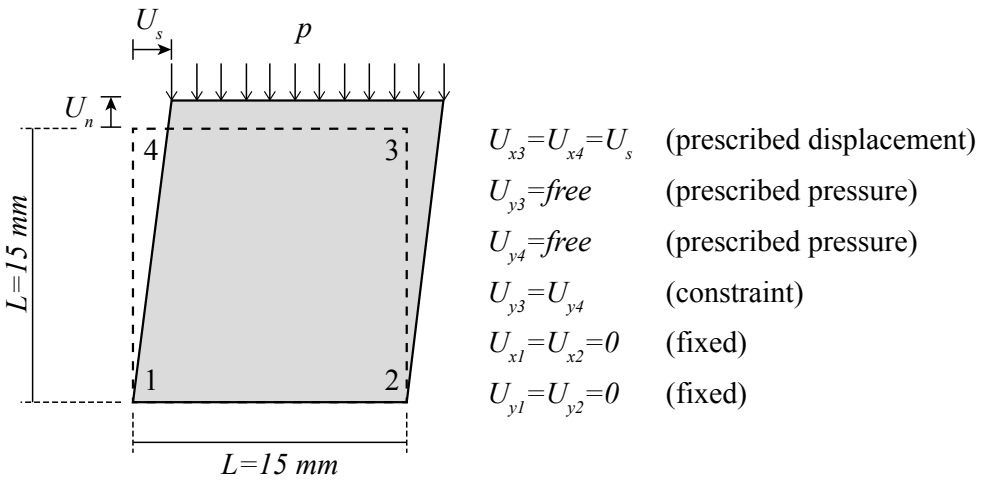

Figure 2.13: Elemental shear test. Geometry and boundary conditions

E	ν	σ_t	G_t	σ_0	σ_p	σ_r	G_c	ε_p	k_b
2970.0	0.15	0.62	0.02	8.0	11.0	1.0	20.0	0.005	1.16
$\frac{N}{mm^2}$	-	$\frac{N}{mm^2}$	$\frac{N}{mm}$	$\frac{N}{mm^2}$	$\frac{N}{mm^2}$	$\frac{N}{mm^2}$	$\frac{N}{mm}$	-	-

Table 2.1: mortar material properties for the shear tests

Results of the analyses are given in Table 2.2 in terms of shear strength and dilatancy, for each level of pre-compression. The first column show the shear stress - shear displacement curves, with the shear strength increasing for higher values of pre-compression. The second column show the uplift (positive vertical displacement) generated upon shear displacement. Finally the third column shows the dilatancy coefficient (which is the tangent to the curves reported in the second column). It can be clearly seen that if the standard Drucker-Prager failure surface ($k_1 = 0$) is chosen for compression, an overestimation of the dilatant behavior (with respect to the values shown in Figure 2.12b and Figure 2.12c) is obtained.

$\tau - U_s$	$U_n - U_s$	$tan\,\psi - U_s$
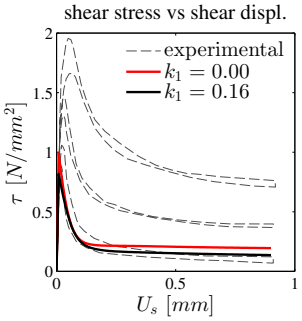	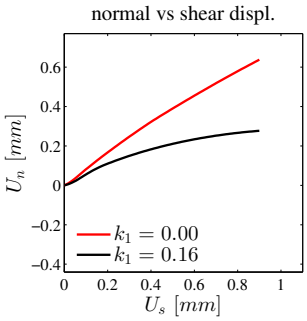	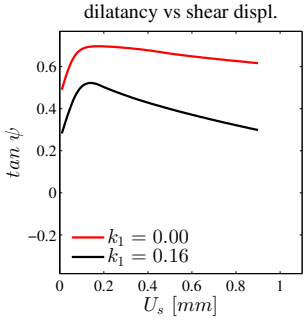
$p = -0.1\,N/mm^2$		
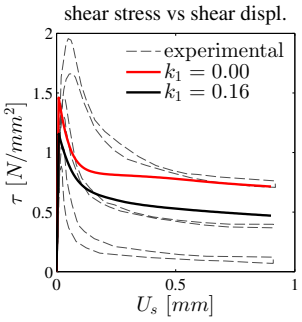	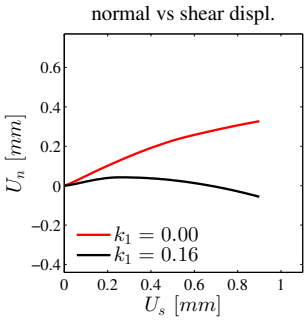	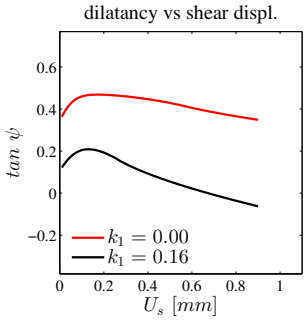
$p = -0.5\,N/mm^2$		
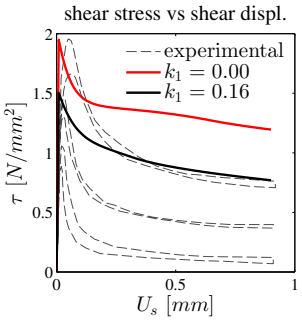	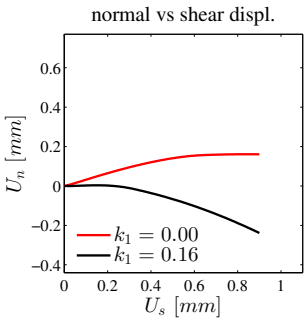	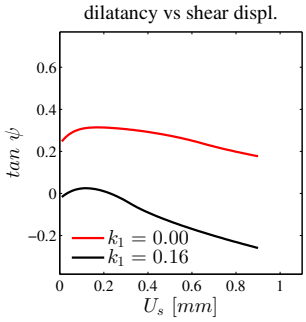
$p = -1.0\,N/mm^2$		

Table 2.2: Numerical results of the elemental shear test

Overall, these analyses show how the size of the compressive surface in the tension/compression quadrants has a major impact on the dilatancy of the model. As explained in the introduction of this section, the d^+/d^- damage model as proposed in Cervera et al. (1995), Faria et al. (1998), Wu et al. (2006) does not explicitly impose the direction of the inelastic strain, as opposed to plastic models. However, this elemental test has shown how a careful definition of the compressive damage surface, and especially of its shape in the II and IV quadrants of the principal (plane)stress space, can help in controlling the dilatant behavior in the proposed continuum damage model.

2.4 Multisurface plasticity interface model

Mortar joints are modeled using interface elements, allowing to incorporate discontinuities in the displacement field. Thus a constitutive law in terms of relative displacement and traction vector is required. The constitutive model adopted in this work is the one formulated in Lourenço and Rots (1997). Here a brief description of the model is given, and for further details the reader should refer to Lourenço and Rots (1997). This model is based on the concept of multisurface plasticity to better describe all failure mechanisms of masonry, through the definition of three surfaces for tension, shear and compressive failures, as shown in Figure 2.14.

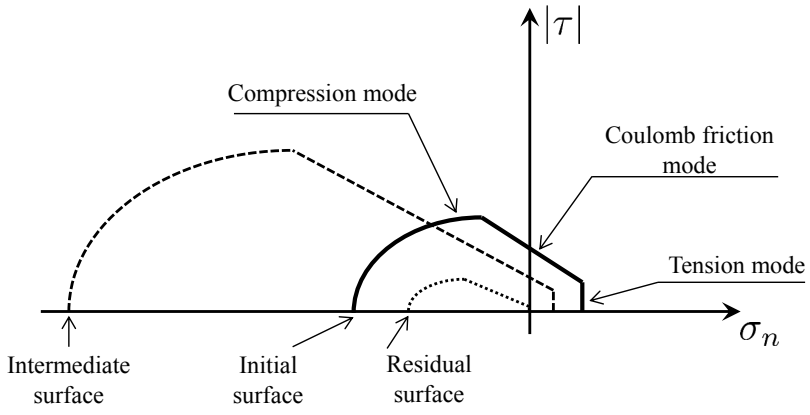

Figure 2.14: composite yield surface for mortar joints

For an interface element, the elastic response relating the generalized stresses $\boldsymbol{\sigma} = \{\sigma_n, \tau\}^T$ and the generalized strains $\boldsymbol{\varepsilon} = \{u_n, u_s\}^T$is given by

$$\boldsymbol{\sigma} = \boldsymbol{D}\boldsymbol{\varepsilon} = diag\left\{k_n, k_s\right\}\boldsymbol{\varepsilon} \tag{2.32}$$

where k_n and k_s are the stiffness parameters (not meant as dummy stiffnesses to simulate contact) in the normal and tangential directions, and can be obtained by the elastic properties of brick and mortar as follows:

$$k_n = \frac{E_b E_m}{t_m\left(E_b - E_m\right)};\; k_s = \frac{G_b G_m}{t_m\left(G_b - G_m\right)} \tag{2.33}$$

where E_b, E_m, t_m, G_b, G_m are respectively the brick Young's modulus, the mortar Young's modulus, the mortar thickness, the brick Shear modulus and the mortar Shear modulus. To describe the nonlinear regime, three yield functions are employed in the framework of multisurface plasticity:

$$f_1\left(\boldsymbol{\sigma}, \kappa_1\right) = \sigma_n - f_t\left(\kappa_1\right) \tag{2.34}$$

$$f_2\left(\boldsymbol{\sigma}, \kappa_2\right) = |\tau| + \sigma_n tan\phi\left(\kappa_2\right) - c\left(\kappa_2\right) \tag{2.35}$$

$$f_3\left(\boldsymbol{\sigma}, \kappa_3\right) = C_{nn}\sigma_n^2 + C_{ss}\tau^2 + C_n\sigma_n - fc\left(\kappa_3\right)^2 \tag{2.36}$$

f_1 is the tension cut-off criterion, where $f_t\left(\kappa_1\right)$ is the yield value and k_1 is the hardening/softening parameter. An associated flow rule is assumed.
f_2 is the Coulomb friction criterion, where $c\left(\kappa_2\right)$ is the cohesion, $\phi\left(\kappa_2\right)$ is the friction angle, and k_2 is the hardening/softening parameter. To properly describe dilatancy in mortar joints, a non associated flow rule is assumed, replacing the friction angle with the dilatancy angle ψ:

$$g_2\left(\boldsymbol{\sigma}, \kappa_2\right) = |\tau| + \sigma_n tan\psi\left(\kappa_2\right) - c\left(\kappa_2\right) \tag{2.37}$$

f_3 is the elliptical cap criterion, where $f_c\left(\kappa_3\right)$ is the yield value and k_3 is the hardening/softening parameter. C_{nn}, C_{ss} and C_n are parameters describing the shape of the elliptical cap. An associated flow rule is assumed.
The evolution of the yield value f_t is described by an exponential softening:

$$f_t(\kappa_1) = f_{t0} exp\left(-\frac{f_{t0}}{G_f^I}\kappa_1\right) \tag{2.38}$$

where f_{t0} is the initial tensile strength and G_f^I is the tensile fracture energy. Similarly, the evolution of the cohesion is given by same exponential softening:

$$c(\kappa_2) = c_0 exp\left(-\frac{c_0}{G_f^{II}}\kappa_2\right) \tag{2.39}$$

where c_0 is the initial cohesion and G_f^{II} is the shear fracture energy. The evolution of friction and dilatancy angles is linked to the evolution of the cohesion:

$$tan\phi(\kappa_2) = tan\phi_0 + (tan\phi_r - tan\phi_0)\left(\frac{c_0 - c}{c_0}\right) \tag{2.40}$$

$$tan\psi(\kappa_2) = tan\psi_0 + (tan\psi_r - tan\psi_0)\left(\frac{c_0 - c}{c_0}\right) \tag{2.41}$$

where ϕ_0 and ψ_0 are the initial friction and dilatancy angles, while ϕ_r and ψ_r are the residual friction and dilatancy angles.
The evolution of $f_c(\kappa_3)$ is described by a hardening-softening law in terms of plastic displacements, explained in Section 2.2.2.

2.5 Numerical modeling of shear walls

In this section, the adopted modeling strategies are used to simulate the experimental in-plane behavior of masonry shear walls Raijmakers and Vermeltfoort (1992). First, a brief description of the experimental tests is given in Section 2.5.1, then the results of each modeling strategy are described in detail. Finally Section 2.5.5 compares the adopted modeling strategies, highlighting similarities/differences and advantages/disadvantages. The analyses were performed using an enhanced version of Kratos Multiphysics Dadvand et al. (2010, 2013), a free open-source framework for the development of multidisciplinary solvers, developed at CIMNE, while pre and post-processing were done in GiD Melendo et al. (2015), also developed at CIMNE.

2.5.1 Numerical simulation of experimental test: TU Eindhoven shear wall

The geometry of the wall (here denoted as W1) as well as the boundary conditions are represented in Figure 2.15. The wall has no opening and it is made of one layer of solid bricks with dimensions $210\,mm \times 52\,mm \times 100\,mm$, with $10\,mm$ thick mortar joints Raijmakers and Vermeltfoort (1992). The wall is subjected to two load stages: (i) First, a uniform pressure is applied on the top of the wall, (ii) then a horizontal load is applied under displacement control in a confined way, keeping the top of the wall horizontal and precluding vertical displacements. The same test is performed for three different values of vertical pre-compression (0.30, 1.21 and $2.12\,N/mm^2$). The experimental failure mechanisms obtained from the tested walls are shown in Figure 2.16.

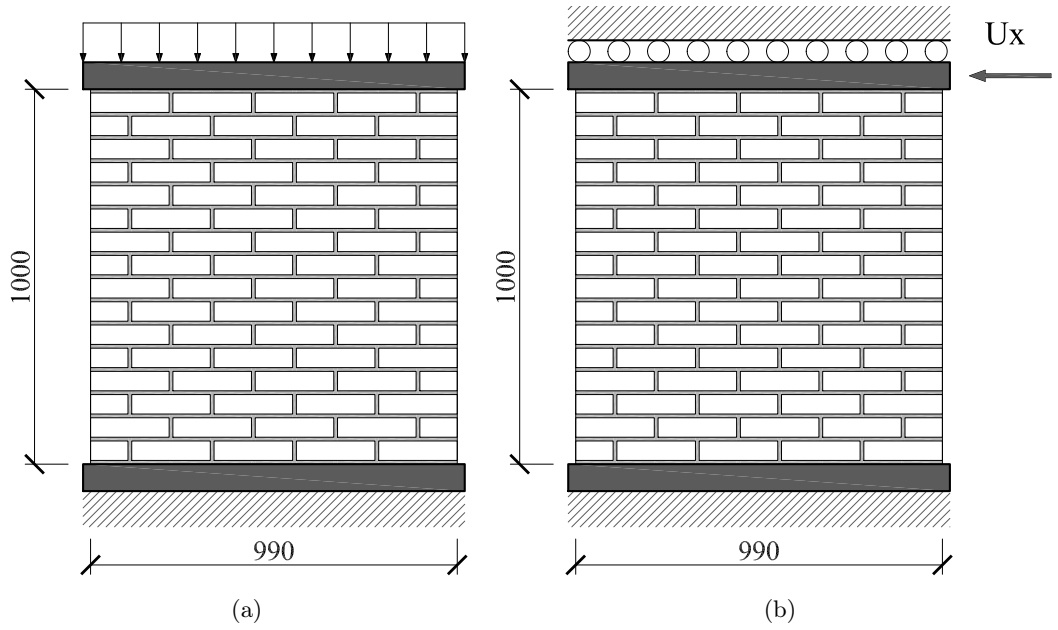

Figure 2.15: Wall W1 - TU Eindhoven shear wall Raijmakers and Vermeltfoort (1992). Geometry and loading stages: (a) stage 1: uniform vertical load $p = 0.3, 1.21, 2.12\,N/mm^2$; (b) stage 2: horizontal displacement under vertical confinement.

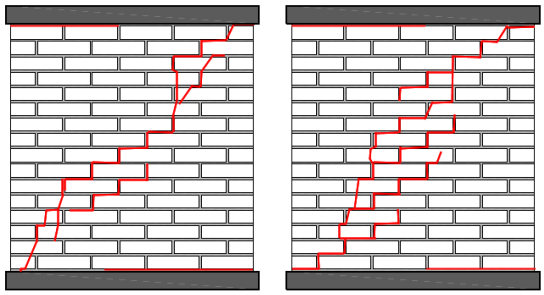

(a) $p = 0.3\,N/mm^2$ (b) $p = 0.3\,N/mm^2$

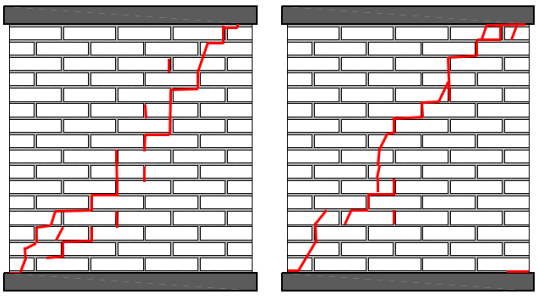

(c) $p = 1.21\,N/mm^2$ (d) $p = 2.12\,N/mm^2$

Figure 2.16: Experimental failure patterns

For each one of the three modeling strategies, three analyses are carried out, one for each level of vertical compression, for a total of nine analyses.
Each nonlinear static analysis is conducted in two stages:

1. In the first stage, a uniform pressure of $0.3/1.21/2.12\,N/mm^2$ is applied on top of the wall, under load control;

2. In the second stage, a horizontal nodal load is applied on the top-right corner of the wall, under displacement control. In this second stage, the vertical displacement on top of the wall, is kept fixed at the value reached at the previous step.

The pseudo-time is adaptively incremented from $t = 0\,s$ to $t = 1\,s$, with an initial time step of $1.0 \times 10^{-2}\,s$, and a minimum time step of $1.0 \times 10^{-9}\,s$. The duration of the two stages are respectively $0.02\,s$ and $0.98\,s$. In each time step the equilibrium is achieved

by means of a full Newton-Raphson iteration process. Convergence is accepted with a relative tolerance of the residual norm of 1.0×10^{-5}.

2.5.2 2D Continuum micro-model (2D-C)

This section reports the results obtained using the 2D-C model. Table 2.3 shows the material parameters for the damage constitutive model used for both bricks and mortar joints. Figure 2.17 shows the obtained force-displacement curves for the three levels of vertical pre-compression.

E	ν	σ_t	G_t	σ_0	σ_p	σ_r	G_c	ε_p	k_b	k_1
850.0	0.15	0.2	0.016	3.0	10.0	2.0	80.0	0.04	1.2	0.16
$\frac{N}{mm^2}$	-	$\frac{N}{mm^2}$	$\frac{N}{mm}$	$\frac{N}{mm^2}$	$\frac{N}{mm^2}$	$\frac{N}{mm^2}$	$\frac{N}{mm}$	-	-	-

(a)

E	ν	σ_t	G_t	σ_0	σ_p	σ_r	G_c	ε_p	k_b	k_1
16700.0	0.15	2.0	0.08	8.0	12.0	1.0	6.0	0.004	1.2	0.0
$\frac{N}{mm^2}$	-	$\frac{N}{mm^2}$	$\frac{N}{mm}$	$\frac{N}{mm^2}$	$\frac{N}{mm^2}$	$\frac{N}{mm^2}$	$\frac{N}{mm}$	-	-	-

(b)

Table 2.3: Model 2D-C. (a) Material properties for mortar joints (damage model); (b) Material properties for bricks (damage model)

A good agreement with experimental results are obtained, with a slight underestimation of the wall capacity for higher level of pre-compression. This is probably due to the plane-stress assumption made for both bricks and mortar joints, that becomes hardly applicable to describe the complex interaction between bricks and mortar joints under high levels of compression. Table 2.4 shows the obtained results in terms of maximum principal strain, minimum principal stress, tensile and compressive damage.

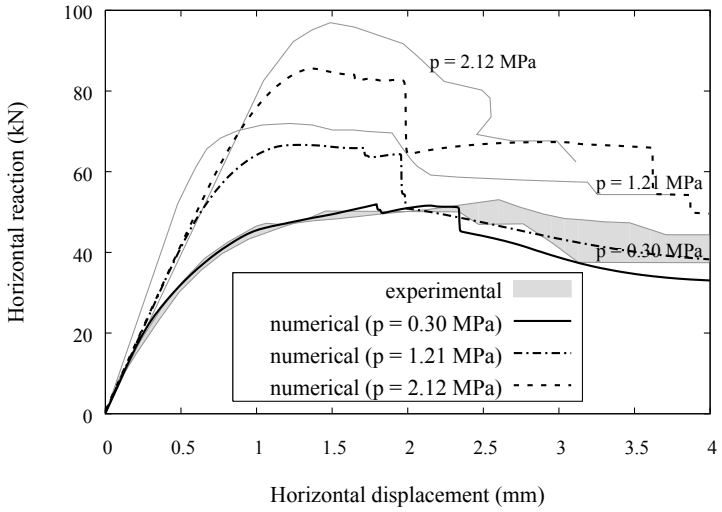

Figure 2.17: Model 2D-C. load-displacement curves for different values of pre-compression

The results obtained from the model 2D-C for a vertical compression of $0.3\,N/mm^2$ are carefully commented to explain the behavior of the shear walls and to better understand the evolution of the micro-structure up to the complete failure of the wall. To this end, five significant snapshots of the analysis are extracted. These snapshots are identified by instants $t = [0.14, 0.30, 0.47, 0.64, 1.0]\,s$, and by horizontal-top-displacements $U_x = [0.5, 1.1, 1.8, 2.5, 4.0]\,mm$. The obtained results can be seen in Figure 2.18, in terms of maximum principal strains.

The first non-linearity appears at a horizontal-top-displacement $U_x = 0.5\,mm$, with horizontal tensile cracks developing at the bottom-right and top-left parts of the wall. At a horizontal-top-displacement $U_x = 1.1\,mm$, staircase diagonal cracks appear from the center of the wall, proceeding towards the supports through the mortar joints. In this stage there are several cracks, but not yet a fully open unique crack, due to the presence of bricks that are still below their tensile peak stress. The formation of these diagonal cracks also produces the first visible change in the slope of the load-displacement curve. The stage between horizontal-top-displacements $U_x = 1.8\,mm$ and $U_x = 2.5\,mm$ is characterized by the previously mentioned cracks joining to form a unique diagonal crack that fully reaches the supports. The joining of those cracks is due to tensile failure

of bricks. The further opening of the diagonal crack leads to the full development of the shear/crushing mechanism determining the collapse of the wall.

ε_{max}	σ_{min}	d^+	d^-
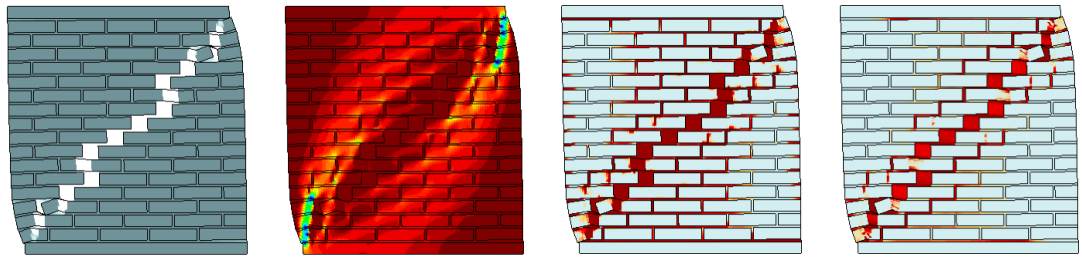			
$p = 0.3\,MPa$			
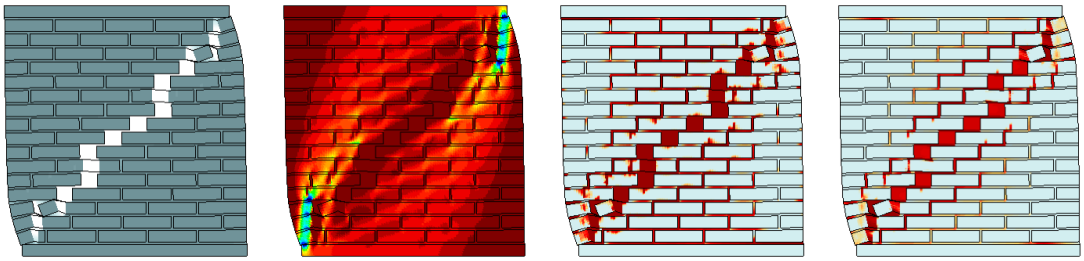			
$p = 1.21\,MPa$			
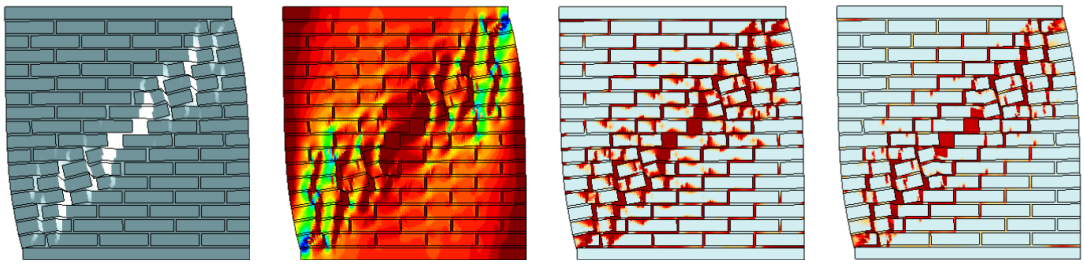			
$p = 2.12\,MPa$			

Table 2.4: Model 2D-C. Results in terms of maximum principal strains, minimum principal stresses, tensile damage and compressive damage, at the ultimate displacement $U_x = 4.0\,mm$

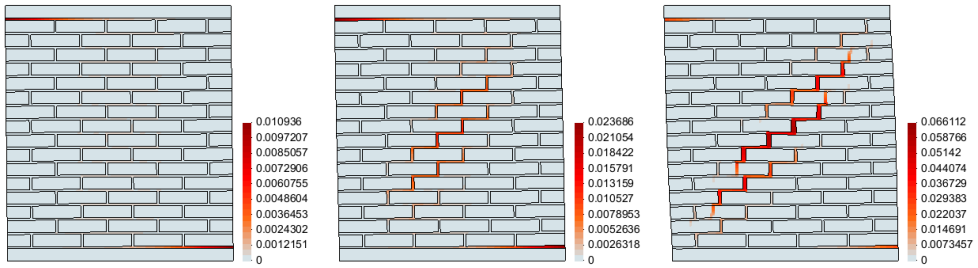

(a) $U_x = 0.5\ [mm]$ (b) $U_x = 1.1\ [mm]$ (c) $U_x = 1.8\ [mm]$

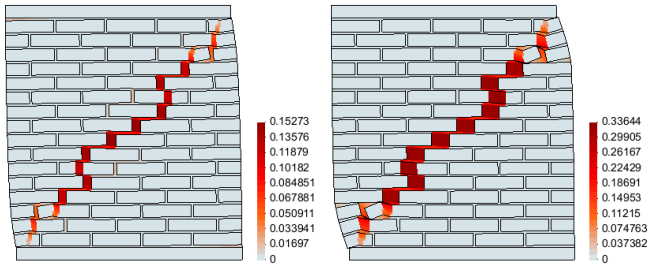

(d) $U_x = 2.5\ [mm]$ (e) $U_x = 4.0\ [mm]$

Figure 2.18: Model 2D-C, $P = 0.3\,MPa$. Incremental contour plots of maximum principal strain ε_{max}

2.5.3 2D Discrete micro-model (2D-D)

This section reports the results obtained using the 2D-D model. Table 2.5 shows the material parameters for the interface constitutive model used for mortar joints, and the elastic properties for the bricks. The potential crack in the bricks are simulated using a simple damage interface model with a tensile strength $\sigma_t = 2.0$. Figure 2.19 shows the obtained force-displacement curves for the three levels of vertical pre-compression. Also in this case, a good agreement with experimental results is reached. As opposed to the 2D-C model, the 2D-D model shows an overestimation of the wall capacity for higher level of pre-compression. This is probably due to assuming only a vertical potential crack in the bricks. This assumption is more appropriate for low values of vertical pre-compression. For higher values of pre-compression, diagonal cracks in the bricks cannot appear, and the main diagonal "crack" has to find its path through the pre-defined interfaces. Table 2.6 shows the obtained results in terms of deformed shape, minimum principal stress, tensile/shear and compressive equivalent plastic displacements.

E	ν
16700.0	0.15
$\frac{N}{mm^2}$	-

(a)

k_n	k_s	ν
82.0	36.0	0.15
$\frac{N}{mm^3}$	$\frac{N}{mm^3}$	-

(b)

f_t	G_I	c	G_{II}	$tan\phi$	$tan\psi$	σ_0	σ_p	σ_r	G_{III}	C_{ss}
0.2	0.016	0.35	0.125	0.75	0	6.0	11.0	2.0	6.0	9.0
$\frac{N}{mm^2}$	$\frac{N}{mm}$	$\frac{N}{mm^2}$	$\frac{N}{mm}$	-	-	$\frac{N}{mm^2}$	$\frac{N}{mm^2}$	$\frac{N}{mm^2}$	$\frac{N}{mm}$	-

(c)

Table 2.5: Model 2D-D. (a) Material properties for elastic bricks; (b)(c) Material properties for mortar joints (interface model)

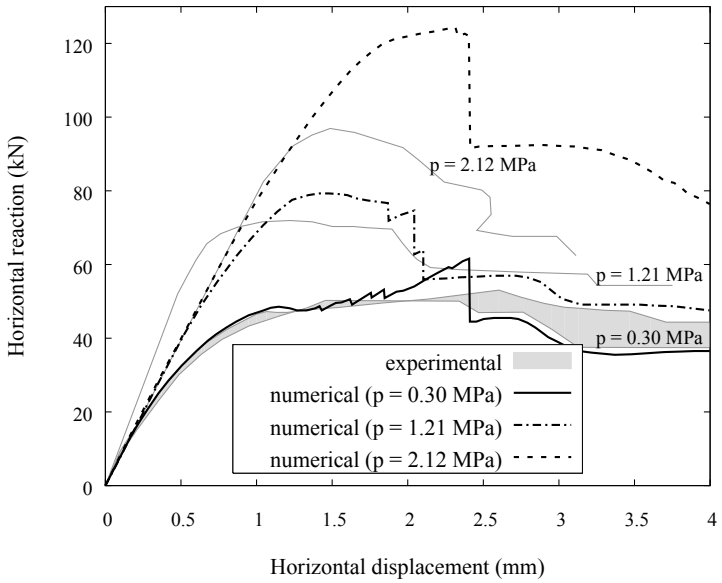

Figure 2.19: Model 2D-D. load-displacement curves for different values of pre-compression

deformed shape	σ_{min}	tensile/shear $u_{p,eq}$	compressive $u_{p,eq}$
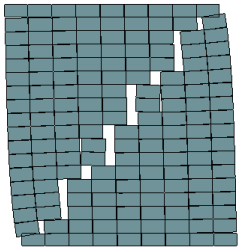	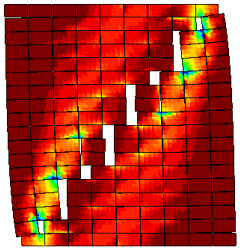	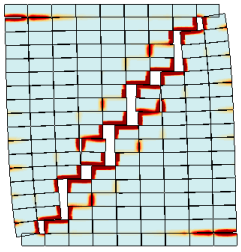	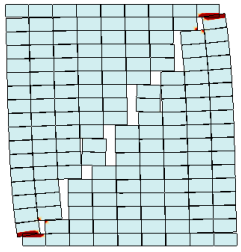
$p = 0.3\,MPa$			
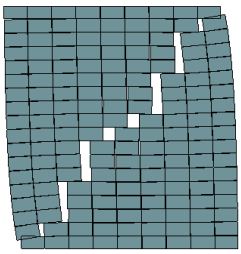	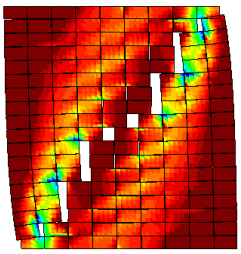	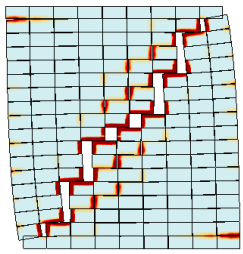	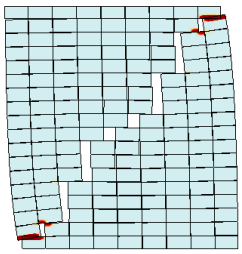
$p = 1.21\,MPa$			
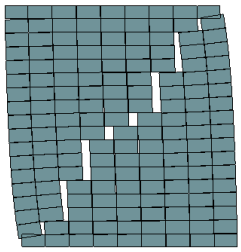	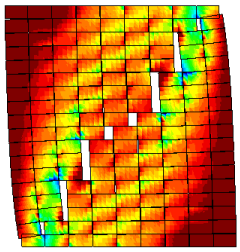	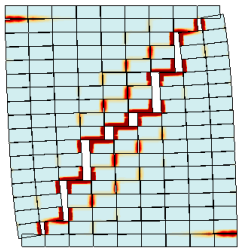	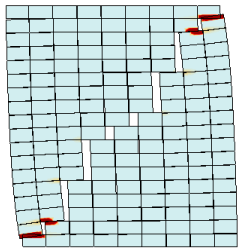
$p = 2.12\,MPa$			

Table 2.6: Model 2D-D. Results in terms of deformed shape, minimum principal stresses, tensile/shear and compressive equivalent plastic displacement, at the ultimate displacement $U_x = 4.0\,mm$

2.5.4 2D mixed Continuum/Discrete micro-model (2D-CD)

This section reports the results obtained using the 2D-CD model. Table 2.7 shows the material parameters for the interface constitutive model used for mortar joints, and for the damage model used for the bricks. Figure 2.20 shows the obtained force-displacement curves for the three levels of vertical pre-compression. A good agreement with experimental results have been obtained also in this case. As expected, this model shows a response which is in-between the 2D-C and the 2D-D models. The overestimation for higher levels of vertical pre-compression is reduced compared to the 2D-D model, by allowing more "freedom" in the possible damage pattern in the bricks.Table 2.8 shows the obtained results in terms of deformed shape, minimum principal stress, tensile/shear and compressive equivalent plastic displacements.

k_n	k_s	ν
82.0	36.0	0.15
$\frac{N}{mm^3}$	$\frac{N}{mm^3}$	-

f_t	G_I	c	G_{II}	$tan\phi$	$tan\psi$	σ_0	σ_p	σ_r	G_{III}	C_{ss}
0.2	0.016	0.35	0.125	0.75	0	6.0	11.0	2.0	6.0	9.0
$\frac{N}{mm^2}$	$\frac{N}{mm}$	$\frac{N}{mm^2}$	$\frac{N}{mm}$	-	-	$\frac{N}{mm^2}$	$\frac{N}{mm^2}$	$\frac{N}{mm^2}$	$\frac{N}{mm}$	-

(a)

E	ν	σ_t	G_t	σ_0	σ_p	σ_r	G_c	ε_p	k_b	k_1
16700.0	0.15	2.0	0.08	8.0	12.0	1.0	6.0	0.004	1.2	0.0
$\frac{N}{mm^2}$	-	$\frac{N}{mm^2}$	$\frac{N}{mm}$	$\frac{N}{mm^2}$	$\frac{N}{mm^2}$	$\frac{N}{mm^2}$	$\frac{N}{mm}$	-	-	-

(b)

Table 2.7: Model 2D-CD. (a) Material properties for mortar joints (interface model); (b) Material properties for bricks (damage model)

deformed shape	σ_{min}	tensile/shear $u_{p,eq}$	compressive $u_{p,eq}$
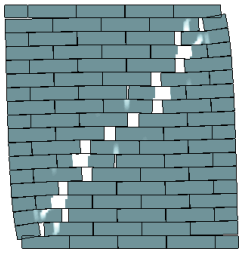	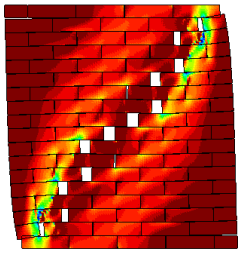	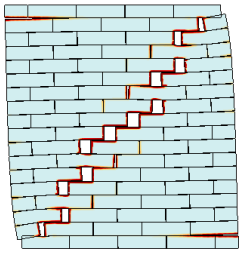	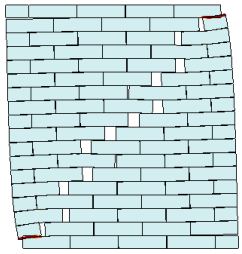
$p = 0.3\,MPa$			
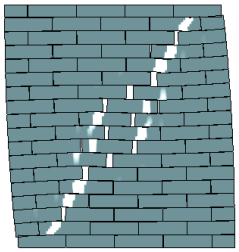	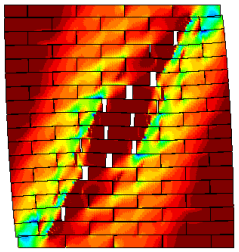	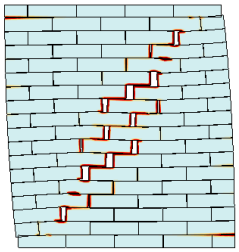	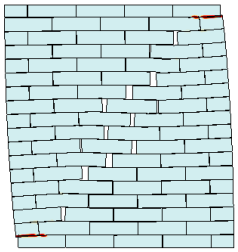
$p = 1.21\,MPa$			
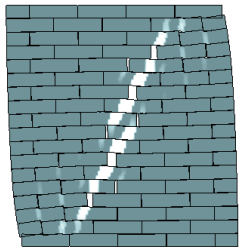	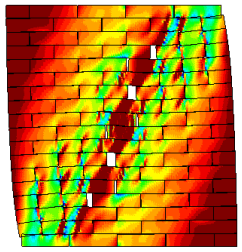	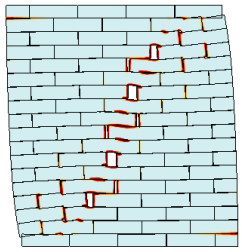	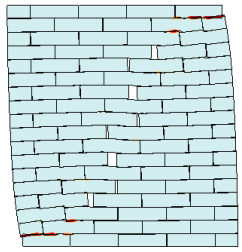
$p = 2.12\,MPa$			

Table 2.8: Model 2D-CD. Results in terms of deformed shape, minimum principal stresses, tensile/shear and compressive equivalent plastic displacement, at the ultimate displacement $U_x = 4.0\,mm$

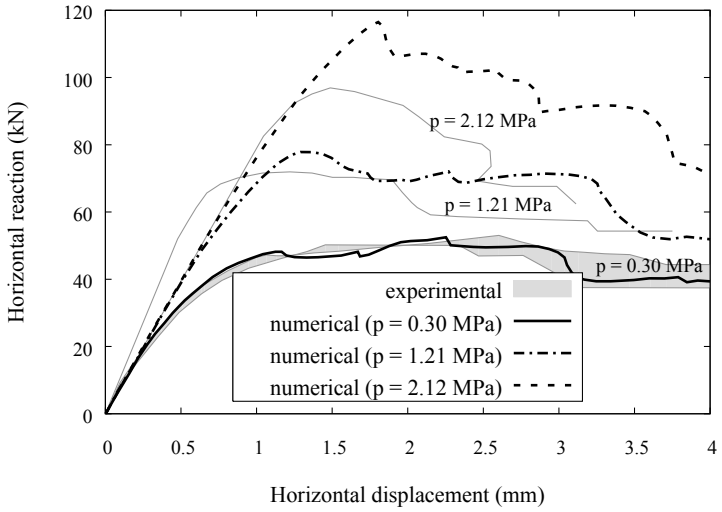

Figure 2.20: Model 2D-CD. load-displacement curves for different values of pre-compression

2.5.5 Comparison and discussion of numerical results

The presented results demonstrate that all the three selected models perform relatively well and give similar results, all in good agreement with the experimental tests. Each modeling strategy introduces simplifications with respect to a more general 3D detailed micro-modeling, thus giving slightly different results.

The model 2D-C uses a tension/compression continuum damage model for both bricks and mortar joints. This leads to a very efficient and robust analysis due to the explicit evaluation of the internal variables. The concept of dilatancy (which is of paramount importance for the simulation of shear walls) cannot be easily defined in the context of damage models, differently from the case of plasticity. Nevertheless, both failure surfaces are active in a tension/compression damage model when the two principal stresses have different sign. In this case, the Cauchy stress is not an isotropic scaling of the effective (elastic) stress. Taking advantage of this feature, a novel compressive model has been formulated to provide a satisfactory shear behavior, in terms of dilatancy and shear strength, as described in Section 2.3. The proposed model requires a careful definition of the parameter k_1 that sets the shape of the compressive failure surface in the ten-

sion/compression quadrants of the principal stresses plane. A value of 0.16 has shown to be be adequate for the investigated case studies, see Section 2.5.6. Also the novel evolution law for the compressive damage variable, based on quadratic bezier curves, has shown to be adequate for the description of the shear-compression nonlinear response of masonry.

The model 2D-D lumps all the main non-linearity in mortar joints, modeled as interface elements with a composite yield criterion based on the concept of multisurface plasticity. The dilatancy of mortar joints are easily defined due to the non-associativity of the shear mode. Another advantage is that this model separately defines the shear and compressive failure mechanisms. In this way the compressive cap criterion can be used to properly model the compressive behavior of the wall without affecting the shear behavior of the mortar joints. The choice of allowing only the tensile failure of the brick, through a vertical potential crack in the mid-section, limits the number of DOFs of the model, but at the same time it does not allow a natural failure of the bricks when a diagonal crack is likely to appear, as in cases of shear at high compression. It should be mentioned that this model takes into account the reduction in shear strength for high level of compression through the elliptical cap mode. However, this happens at the interface constitutive level but at the structural level the "crack" is forced to find its path through the predefined interfaces. This is probably the cause of overestimation of the strength of the wall for higher vertical compression levels and sudden drops as the vertical cracks in the bricks open, as can be seen in Figure 2.19.

Finally the model 2D-CD seems to join the features of both the previous models, at the price of a higher computational cost. In this model the accurate description of the mortar joint behavior is achieved with the composite interface model, while the non-linearity in the bricks is described through the continuum damage model, thus without making any assumption on the direction of the cracks in the bricks. Compared to the 2D-D model, the overestimation of the shear strength of the wall under high vertical compression is alleviated, as can be seen in Figure 2.20. This can also be seen by comparing the crack patterns obtained for each model and for each level of vertical compression, as shown in Table 2.9. Model 2D-CD shows a progressively changing direction in the main diagonal crack, becoming more vertical as the vertical compression increases, due to the propagation of diagonal cracks in the bricks, while the model 2D-D shows almost the same failure pattern for all vertical compression levels.

$P = 0.30\,N/mm^2$	$P = 1.21\,N/mm^2$	$P = 2.12\,N/mm^2$
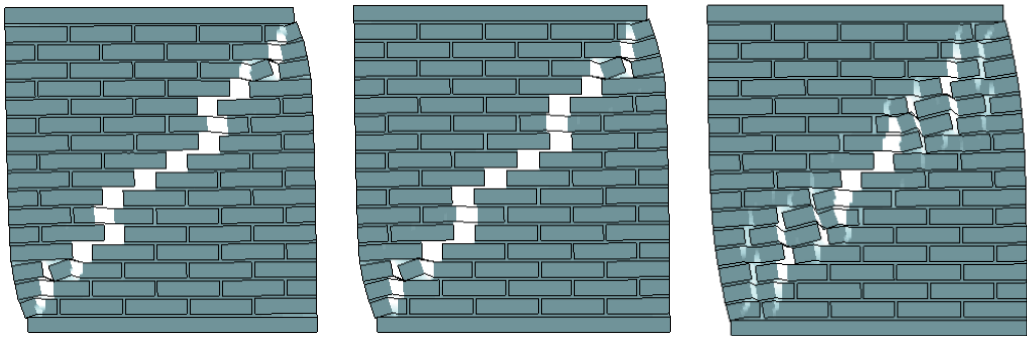		
2D Continuum meso-model (2D-C)		
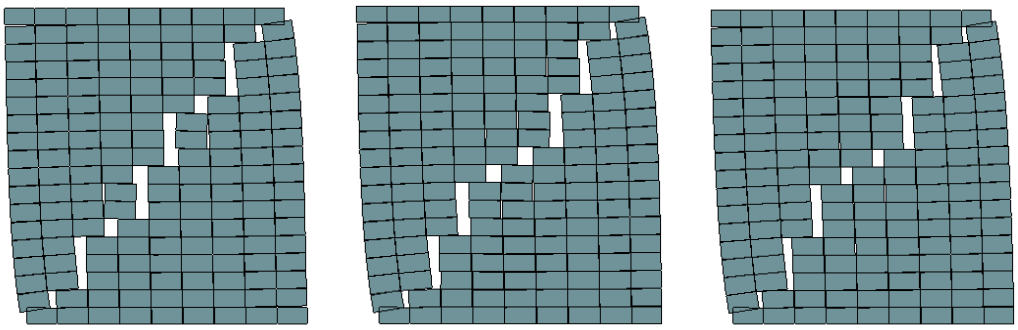		
2D Discrete micro-model (2D-D)		
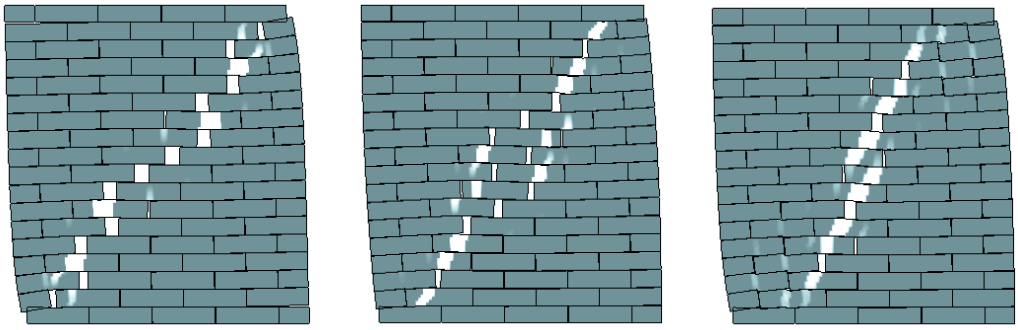		
2D Mixed Continuum/Discrete micro-model (2D-CD)		

Table 2.9: comparison of failure patterns

2.5.6 Dilatant behavior in the continuum micro-model 2D-C

This section presents a further assessment of the tension/compression damage model proposed for the 2D-C model. A parametric study is carried out to evaluate the model's capability of handling the dilatant behavior of mortar joints. The effect of the compressive surface on the global response of the wall is evaluated.
For the 2D-C modeling strategy, with the lowest of the three vertical compression levels, $0.3\,N/mm^2$, three analyses have been carried out, varying the k_1 parameter in Eq. (2.5). Three values have been selected: 0.0, 0.16, and 1.0. Recalling that this parameter affects the shape of the compressive surface in tension/compression quadrants, the value of 0.0 leads to a Drucker-Prager criterion, while the value of 1.0 leads to the Lubliner criterion Lubliner et al. (1989). The intermediate value of 0.16 has been found as optimal for the required dilatancy. The results of the three analyses are shown in Figure 2.21 in terms of global force-displacement response, and in Figure 2.22 in terms of maximum principal strains. As expected the Drucker-Prager criterion ($k_1 = 0$) overestimates the dilatancy of the model, and since no vertical displacement is allowed on top of the wall while loaded in shear, this induces an excessive state of compression to the material with a consequent overestimation of the global strength, as well as a more brittle behavior. Furthermore the crack pattern clearly shows how the slip of mortar joints is inhibited, while a unique diagonal crack opens through the bricks. On the contrary, a k_1 value of 1.0 makes the compressive surface very close to the tensile one in the tension/compression quadrants. In this case the dilatancy of mortar joints is not captured at all, and consequently the global shear strength of the model is largely underestimated. The failure in this case is almost only due to slip of mortar joints in the middle of the wall, and only when the crack reaches the boundaries of the wall, it finally propagates vertically through the bricks. On the other hand, the case with $k_1 = 0.16$ provides a more realistic result, by giving a better estimate of the dilatancy of mortar joints.

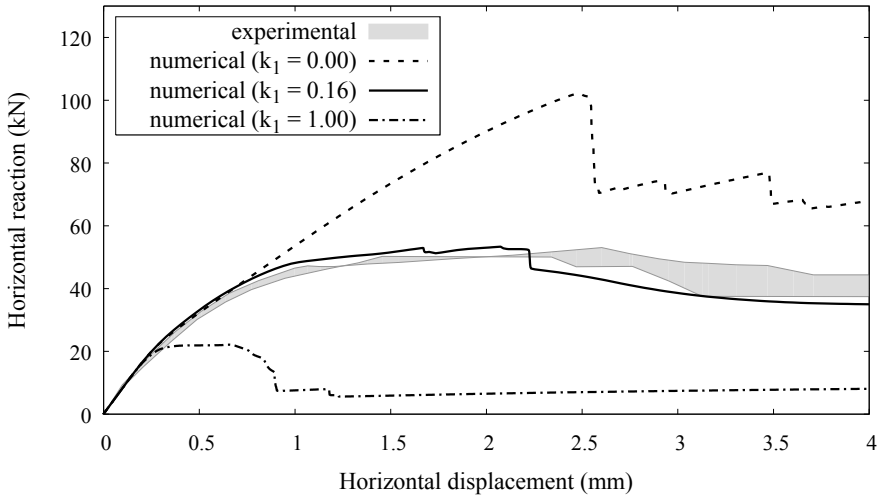

Figure 2.21: Model 2D-C, $p = 0.3\,N/mm^2$. Force-displacement curves for three different values of k_1

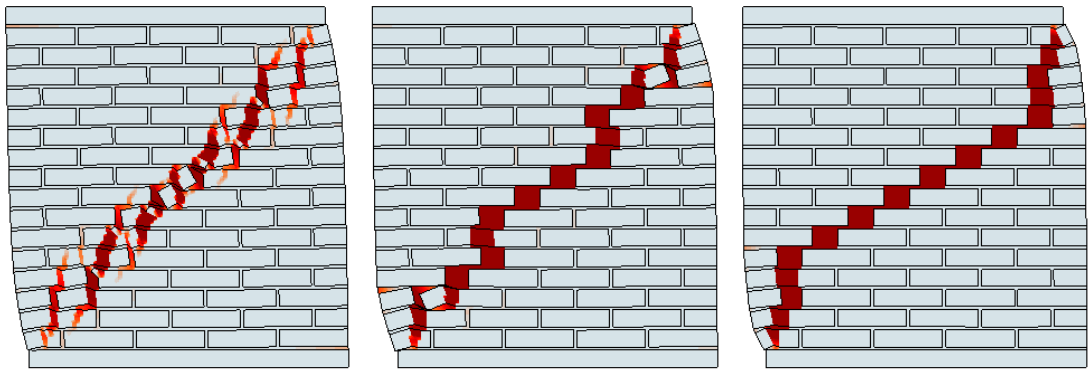

(a) $k_1 = 0.0$ (b) $k_1 = 0.16$ (c) $k_1 = 1.0$

Figure 2.22: Model 2D-C, $p = 0.3\,N/mm^2$. Failure patterns for three different values of k_1

This page is intentionally left blank

Chapter 3

Regularization of first order computational homogenization

This chapter gives a brief summary of the main concepts and basic equations of classical first order computational homogenization, where a standard first order continuum theory is assumed in both scales. It then investigates the possibility of using first order computational homogenization together with a simple regularization procedure based on the fracture energy of the micro-scale-constituents. A generalized geometrical characteristic length takes into account the size of the macro-scale element as well as the size of the RVE (and its constituents).

The formulation of phenomenological closed-form constitutive models for the analysis of heterogeneous quasi-brittle materials such as masonry is still a challenging task Pelà et al. (2011, 2013). The evolution of macroscopic properties is highly influenced by complex micro-structural phenomena, especially when strain localizations occur in the micro-structure leading to complex dissipation mechanisms at the structural level.

There are three main approaches to model this kind of heterogeneous materials, introduced in Chapter 1 and briefly recalled here.

The first approach is the Direct Numerical Simulation (DNS) where a classical 1-scale FE model is used, and all the information about the micro-structure is explicitly modeled. An interface model using multisurface plasticity was proposed in Lourenço and Rots (1997) to describe the in-plane behavior of masonry. In this kind of modeling, both bricks and mortar joints are explicitly modeled, and all nonlinear behaviors are lumped in the interface elements. This approach is very efficient with small-scale structures, but

it soon becomes unaffordable for large-scale time consuming analyses.

The second approach is known as Concurrent Multiscale Method (CMM). As a multiscale model, it involves the study of multiple length scales as well as the exchange of information among them. The micro-structural scale is adaptively inserted and resolved in the structural model, establishing a strong coupling between macro and micro scales. Works on this subject can be found in Lloberas-Valls et al. (2011, 2012), Lloberas-Valls (2013), among others.

The third approach is known as Computational Homogenization Method (CHM). Similar to the CMM, it is based on multiscale modeling. Assuming that the length scales are separated, this approach establishes a weak coupling between them. The micro-structural features are not physically inserted in the structural model, as in the case of CMM, but they are modeled into a so called representative volume element (RVE) which is associated to each integration point of the macroscopic mesh. The RVE is then used to extract a homogenized response to the macroscopic strain field, thus emulating an equivalent homogeneous medium. This model has been used to model a large class of materials characterized by complex micro-structures, with linear and nonlinear behaviors Miehe et al. (1999), Fritzen et al. (2013), Otero et al. (2012, 2015), Quinteros et al. (2012), Oller et al. (2005), Car et al. (2002), Zucchini and Lourenço (2002, 2009).

However, it was soon recognized to give non-objective results when dealing with strain-softening materials. In fact the RVE looses its representativeness upon strain localization. In the last years, several modifications to the classical CHM were proposed, and a review on recent developments can be found in Nguyen et al. (2011) and in the references therein. Some approaches regularize the response of the RVE by using a higher order theory at the macro-scale, such that the information about a material characteristic length is naturally taken into account Geers et al. (2003), Kouznetsova et al. (2004, 2002), De Bellis (2009), De Bellis and Addessi (2011), Trovalusci and Masiani (2003), Addessi et al. (2010). Others, known as continuous-discontinuous approaches, up-scale the RVE response to a traction-separation law (upon strain localization) used by a discontinuity inserted into the macro-scale model Massart (2003), Massart et al. (2007), Mercatoris et al. (2009), Mercatoris and Massart (2011), Oliver et al. (2014b,a), Belytschko et al. (2008), Bosco et al. (2015). Another issue related to the loss of representativeness of the RVE is the choice of proper boundary conditions to be applied on the RVE. A study on this topic was done in Coenen et al. (2012), where a novel boundary condition was proposed, using the concept of rotating periodicity to avoid

constraining the crack propagation orientation.
In the context of masonry modeling, works on continuous-discontinuous computational homogenization can be found in Massart et al. (2007), Massart (2003) for modeling the in-plane behavior of masonry structures, and later on extended to the study of shell elements for the analysis of the out-of-plane behavior Mercatoris et al. (2009), Mercatoris and Massart (2011), while works on computational homogenization using a Cosserat continuum at the macro-scale can be found in De Bellis (2009), De Bellis and Addessi (2011).
Previous approaches based on first order homogenization and fracture energy regularization considered the characteristic length used in the micro-structural constitutive models equal to the characteristic length of the macro-scale finite elements Badillo (2012). The same was done in De Bellis (2009) to compare the classical first order homogenization with the Cosserat-based homogenization. This chapter proposes an extension of the fracture energy-based regularization to two-scale computational homogenization based on classical first order continuum theory. The main aim is to allow the usage of first order computational homogenization for the analysis of quasi-brittle micro-structures. The main novelty of the proposed approach resides in the consistent definition of a fracture energy based regularization, in order to account for the characteristic lengths of the finite elements at both scales, as well as the size of the RVE.

3.1 Classical first order computational homogenization

The main work-flow of the classical CHM can be represented as in Figure 3.1.
The procedure can be defined by three main steps:

1. *Down-scaling* or *macro-micro transition*, where the macroscopic strain at any point of the macroscopic mesh, are transferred to the micro-scale, where they are used to apply boundary conditions on the RVE mesh;

2. *Solution of the micro-scale Boundary Value Problem* (BVP), which can be done through any numerical method, but here FEM is considered;

3. *Up-scaling* or *micro-macro transition*, where the macro-scale stress tensor and the macro-scale tangent operator are obtained via homogenization procedures.

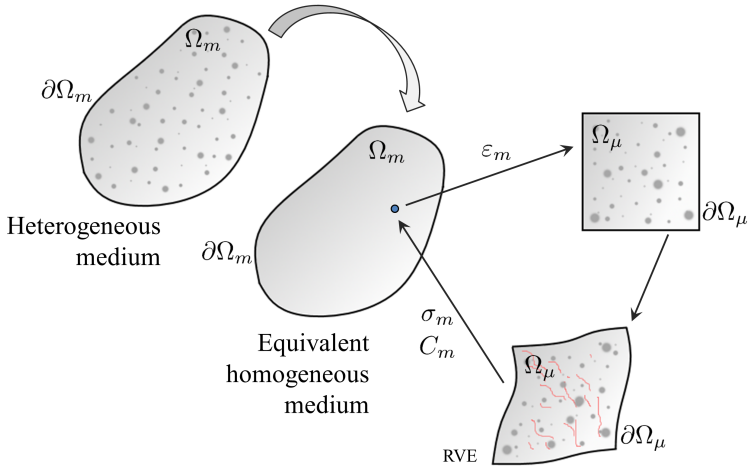

Figure 3.1: work-flow of classical computational homogenization

3.2 Down-scaling or macro-micro transition

The starting point for a kinematically based computational homogenization method is to assume that the macroscopic strain $\boldsymbol{\varepsilon}_m$, in each point $\boldsymbol{x}_m$ of the macro-scale domain and at each instant t, can be obtained as the volume average of the microscopic strain field $\boldsymbol{\varepsilon}_\mu$ defined at each point $\boldsymbol{x}_\mu$ of the micro-scale domain and at each instant t:

$$\boldsymbol{\varepsilon}_m(\boldsymbol{x}_m, t) = \frac{1}{V_\mu} \int_{\Omega_\mu} \boldsymbol{\varepsilon}_\mu(\boldsymbol{x}_\mu, t)\, \mathrm{d}V \tag{3.1}$$

The microscopic strain field can be expressed as the symmetric gradient of the microscopic displacement field $\boldsymbol{u}_\mu$, thus Eq. (3.1) can be rewritten as

$$\boldsymbol{\varepsilon}_m(\boldsymbol{x}_m, t) = \frac{1}{V_\mu} \int_{\Omega_\mu} \nabla^s \boldsymbol{u}_\mu\, \mathrm{d}V \tag{3.2}$$

or equivalently using the Gauss theorem

$$\boldsymbol{\varepsilon}_m(\boldsymbol{x}_m, t) = \frac{1}{V_\mu} \int_{\partial\Omega_\mu} \boldsymbol{u}_\mu \otimes_s \boldsymbol{n}\, \mathrm{d}A \tag{3.3}$$

being $\boldsymbol{n}$ the outward unit normal field on the RVE boundary $\partial\Omega_\mu$. It is assumed that

the microscopic displacement field can be additively split into a linear part (coarse scale contribution) and a fluctuating part $\tilde{\boldsymbol{u}}_\mu$ (fine scale contribution)

$$\boldsymbol{u}_\mu(\boldsymbol{x}_\mu, t) = \boldsymbol{\varepsilon}_m(\boldsymbol{x}_m, t)\boldsymbol{x}_\mu + \tilde{\boldsymbol{u}}_\mu(\boldsymbol{x}_\mu, t) \tag{3.4}$$

and in the same way the microscopic strain field can be split into a constant part (coarse scale contribution) and a fluctuating part $\tilde{\varepsilon}_\mu$(fine scale contribution)

$$\boldsymbol{\varepsilon}_\mu(\boldsymbol{x}_\mu, t) = \boldsymbol{\varepsilon}_m(\boldsymbol{x}_m, t) + \tilde{\boldsymbol{\varepsilon}}_\mu(\boldsymbol{x}_\mu, t) \tag{3.5}$$

Inserting the definition of the microscopic strain field (Eq. (3.5)) into the definition of the macroscopic strain field (Eq. (3.1)), and taking into account that the macroscopic strain field is constant over the RVE, and the microscopic strain fluctuation field can be written as the symmetric gradient of the microscopic displacement fluctuation field, one obtains:

$$\boldsymbol{\varepsilon}_m(\boldsymbol{x}_m, t) = \boldsymbol{\varepsilon}_m(\boldsymbol{x}_m, t) + \frac{1}{V_\mu}\int_{\Omega_\mu} \nabla^s \tilde{\boldsymbol{u}}_\mu \, \mathrm{d}V \tag{3.6}$$

For Eq. (3.6) to be satisfied, it is required that the integral of the microscopic displacement fluctuation field over the RVE domain vanishes:

$$\int_{\Omega_\mu} \nabla^s \tilde{\boldsymbol{u}}_\mu \, \mathrm{d}V = 0 \tag{3.7}$$

or equivalently using the Gauss theorem:

$$\int_{\partial\Omega_\mu} \tilde{\boldsymbol{u}}_\mu \otimes_s \boldsymbol{n} \, \mathrm{d}A = 0 \tag{3.8}$$

Eq. (3.8) provides the minimal kinematic constraint that a microscopic displacement fluctuation field should satisfy to be kinematically admissible.

The last step of the macro-micro transition is to define the boundary conditions to be applied on the RVE displacement fluctuation field, in order for the micro-BVP to be solved. Following the work in De Souza Neto and Feijóo (2006), typical *subsets of kinematically admissible microscopic displacement fluctuations* are briefly summarized in the following.

Zero displacement fluctuations:

$$\tilde{\boldsymbol{u}}_\mu(\boldsymbol{x}_\mu, t) = 0 \quad \forall \boldsymbol{x}_\mu \in \Omega_\mu \tag{3.9}$$

This model forces the displacement fluctuations to vanish in every point of the RVE domain, thus the whole RVE undergoes a uniform strain equal to the macro-scale strain field.

Zero boundary displacement fluctuations:

$$\tilde{\boldsymbol{u}}_\mu(\boldsymbol{x}_\mu, t) = 0 \quad \forall \boldsymbol{x}_\mu \in \partial\Omega_\mu \tag{3.10}$$

This model forces the displacement fluctuations to vanish only on the boundaries of the RVE.

Periodic boundary displacement fluctuations:

$$\tilde{\boldsymbol{u}}_\mu(\boldsymbol{x}_\mu^+, t) = \tilde{\boldsymbol{u}}_\mu(\boldsymbol{x}_\mu^-, t) \quad \forall\, pair\, \{\boldsymbol{x}_\mu^+,\, \boldsymbol{x}_\mu^-\} \in \partial\Omega_\mu \tag{3.11}$$

being $\boldsymbol{x}_\mu^+$ and $\boldsymbol{x}_\mu^-$ two opposite points on the RVE boundary$\partial\Omega_\mu$. This model constraints the displacement fluctuations on the boundaries of the RVE to be periodic.

Minimally constrained boundary displacement fluctuations or Uniform boundary traction:

$$\boldsymbol{\sigma}_\mu(\boldsymbol{x}_\mu, t)\boldsymbol{n}(x_\mu) = \boldsymbol{\sigma}_m(\boldsymbol{x}_m, t)\boldsymbol{n}(x_\mu) \quad \forall \boldsymbol{x}_\mu \in \partial\Omega_\mu \tag{3.12}$$

Where $\boldsymbol{\sigma}_\mu(\boldsymbol{x}_\mu, t)$ is the microscopic stress field. As shown in De Souza Neto and Feijóo (2006), the distribution of stresses on the RVE boundaries, reactive to the minimal kinematic constraint given in Eq. (3.8), satisfies Eq. (3.12). In fact, in a kinematically-based framework, the traction boundary condition in Eq. (3.12) is not explicitly imposed, but it's a direct consequence of enforcing the minimal kinematic constraint given in Eq. (3.8).

3.3 Solution of the micro-scale BVP

Assuming that inertia forces are negligible, the *Principle of Virtual Work* establishes that the RVE is in equilibrium if and only if the variational equation

$$\int_{\Omega_\mu} \boldsymbol{\sigma}_\mu(\boldsymbol{x}_\mu, t) \colon \nabla^s \boldsymbol{\eta} \, \mathrm{d}V - \int_{\Omega_\mu} \boldsymbol{b}(\boldsymbol{x}_\mu, t) \cdot \boldsymbol{\eta} \, \mathrm{d}V - \int_{\partial\Omega_\mu} \boldsymbol{t}^e(\boldsymbol{x}_\mu, t) \cdot \boldsymbol{\eta} \, \mathrm{d}A = 0 \quad \forall \boldsymbol{\eta} \in \mathscr{V}_\mu \tag{3.13}$$

holds at each instant t. In Eq. (3.13), $\boldsymbol{b}(\boldsymbol{x}_\mu, t)$ is the body force field in the RVE domain, $\boldsymbol{t}^e(\boldsymbol{x}_\mu, t)$ is the external traction field on the boundaries of the RVE, and $\mathscr{V}_\mu$ is an appropriate space of virtual displacements $\boldsymbol{\eta}$ of the RVE, subjected to one of the constraints defined in Section 3.2.

A key ingredient in the definition of multiscale constitutive models is the *Hill-Mandel Principle of Macro-Homogeneity* Hill (1965), Mandel (1971), an energy average theorem establishing that the macroscopic stress power must equal the volume average of the microscopic stress power over the RVE

$$\boldsymbol{\sigma}_m \colon \dot{\boldsymbol{\varepsilon}}_m = \frac{1}{V_\mu} \int_{\Omega_\mu} \boldsymbol{\sigma}_\mu \colon \dot{\boldsymbol{\varepsilon}}_\mu \, \mathrm{d}V \tag{3.14}$$

for any kinematically admissible microscopic strain rate field $\dot{\boldsymbol{\varepsilon}}_\mu$, i.e. (following the additive split between coarse scale and fine scale contributions) for any microscopic strain rate field of the form:

$$\dot{\boldsymbol{\varepsilon}}_\mu = \dot{\boldsymbol{\varepsilon}}_m + \nabla^s \dot{\tilde{\boldsymbol{u}}}_\mu \quad \forall \dot{\tilde{\boldsymbol{u}}}_\mu \in \mathscr{V}_\mu \tag{3.15}$$

As proved in De Souza Neto and Feijóo (2006), the Hill-Mandel Principle is equivalent to requiring that body forces and surface traction in the RVE be purely reactive, i.e. they are reaction to the chosen kinematic constraints, and cannot be prescribed independently. In this way the RVE equilibrium reduces to:

$$\int_{\Omega_\mu} \boldsymbol{\sigma}_\mu(\boldsymbol{x}_\mu, t) \colon \nabla^s \boldsymbol{\eta} \, \mathrm{d}V = 0 \tag{3.16}$$

3.4 Up-scaling or micro-macro transition

The last step in the homogenization procedure consists in finding the homogenized macroscopic stress tensor (and if required the homogenized tangent operator) after the RVE equilibrium is found. As shown in Hernández et al. (2012), Ortolano et al. (2013), a definition of the homogenized stress tensor can be derived directly from the Hill-Mandel

Principle and the additive split of the microscopic strain, and not as an assumption of the model. Inserting the split of the microscopic strain rate given in Eq. (3.15), into the Hill-Mandel Principle Eq. (3.14), the following relation is obtained:

$$\boldsymbol{\sigma}_m : \dot{\boldsymbol{\varepsilon}}_m = \frac{1}{V_\mu} \int_{\Omega_\mu} \boldsymbol{\sigma}_\mu : \dot{\varepsilon}_m \, \mathrm{d}V + \frac{1}{V_\mu} \int_{\Omega_\mu} \boldsymbol{\sigma}_\mu : \nabla^s \dot{\tilde{\boldsymbol{u}}}_\mu \, \mathrm{d}V \quad \forall \dot{\tilde{\boldsymbol{u}}}_\mu \in \mathscr{V}_\mu \tag{3.17}$$

which is valid for any kinematically admissible $\dot{\tilde{\boldsymbol{u}}}_\mu$, and for the case of $\dot{\tilde{\boldsymbol{u}}}_\mu = 0$, the following relation is obtained:

$$\boldsymbol{\sigma}_m : \dot{\boldsymbol{\varepsilon}}_m = \frac{1}{V_\mu} \int_{\Omega_\mu} \boldsymbol{\sigma}_\mu : \dot{\varepsilon}_m \, \mathrm{d}V \quad \forall \dot{\varepsilon}_m \tag{3.18}$$

which is valid for any macroscopic strain rate field, leading to:

$$\boldsymbol{\sigma}_m = \frac{1}{V_\mu} \int_{\Omega_\mu} \boldsymbol{\sigma}_\mu(\boldsymbol{x}_\mu, t) \, \mathrm{d}V \tag{3.19}$$

Thus the homogenized macroscopic stress tensor can be obtained as the volume average of the microscopic stress field of the RVE.

3.5 Interpretation and comparison with other multiscale methods

CHM allows a straightforward interpretation within the framework of Variational Multiscale Methods (VMM). The main idea is to consider that the continuous displacement field $\boldsymbol{u}$ can be decomposed into a coarse and a fine component as

$$\boldsymbol{u} = \bar{\boldsymbol{u}} + \tilde{\boldsymbol{u}} \tag{3.20}$$

where $\bar{\boldsymbol{u}}$ is defined as the "coarse" scale contribution (i.e. the one described by the coarse FE mesh) and $\tilde{\boldsymbol{u}}$ is the "fine" scale contribution (i.e. the one that would correspond to a detail that cannot be solved by the coarse FE mesh). The corresponding test functions are named $\bar{w}$ and $\tilde{w}$. Using such decomposition the strain $\boldsymbol{\varepsilon} \coloneqq \nabla^s \boldsymbol{u}$ becomes

$$\boldsymbol{\varepsilon} = \nabla^s \bar{\boldsymbol{u}} + \nabla^s \tilde{\boldsymbol{u}} \tag{3.21}$$

To follow the standard multiscale procedure Hughes et al. (1998), one shall at this point

introduce a model to obtain $\tilde{\boldsymbol{u}}$. This can be done by applying the Galerkin approach at the level of the fine scale to give

$$\int_{\Omega} \tilde{w} \nabla \cdot \boldsymbol{\sigma} \left(\nabla^s \tilde{\boldsymbol{u}} \right) \, \mathrm{d}V = \int_{\Omega} \tilde{w} \boldsymbol{f} \, \mathrm{d}V - \int_{\Omega} \tilde{w} \nabla \cdot \boldsymbol{\sigma} \left(\nabla^s \bar{\boldsymbol{u}} \right) \, \mathrm{d}V \tag{3.22}$$

which defines a "fine" scale problem which can be eventually solved if one, as in our case, provides a suitable discretization of the fine scale domain (that is, a way to actually compute $\tilde{w}$). The problem is completed once one prescribes a suitable Boundary Condition for $\tilde{\boldsymbol{u}}$. In the VMM community it is customary to assume that $\int_{\Omega} \tilde{w} \left(\nabla^s \tilde{\boldsymbol{u}} \right) \, \mathrm{d}V = 0$ which can be reworked (by applying the Green-Gauss theorem) to give

$$\int_{\partial\Omega} \tilde{w} \left(\tilde{\boldsymbol{u}} \otimes_s \boldsymbol{n} \right) \, \mathrm{d}A = 0 \tag{3.23}$$

In the case of CHM, $\tilde{w}$ can be considered as a discontinuous function defined (locally in each integration point) by the Finite Element discretization of the RVE. Under this assumption, Eq. (3.22) and Eq. (3.23) can be restricted to the RVE volume to give the Finite Element problem

$$\int_{\Omega_{RVE}} \tilde{w} \nabla \cdot \boldsymbol{\sigma} \left(\nabla^s \tilde{\boldsymbol{u}} \right) \, \mathrm{d}V = \int_{\Omega_{RVE}} \tilde{w} \boldsymbol{f} \, \mathrm{d}V - \int_{\Omega_{RVE}} \tilde{w} \nabla \cdot \boldsymbol{\sigma} \left(\nabla^s \bar{\boldsymbol{u}} \right) \, \mathrm{d}V \tag{3.24}$$

$$\int_{\partial\Omega_{RVE}} \tilde{w} \left(\tilde{\boldsymbol{u}} \otimes_s \boldsymbol{n} \right) \, \mathrm{d}A = 0 \tag{3.25}$$

Interestingly, Eq. (3.25) coincides with the so called "minimal" boundary conditions for $\tilde{\boldsymbol{u}}$. Observe that both $\tilde{\boldsymbol{u}} = 0$ (in $\partial\Omega_{RVE}$) and the constraint of $\tilde{\boldsymbol{u}}$ being periodic (in $\partial\Omega_{RVE}$) are special cases that comply with this boundary condition. Observe also that no assumption on the periodicity of $\tilde{\boldsymbol{u}}$ is needed when deriving minimal boundary conditions.

3.6 Fracture-energy-based regularization in two-scale FE Computational Homogenization

An essential aspect in numerical modeling is mesh objectivity, defined as the requirement that the results must be independent of the adopted discretization.

In a continuum which exhibits strain-softening, the strain localizes into a narrow zone where energy is dissipated according to its size, while outside the material unloads

elastically. On the other hand, in the FEM context, if standard local continuum models are used (i.e. the material response is computed as a function of local strains), this localization zone is related to the domain (volume or area) of each finite element. Thus, if strain softening appears, the dissipative domain will coincide with only one strip of elements through the finite element mesh, but since the dissipation of the total energy is proportional to the size of the finite elements, the energy dissipated would diminish as the elements become smaller upon mesh refinement, leading to non-objective results that depend on the FE size.

A solution to this problem, now widely used, was proposed first in Bažant and Oh (1983), and later on addressed by several authors (Cervera and Chiumenti (2006), Oliver (1989), Oller (2001), among others). The authors point out that in a FEM framework, the concept of strain softening should not be considered as a characteristic of the material alone, since it is related to both the fracture energy G_f and the size of the finite element where the energy dissipation occurs. The computational width of the fracture process is computed in each element depending on its geometry and dimension. This computational width is known as the element characteristic length l_{ch}. According to this model, the softening law depends on both the material fracture energy per unit of crack surface area G_f and the element characteristic length l_{ch}, in such a way that the following relation holds:

$$G_f = \frac{W}{A} = \frac{W}{V} l_{ch} = g_f \, l_{ch} \tag{3.26}$$

where W is the total energy dissipated by the fracture process, A is the crack surface area, g_f is the fracture energy per unit of volume, and V is the volume of the dissipative zone.

Referring to the notations given in Figure 3.2, Eq. (3.26) can be rewritten as:

$$G_f = \frac{W}{ht} = \frac{W}{htl_{ch}} l_{ch} = g_f \, l_{ch} \tag{3.27}$$

In two-scale FE analysis, the concept of characteristic length of the parent element (the element containing the constitutive law that needs to be regularized) is not so obvious, in the sense that the non-linear behavior is generated by a constitutive model associated to a domain of the micro-scale, but the dissipation finally occurs in a domain of the

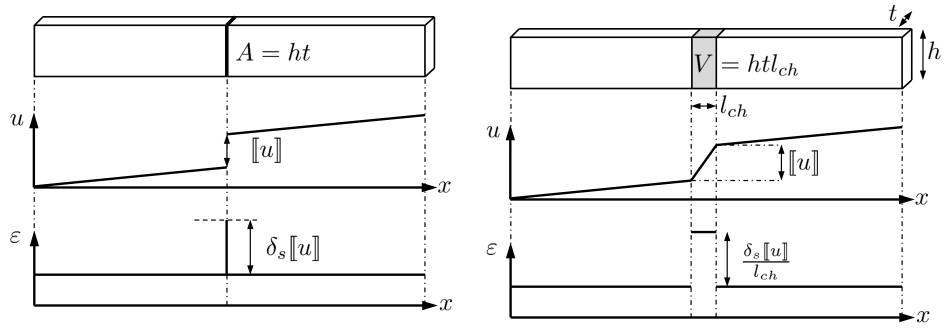

(a) strong discontinuity (b) regularized smeared discontinuity

Figure 3.2: representation of displacement and strain fields in mode I fracture, and the regularization process

macro-scale. If one considers only the characteristic length of the FE in the micro-scale, one would obtain a correct dissipation in the RVE, but then, changing the size of the RVE or the size of the FE at the macro-scale, one would obtain non-objective responses at the macro-scale. Both requirements of mesh-objectivity and correct dissipation can be satisfied only if a regularization is employed in both scales of the analysis.

This suggests that the regularization parameter for the constitutive model used in the micro-scale should be adjusted to take into account the nested feature of the multiscale homogenization procedure. As a starting point we can assume that the constitutive law at the micro-scale should be regularized using a modified characteristic length $\widetilde{l}_{ch,\mu}$, defined as a function of all the characteristic lengths that may enter into the problem (see Figure 3.3):

$$\widetilde{l}_{ch,\mu} = f(l_{ch,\mu},\, l_{ch,m},\, l_{ch,RVE}) \tag{3.28}$$

where $l_{ch,\mu}$is the characteristic length of the FE in the micro-scale, $l_{ch,m}$ is the characteristic length of the FE in the macro-scale, and $l_{ch,RVE}$ is the characteristic length of the RVE itself. The characteristic length of the FE (both at the micro and at the macro scale) has to be always computed according to the geometry, interpolation and integration scheme of the considered finite element Rots (1988).

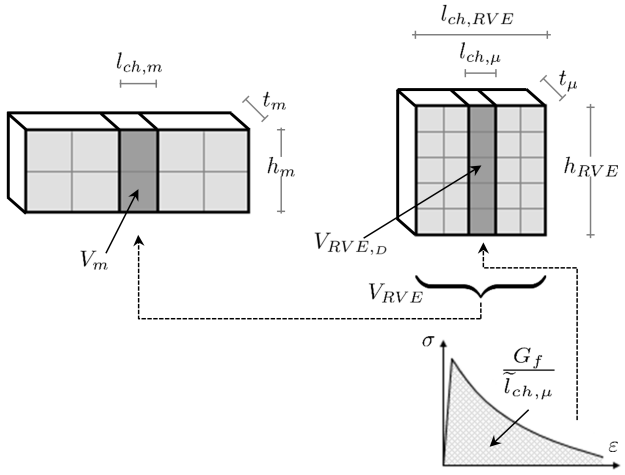

Figure 3.3: fracture energy based regularization in 2-scale FEM

To obtain a definition for the modified characteristic length, we can define the energy $W_{RVE_{,D}}$ dissipated in the damaged domain of the RVE as:

$$W_{RVE_{,D}} = \frac{G_f}{\widetilde{l}_{ch,\mu}} V_{RVE,D} = \frac{G_f}{\widetilde{l}_{ch,\mu}} l_{ch,\mu}\, t_\mu\, h_{RVE} \tag{3.29}$$

where $V_{RVE,D}$is the damaged domain of the RVE, h_{RVE} is the length of the RVE *in the direction of the crack*, and t_μ is the thickness of the RVE. We can now "smear" the dissipated energy over the whole RVE domain, defining an equivalent specific fracture energy $\widetilde{g}_f$ as:

$$\widetilde{g}_f = \frac{W_{RVE,D}}{V_{RVE}} = \frac{W_{RVE,D}}{l_{ch,RVE}\, h_{RVE}\, t_\mu} = \frac{G_f}{\widetilde{l}_{ch,\mu}} \frac{l_{ch,\mu}}{l_{ch,RVE}} \tag{3.30}$$

Integrating this specific fracture energy over the dissipating domain at the macro-scale we get the total energy W_m dissipated at the macro-scale:

$$W_m = \int_{A_m} \widetilde{g}_f \, \mathrm{d}V_m \tag{3.31}$$

$$W_m = \widetilde{g}_f \, l_{ch,m}\, h_m\, t_m \tag{3.32}$$

Where h_m and t_m are respectively the length and the thickness of the crack at the macro-scale. Substituting Eq. (3.30) in Eq. (3.32), and equating it with the actual dissipated energy that we're seeking at the structural level

$$W = G_f \, h_m \, t_m \tag{3.33}$$

we obtain a definition for the modified characteristic length, *to be used at the micro-scale*, that provides the proper dissipation at the macro-scale:

$$W_m = \frac{G_f}{\widetilde{l}_{ch,\mu}} \frac{l_{ch,\mu}}{l_{ch,RVE}} \, l_{ch,m} \, h_m \, t_m = G_f \, h_m \, t_m \tag{3.34}$$

$$\widetilde{l}_{ch,\mu} = l_{ch,\mu} \frac{l_{ch,m}}{l_{ch,RVE}} \tag{3.35}$$

From Eq. (3.35) it can be seen that the characteristic lengths at the micro-scale should be multiplied by a scaling factor (constant over the RVE) which is the ratio between the characteristic length of the parent-element at the macro-scale and the characteristic length of the RVE itself.

This procedure can be regarded as a 2-step smearing of a discontinuity: (i) First, the discontinuity is smeared over the localization band in the RVE (Eq. (3.29)) , with a width of $l_{ch,\mu}$, and a length of h_{RVE}; (ii) Then, the discontinuity (now in the form of a localization band in the RVE) is smeared over the localizing element at the structural-level (Eq. (3.30), Eq. (3.31), Eq. (3.32)).

In Badillo (2012), the modified characteristic length to be used at the micro-scale was taken equal to the characteristic length of the macro-scale FE. In that context, however, the author was dealing with composites made of damageable matrix and long fibers. Long fibers are typically oriented along the loading direction, allowing damage to spread over a wide area. In those cases damage is distributed over the whole RVE domain, while the localization may happen at the structural level. On the contrary, in masonry the localization is already visible in the RVE, thus requiring to consider both length scales during the regularization procedure. It should be noted however, that the method proposed in Badillo (2012) is recovered from Eq. (3.35), setting $l_{ch,\mu} = l_{ch,RVE}$.

In Massart (2003) the localized RVE was homogenized towards a discontinuity with a band width equal to the RVE characteristic length. In the approach proposed by this work, this corresponds to $l_{ch,m} = l_{ch,RVE}$, thus leaving the characteristic length of the

micro-structural elements unchanged.
Eq. (3.29) defines the total energy dissipated in the damaged part of the RVE, assuming that the total length of the crack is equal to the length of the RVE in the crack direction (h_{RVE}), thus assuming a straight crack. Let's assume instead that in the RVE the crack is non-straight, with a total length equal to Φh_{RVE}, where $\Phi \geq 1$ is a scaling factor that measures the tortuosity of the crack. Eq. (3.29) then becomes

$$W_{RVE_{,D}} = \frac{G_f}{\widetilde{l}_{ch,\mu}} l_{ch,\mu}\, t_\mu\, \Phi h_{RVE} \tag{3.36}$$

Eq. (3.33), refers to the total energy dissipated by the real crack that we should simulate, and it was assumed straight (as for the crack in the RVE) with a length equal to the length of the specimen in the crack direction h_m. If we consider instead a non-straight crack, Eq. (3.33) becomes

$$W = G_f \Phi h_m\, t_m \tag{3.37}$$

Thus Eq. (3.34) becomes

$$W_m = \frac{G_f}{\widetilde{l}_{ch,\mu}} \frac{l_{ch,\mu}}{l_{ch,RVE}} \Phi l_{ch,m}\, h_m\, t_m = G_f\, \Phi h_m\, t_m \tag{3.38}$$

where the tortuosity factor Φ appears in both sides of the equation, thus it cancels out, and the modified characteristic length defined in Eq. (3.35) remains unchanged.

3.7 Mode I fracture test

The test reported in this section is meant to assess the regularization capabilities of the proposed method with respect to a simple mode I fracture test. The specimen is a rectangular plate in a state of plane-stress subject to a uniaxial tensile load. The micro-structure is assumed as a matrix with a periodic pattern of circular voids (note that voids are emulated with a very soft linear elastic material as reported in Table 3.1). The regularization with respect to the macro-scale FE size and the size of the RVE is checked by performing the same analysis on two different macro-scale discretizations and two different RVE sample sizes, for a total of four analyses. The same analyses are conducted with and without the regularization procedure to better show the differences. Details about the geometry, the two macro-scale models, and the two RVEs, are given

respectively in [Figure 3.4, Figure 3.5, Figure 3.6], while details about the mechanical properties of the micro-structural constituents are given in Table 3.1. Periodic boundary displacement fluctuations are employed in the multiscale analysis, since in this example we expect cracks aligned with the periodicity directions.

A local continuum damage model is used to describe the constitutive behavior of the matrix in the RVE. The main concepts of the model are summarized here. For further details the reader can refer to Cervera and Chiumenti (2006), Cervera et al. (2010b) and the references therein. The constitutive equation is defined as

$$\boldsymbol{\sigma} = (1-d)\bar{\boldsymbol{\sigma}} = (1-d)\boldsymbol{C} : \boldsymbol{\varepsilon} \tag{3.39}$$

where the stress tensor $\boldsymbol{\sigma}$ is obtained as a function of the effective stress tensor $\bar{\boldsymbol{\sigma}}$, computed from the total strain tensor $\boldsymbol{\varepsilon}$ and the fourth order isotropic linear elastic constitutive tensor $\boldsymbol{C}$, and the damage index d, which ranges from zero for the undamaged material, to one for the completely damaged material. In order to compute this damage index, related to the current effective stress state, it is necessary to introduce a scalar measure, termed as equivalent stress τ. In this example we assume a Rankine criterion, so the equivalent stress can be computed as follows:

$$\tau = \left[\bar{\boldsymbol{\sigma}}^{+} : \boldsymbol{\Lambda} : \bar{\boldsymbol{\sigma}}^{+}\right]^{1/2} \tag{3.40}$$

where $\bar{\boldsymbol{\sigma}}^{+}$ is the positive part of the effective stress tensor, defined as

$$\bar{\boldsymbol{\sigma}}^{+} = \sum_{i=1}^{3} \langle \bar{\sigma}_i \rangle \, \boldsymbol{p}_i \otimes \boldsymbol{p}_i \tag{3.41}$$

where $\boldsymbol{p_i}$ is the eigenvector associated with the principal stress $\bar{\sigma}_i$, symbols $\langle \bullet \rangle$ are the Macaulay brackets ($\langle x \rangle = x$, if $x \geq 0$, $\langle x \rangle = 0$, if $x < 0$), and $\boldsymbol{\Lambda}$ is a non-dimensional fourth order tensor defined as

$$\boldsymbol{\Lambda} = \boldsymbol{p}_1 \otimes \boldsymbol{p}_1 \otimes \boldsymbol{p}_1 \otimes \boldsymbol{p}_1 \tag{3.42}$$

Being the damage an irreversible process, we can introduce another scalar quantity, termed as damage threshold r, that represents the largest value ever reached by the equivalent stress τ during the loading history. The damage threshold r at time $t + \Delta t$ can be evaluated as

$$r = max\left(r_0,\, max\left(r_t, \tau\right)\right) \tag{3.43}$$

where r_t is the damage threshold at the previous (converged) time step, and r_0 is the initial damage threshold (the one that defines the elastic limit) that in this case is $r_0 = f_t$. Accordingly, the following damage criterion is introduced:

$$\Phi\left(\tau,\, r\right) = \tau - r_t \leq 0 \tag{3.44}$$

In this way, the damage index d, in the time interval $[t, t + \Delta t]$, can grow only if $\tau > r_t$. In this test the damage is assumed to evolve according to the following exponential law:

$$d\left(r\right) = 1 - \frac{r_0}{r} exp\left\{2H_{dis}\left(\frac{r_0 - r}{r_0}\right)\right\} \tag{3.45}$$

where H_{dis} is the discrete softening parameter. As described in Section 3.6, in the discrete problem the softening law should be adjusted according to the size of the dissipative zone (l_{dis}), in such a way that the following equation holds:

$$g_f\, l_{dis} = G_f \tag{3.46}$$

where the specific dissipated energy g_f, for the exponential softening law, can be calculated as:

$$g_f = \left(1 + \frac{1}{H_{dis}}\right)\frac{f_t^2}{2E} \tag{3.47}$$

The discrete softening parameter is calculated as

$$H_{dis} = \frac{l_{dis}}{l_{mat} - l_{dis}} \tag{3.48}$$

where $l_{mat} = 2EG_f/f_t^2$. In standard 1-scale FE analysis, l_{dis} is assumed equal to the characteristic length of the FE ($l_{dis} = l_{ch}$). Here we are using this constitutive law in the RVE of a 2-scale FE analysis, so l_{dis} is equal to the modified characteristic length $\widetilde{l}_{ch,\mu}$, as defined in Eq. (3.35).

The analysis was performed using Kratos Multiphysics Dadvand et al. (2010), a free open-source framework for the development of multidisciplinary solvers, developed at CIMNE, while pre and post-processing were done in GiD Melendo et al. (2015), also

developed at CIMNE.

The results obtained without the proposed regularization procedure (Figure 3.7a) show four widely distinct force-displacement curves. As expected, the response is more brittle for larger RVEs and/or with finer meshes at the macro-scale. Applying the proposed regularization all the analyses give the same response (Figure 3.7b), thus showing objectivity with respect to the macro-scale FE size and to the RVE size. The macro-scale displacement field and the micro-scale maximum principal strain, at the end of the analysis, are shown in Figure 3.8.

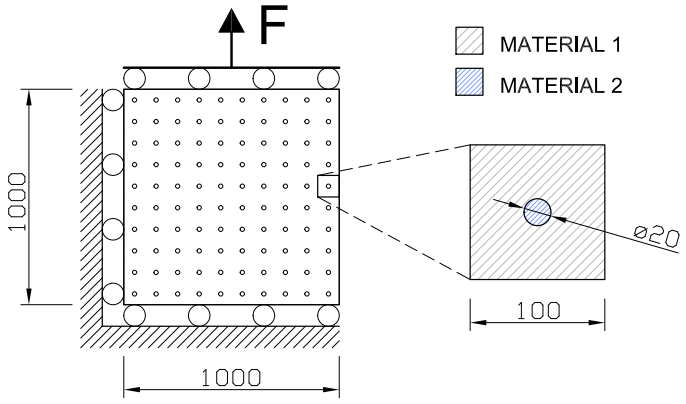

Figure 3.4: geometry of the model and boundary conditions

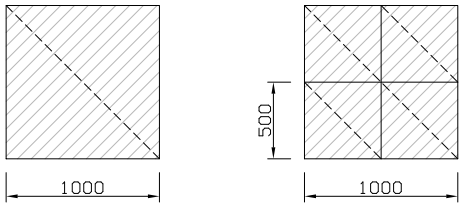

(a) (b)

Figure 3.5: macro-scale meshes: (a) macro 1x1 - mesh size=1000;(b) macro 2x2 - mesh size=500

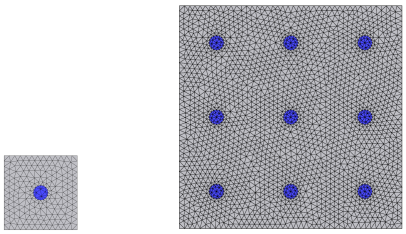

(a) (b)

Figure 3.6: (a)RVE 1x1- size=100; (b)RVE 3x3 - size=300

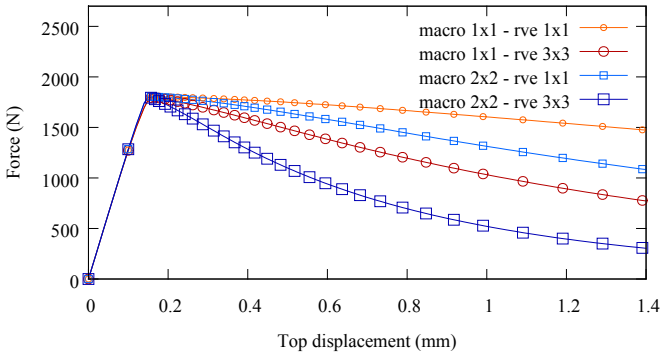

(a)

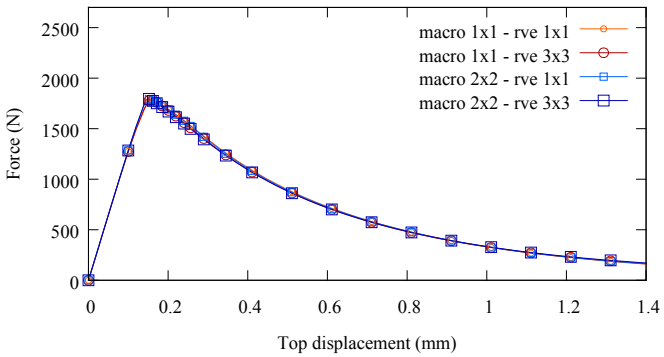

(b)

Figure 3.7: Force-Displacement curves: (a) without regularization; (b) with regularization

Property	Value (Material 1)	Value (Material 2)	Unit
Young's modulus	14000.0	1.0	N/mm^2
Poisson's ratio	0.15	0.15	-
Type	Continuum damage model	Linear elastic	-
Tensile maximum stress	2.2	-	N/mm^2
Tensile fracture energy	0.8	-	N/mm
Damage criterion	Rankine	-	-
Softening law	Exponential	-	-

Table 3.1: material properties

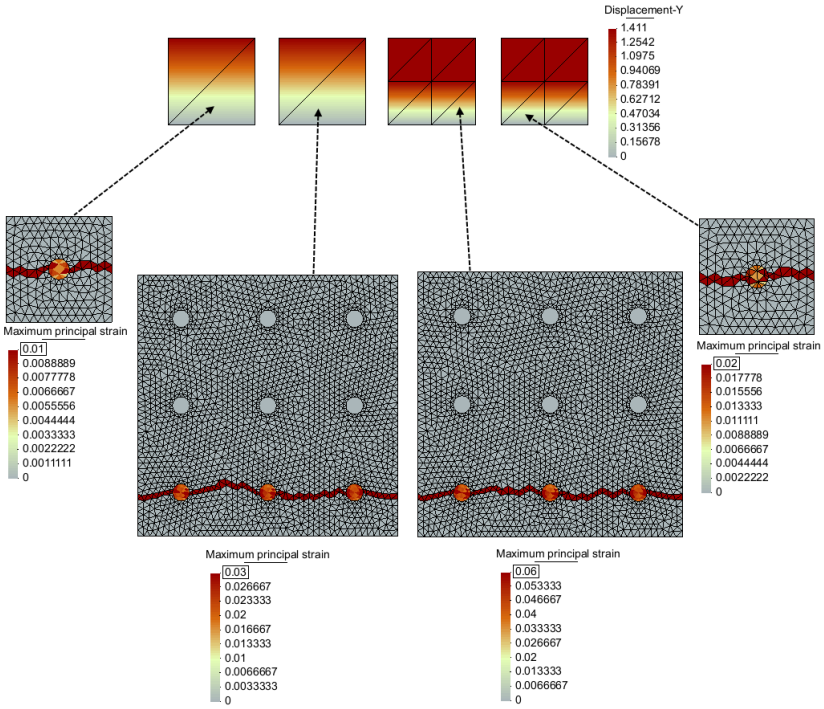

Figure 3.8: macro-scale displacement field - RVEs maximum principal strain field (with regularization)

This page is intentionally left blank

Chapter 4

Multiscale analysis of in-plane loaded shear walls

This chapter applies the concepts of the regularized first order computational homogenization method proposed in Chapter 3, to the numerical simulation of in-plane loaded shear walls made of periodic brick masonry. The results obtained with the multiscale analyses are compared to the experimental results and the micro-model results presented in Chapter 2. These examples aim at assessing the properties of the proposed approach under 2D-plane stress assumptions. The analyses were performed using Kratos Multiphysics Dadvand et al. (2010, 2013), a free open-source framework for the development of multidisciplinary solvers, developed at CIMNE, while pre and post-processing were done in GiD Melendo et al. (2015), also developed at CIMNE.

4.1 Numerical simulation of experimental test: TU Eindhoven shear wall

The geometry of the wall (here denoted as W1) as well as the boundary conditions are already described in Chapter 2. For the sake of clarity a brief description is also reported here (see Figure 4.1). The wall has no opening and it is made of one layer of solid bricks with dimensions $210\,mm \times 52\,mm \times 100\,mm$, with $10\,mm$ thick mortar joints Raijmakers and Vermeltfoort (1992). The wall is subjected to two load stages: (i) First, a uniform pressure is applied on the top of the wall, (ii) then a horizontal load is applied

under displacement control in a confined way, keeping the top of the wall horizontal and precluding vertical displacements. The multiscale analyses were performed only for the lowest vertical compression level ($0.30\,N/mm^2$).

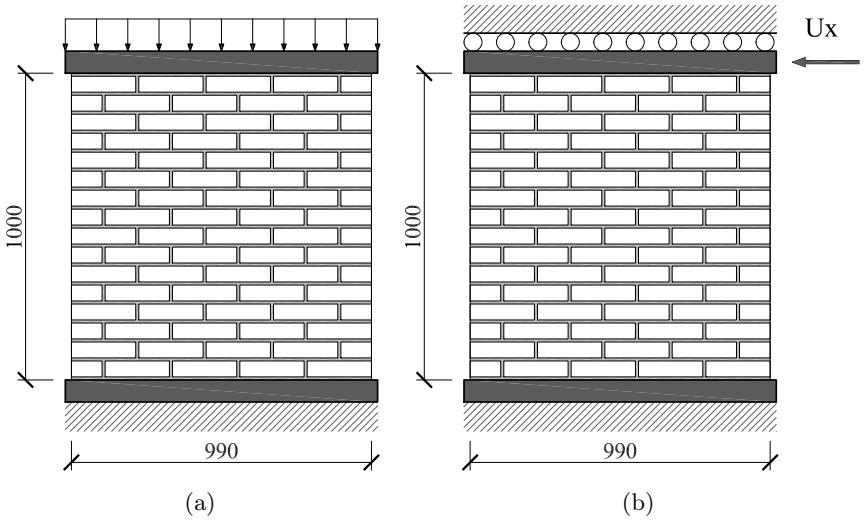

Figure 4.1: Wall W1 - TU Eindhoven shear wall Raijmakers and Vermeltfoort (1992). Geometry and loading stages: (a) stage 1: uniform vertical load $p = 0.3\,N/mm^2$; (b) stage 2: horizontal displacement under vertical confinement.

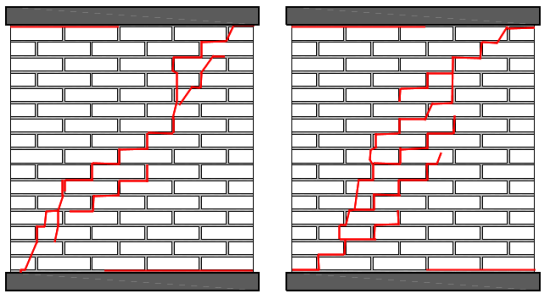

(a) $p = 0.3\,N/mm^2$ (b) $p = 0.3\,N/mm^2$

Figure 4.2: Experimental failure patterns

4.2 RVE and micro-scale constitutive laws

The mesh for both bricks and mortar joints consists of a structured grid of standard displacement-based 4-node quadrilateral plane stress elements, with a uniform size of $10.0\,mm$, as shown in Figure 4.3.

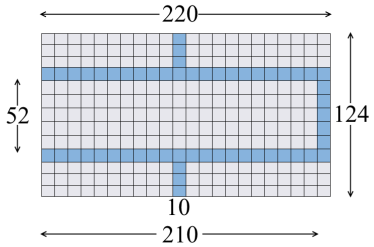

Figure 4.3: RVE mesh. All units are in mm

The constitutive model used for both bricks and mortar joints is the same used for the DNS (micro-modeling) described in Section 2.2.
Material properties for bricks and mortar joints are summarized in Table 4.1. These values are taken from the analysis conducted in Lourenço (1996), Lourenço and Rots (1997). The material parameters governing the compressive behavior of mortar joints are adapted to obtain the correct compressive behavior of the masonry composite material. In fact in this simulation a plane stress behavior is adopted, which cannot capture the typical increase in compressive capacity of mortar joints, due to the confining effect of the surrounding bricks. Another possibility of cope with this issue could be the Generalized Plane State model Addessi and Sacco (2014).

E	ν	σ_t	G_t	σ_0	σ_p	σ_r	G_c	ε_p	k_b	k_1
850.0	0.15	0.2	0.016	3.0	10.0	2.0	80.0	0.04	1.2	0.16
$\frac{N}{mm^2}$	-	$\frac{N}{mm^2}$	$\frac{N}{mm}$	$\frac{N}{mm^2}$	$\frac{N}{mm^2}$	$\frac{N}{mm^2}$	$\frac{N}{mm}$	-	-	-

(a)

E	ν	σ_t	G_t	σ_0	σ_p	σ_r	G_c	ε_p	k_b	k_1
16700.0	0.15	2.0	0.08	8.0	12.0	1.0	6.0	0.004	1.2	0.0
$\frac{N}{mm^2}$	-	$\frac{N}{mm^2}$	$\frac{N}{mm}$	$\frac{N}{mm^2}$	$\frac{N}{mm^2}$	$\frac{N}{mm^2}$	$\frac{N}{mm}$	-	-	-

(b)

Table 4.1: Material properties for bricks and mortar joints

4.3 RVE boundary conditions

The walls considered in this section are made of running bond masonry, thus showing a periodic texture. Taking advantage of the periodicity of the micro-structure, periodic boundary displacement fluctuations (see Eq. (3.11)) are enforced on the boundaries of the RVE. In some applications, the assumption of periodic boundary fluctuations might enforce unphysical constraints on the crack direction Coenen et al. (2012). However, for the specific case of masonry the cracks mainly take place following the periodic geometry of the weak mortar joints. In this sense, the periodic assumption does not spoil the actual cracking direction, both in the case of failure of bed/head joints and in the case of staircase cracks. Further detailed studies on the effect of different RVE boundary conditions, with a special focus on strain localization, are discussed in Appendix C.

4.4 Multiscale simulation

In order to assess the proposed method, the multiscale homogenization analysis was performed on four different meshes, here denoted as mesh 7x7, mesh 8x8, mesh 9x9, and mesh 15x15, as shown in Figure 4.4. All macro-scale models consists of a structured mesh of 4-node quadrilateral plane-stress finite elements. In order to improve the performance

of these rather coarse discretizations, the Enhanced Assumed Strain (EAS) quadrilateral element proposed in Simo and Rifai (1990) was used.

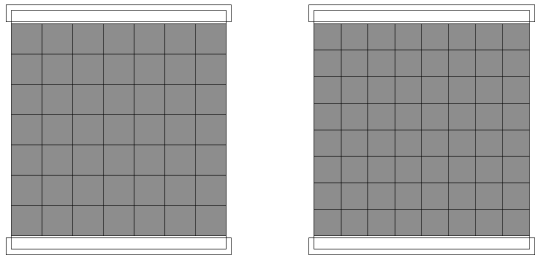

(a) mesh 7x7 (b) mesh 8x8

(c) mesh 9x9 (d) mesh 15x15

Figure 4.4: adopted meshes at the macro-scale

The results obtained from all four analyses are in very good agreement with the DNS predictions. Figure 4.5 shows how the obtained load-displacement curves closely follow the curve of the DNS. Furthermore it can be seen how upon mesh refinement the relative error among the curves diminishes, thus showing objectivity of the response thanks to the regularization procedure proposed by this research. The coarsest mesh (7x7) shows a premature failure in the compressed corners probably due to the sudden loss of bearing capacity of the few elements involved in the nonlinear process. However, already the 8x8 mesh shows a better agreement in the final stage, and finally the 9x9 and 15x15 meshes start showing smoother transitions towards the compressive failure.

The 15x15 mesh from a practical point of view may not seem the best choice for the analyzed problem, since the FE size at the macro-level is smaller than the RVE size. However, the 15x15 case was intentionally addressed to show the mesh insensitivity of

the proposed regularization method. All the other cases with coarser meshes actually look more appropriate, since the FE size at the macro-level is larger than the RVE size. In those cases, the main failure mechanisms, displacement and force capacities are correctly represented despite the mesh coarseness.

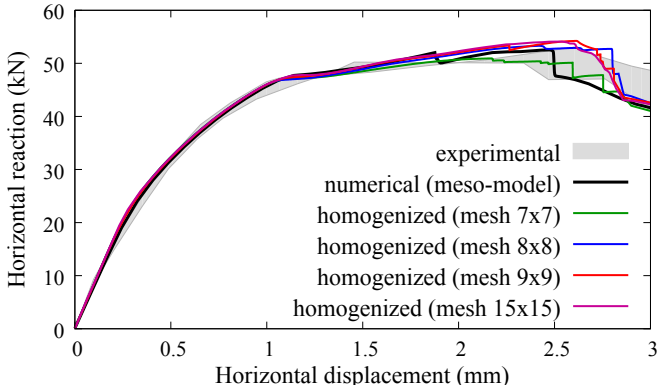

Figure 4.5: Load-Displacement curve

Table 4.3 shows the obtained results in terms of displacement, maximum principal strain and minimum principal stress. In particular, it can be seen how the shape of the crack (in terms of maximum principal strains) and the redistribution of compressive stresses closely resembles those obtained with the DNS.
Table 4.2 shows the final state (in terms of maximum principal strain, tensile and compressive damage) of three significant RVEs. The first RVE (RVE 1) shows a prevailing mode I failure, where the tensile damage concentrates in one of the bed joints. This is the first source of non-linearity that appears during the test, while the vertical confinement is still low. The second RVE (RVE 2) shows the typical staircase failure due to shear with low confining pressure. This RVE is taken from the center of the wall, where the main diagonal crack starts. Finally the third RVE (RVE 3) is taken from the bottom-left corner of the wall, where the main diagonal crack ultimately triggers the collapse of the wall. This failure happens at a later stage of the test, and due to the fact that vertical displacements on top of the wall are constrained, this area is subjected to significant concentration of compressive stresses. The RVE successfully shows a first staircase damage pattern, followed by the failure of the brick by vertical splitting.

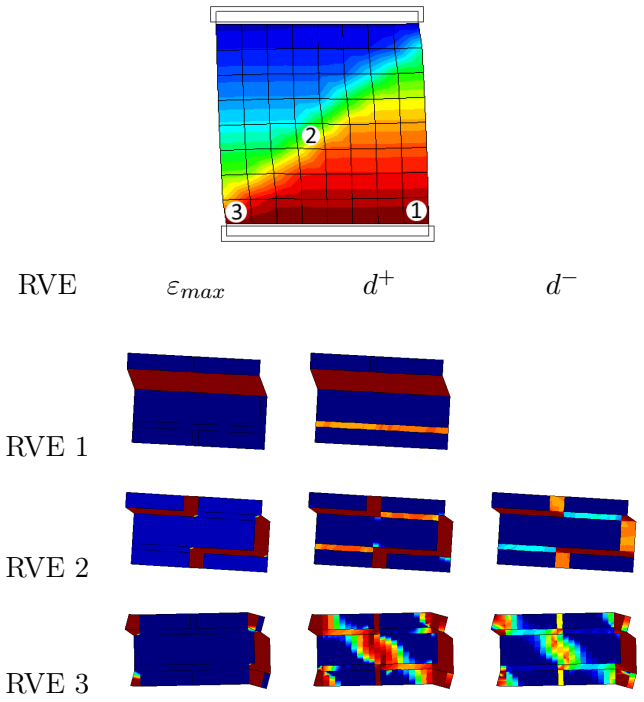

Table 4.2: final state in three significant RVEs

The smeared crack approach adopted in this research, together with proper fracture energy regularization, has provided numerical results in good agreement with the experimental cracking patterns on masonry shear walls.
However, it must be noted that in general the proposed regularization cannot solve (and neither attempts to) the well-known problem of mesh-bias dependency of the FE solution, that is, some preferred directions might still exist in the model depending on the orientation of the mesh. Such issue can be however addressed by carefully choosing the finite element model employed in the coarse mesh, as demonstrated by recent works Cervera et al. (2010a), Cervera and Chiumenti (2006), Cervera et al. (2010b), Benedetti et al. (2015), Oliver et al. (2014c). In particular the element formulation employed in current work (EAS Simo and Rifai (1990)) makes it reasonably insensitive to mesh bias (see Appendix A).

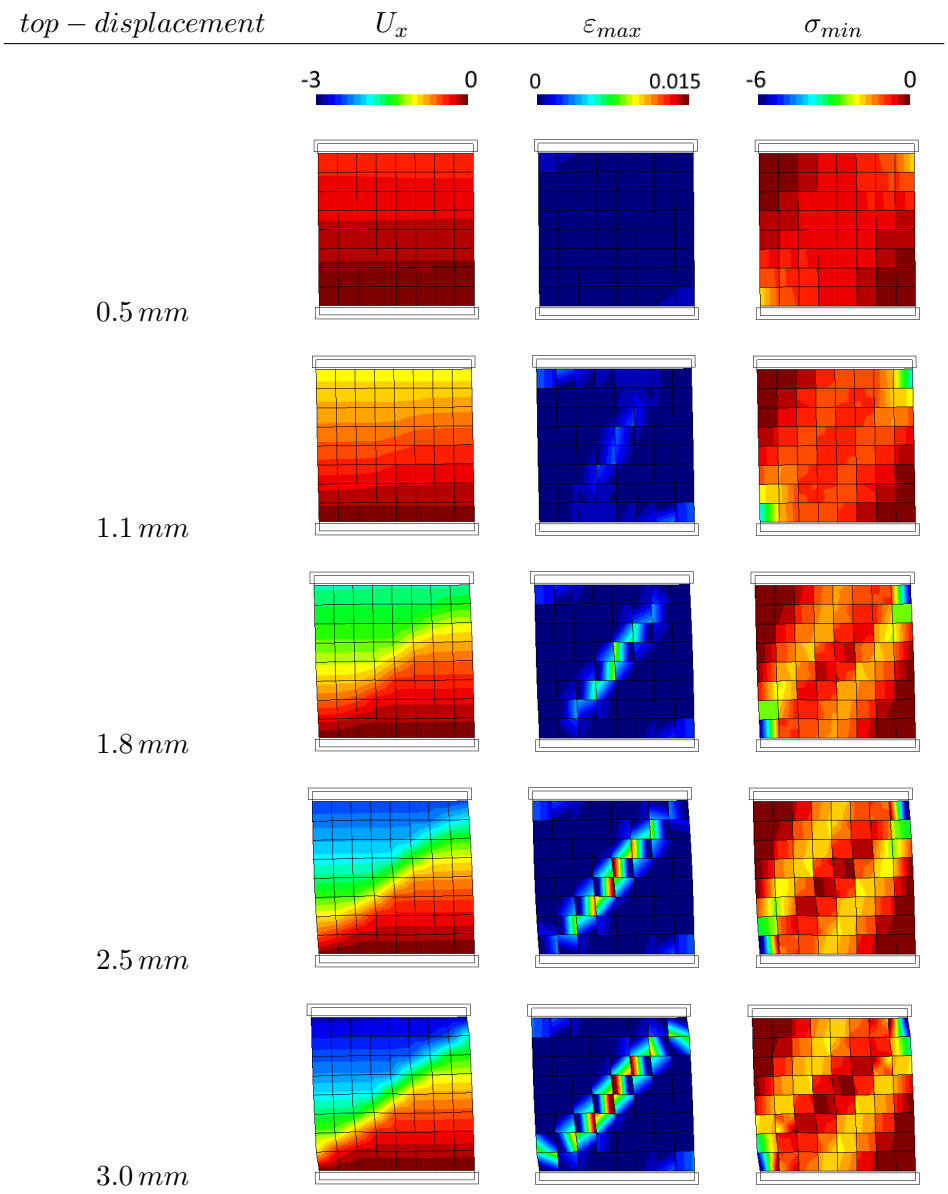

Table 4.3: CHM. Incremental contour plots of (U_x) horizontal top displacement, (ε_{max}) maximum principal strain, and (σ_{min}) minimum principal stress

4.5 Computational cost

An important aspect in this kind of simulations is the computational cost. Even if such a study is out of the scope of this paper, this section gives just a brief comparison between the DNS and the Multiscale simulations. It should be noted that the specimen described in Section 2.5.1 is quite small ($1\,m \times 1\,m$) and it is not the perfect candidate for a multiscale simulation. Nevertheless it was analyzed for a comparison with experimental results. To exploit the advantages of the proposed multiscale model, a second DNS was conducted on a larger model ($3\,m \times 3\,m$) which is a scaled version of the original one. For both cases a multiscale simulation was carried out, using the same macro-scale discretization (7 x 7 mesh) which proved to be sufficient to obtain good results in both analysis (see Figure 4.6a and Figure 4.6b).

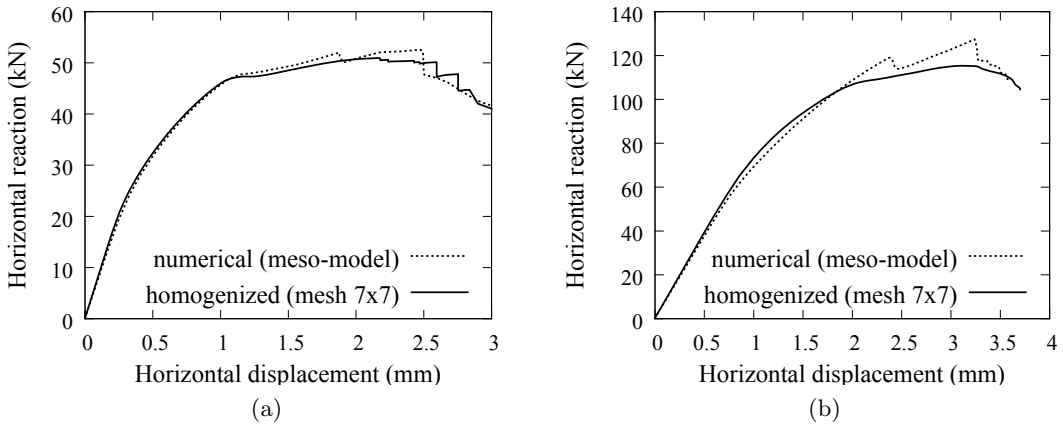

Figure 4.6: load-displacement curves for the original (a) and scaled model (b)

Table 4.4a and Table 4.4b show the computational cost of the DNS and the Multiscale simulations in terms of memory usage and (real) time. To give an objective comparison, the measured time is not referred to the entire simulation, but to the average duration of a single global iteration (i.e. the total duration of a load step, divided by the number of equilibrium iterations). Furthermore the time has been measured during specific load steps where almost the entire model is in a nonlinear range.

DNS model	number of nodes	number of elements	average time per iteration	memory
$1\,m \times 1\,m$	11152	10934	$1.51\,sec.$	$120\,MB$
$3\,m \times 3\,m$	77064	76502	$9.72\,sec.$	$730\,MB$

(a)

number of nodes	number of elements	number of RVEs	number of nodes (RVE)	number of elements (RVE)	average time per iteration	memory
64	49	196	322	356	$4.97\,sec.$	$275\,MB$

(b)

Table 4.4: computational cost for the Direct Numerical Simulations (a) and for the Multiscale simulation with a 7x7 mesh (b)

As it can be observed, the multiscale simulation proves to be efficient with respect to the DNS when dealing with large structures (or alternatively when the micro-structure is very small compared to the specimen). The DNS is penalized when used with large models due to increasing time and memory requirements, mainly required by the storage and solution of large linear systems of equations. On the contrary, the Multiscale simulation is penalized when used with small models, where the overhead of the homogenization process dominates.

All the computations were done on a single machine with an Intel Core i7-2670QM-2.20GHz CPU and 8.00 GB RAM. The code was parallelized using OpenMP.

This page is intentionally left blank

Chapter 5

Computational homogenization for thick shells

This chapter presents a multiscale method based on computational homogenization for the analysis of general heterogeneous thick shell structures, with special focus on periodic brick-masonry walls. The proposed method is designed for the analysis of shells whose micro-structure is heterogeneous in the in-plane directions, but homogeneous in the shell-thickness direction. Under this assumption, this work proposes an efficient homogenization scheme where both the macro-scale and the micro-scale are described by the same shell theory. The proposed method is then applied to the analysis of out-of-plane loaded brick-masonry walls, and compared to experimental and micro-modeling results in Chapter 6.

5.1 State of the art in computational homogenization for shells

Computational Homogenization for shell-like structures is an emerging branch of Computational Homogenization Methods. The need for such kind of homogenization stems from the fact that the size of the micro-structure has the same order of magnitude of the structure thickness, so that a standard 3D continuum homogenization cannot be applied, at least not with respect to the thickness direction. In the last years some works have been done for thin structured shells in generic structural applications, with elas-

tic or inelastic material behavior, with or without geometric non-linearity Geers et al. (2007, 2010), Coenen et al. (2010), Cong et al. (2015), Grytz and Meschke (2006). In these approaches, a 3D solid RVE discretizing the whole micro-structure in the thickness direction, is coupled to the macro-scale shell model. Applications of this concept to the specific case of masonry structures can be found in Mercatoris et al. (2009), Mercatoris and Massart (2011). In those works, material non-linearity was considered and the homogenization was based on a Kirchhoff-Love (thin) shell theory, while the nonlinear transverse shear behavior was obtained by means of a separated model (i.e. not directly from the RVE calculations).

The present work proposes a new homogenization procedure for shell-like structures, based on Reissner-Mindlin (thick) shell theory. This approach is tailored to the homogenization of micro-structures that are heterogeneous in the in-plane directions, but homogeneous in the thickness direction (i.e. an extrusion of a heterogeneous surface in the thickness direction). With this assumption, both the macro-scale domain and the RVE domain can be accurately described according to shell theories. Reissner-Mindlin shell theory is based on the hypothesis that the initially straight normals to the mid-plane of the shell remain straight after deformation, even though not necessarily perpendicular to the mid-plane. If the micro-structure is homogeneous in the thickness direction, it is reasonable to assume that the previously mentioned hypothesis holds. This assumption reduces the range of applicability of this method, with respect to those methods using a 3D RVE, but it greatly simplifies the macro-micro scale transition (both scale share the same theory), and it reduces the computational cost of the RVE calculations.

5.2 Proposed homogenization framework

This section gives the main concepts and basic equations of the proposed computational homogenization framework, where classical first order homogenization is extended to the case of shell theory. The following derivations assume small strain theory.

The main work-flow of the proposed CHM for shells can be represented as in Figure 5.1. The proposed method is formally identical to the classical CHM for 2D and 3D continua Petracca et al. (2016). The main difference is that now the continuum strain and stress tensors should be replaced with the generalized strains and generalized stresses typical of shell kinematic, as described in Section 5.3.

The procedure can be formally split into three main steps:

1. *Down-scaling* or *macro-micro transition*, where the macroscopic generalized strain at any point of the macroscopic domain, are transferred to the micro-scale, where they are used to apply boundary conditions on the RVE;

2. *Solution of the micro-scale Boundary Value Problem* (BVP), which can be done through any numerical method, but here FEM is considered;

3. *Up-scaling* or *micro-macro transition*, where the macro-scale generalized stresses and the macro-scale tangent operator are obtained via homogenization procedures.

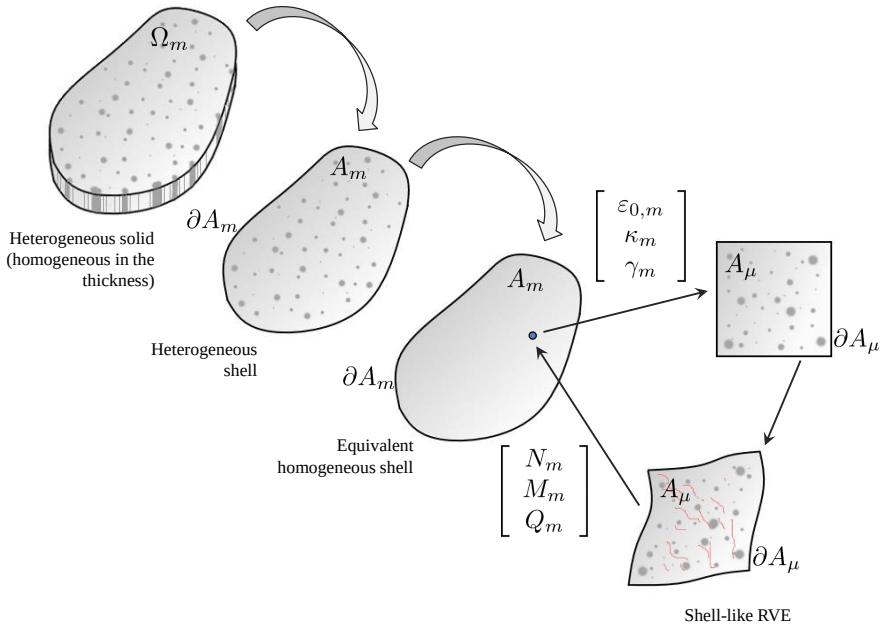

Figure 5.1: work-flow of computational homogenization for shells

5.3 Shell kinematics

From now on, any generalized quantity related to the shell theory is identified with a superimposed hat $\widehat{(\cdot)}$.
The generalized unknown vector in the local coordinate system of the shell is defined as:

$$\widehat{\boldsymbol{u}} = \left[\begin{array}{ccc} \boldsymbol{u}_0 & u_z & \boldsymbol{\theta} \end{array} \right]^T = \left[\begin{array}{ccccc} u_x & u_y & u_z & \theta_x & \theta_y \end{array} \right]^T \tag{5.1}$$

where $\boldsymbol{u}_0 = \left[\begin{array}{cc} u_x & u_y \end{array} \right]^T$ are the in-plane displacements, u_z is the vertical displacement normal to the shell mid-plane, and $\boldsymbol{\theta} = \left[\begin{array}{cc} \theta_x & \theta_y \end{array} \right]^T$ are the out-of-plane rotations about the local x and y axes respectively.
According to the first order shear deformation theory of Reissner-Mindlin, the generalized strains of the shell are defined as:

$$\widehat{\boldsymbol{\varepsilon}} = \left[\begin{array}{ccc} \boldsymbol{\varepsilon}_0 & \boldsymbol{\kappa} & \boldsymbol{\gamma}_0 \end{array} \right]^T = \left[\begin{array}{cccccccc} \varepsilon_{0,xx} & \varepsilon_{0,yy} & 2\varepsilon_{0,xy} & \kappa_{xx} & \kappa_{yy} & 2\kappa_{xy} & 2\varepsilon_{0,xz} & 2\varepsilon_{0,yz} \end{array} \right]^T \tag{5.2}$$

The in-plane strain tensor due to membrane actions is defined as:

$$\boldsymbol{\varepsilon}_0 = \nabla^s \boldsymbol{u}_0 \tag{5.3}$$

The curvature tensor due to bending actions is defined as:

$$\boldsymbol{\kappa} = \nabla^s \left(\boldsymbol{P}\boldsymbol{\theta} \right) \tag{5.4}$$

The transverse shear strain is defined as:

$$\boldsymbol{\gamma}_0 = \nabla u_z + \boldsymbol{P}\boldsymbol{\theta} \tag{5.5}$$

In the previous relations the matrix $\boldsymbol{P}$ has been introduced to take into account the sign convention about rotations (i.e. a positive curvature along the local x direction is obtained from a positive rotation about the local y direction, while a positive curvature along the local y direction is obtained from a negative rotation about the local x axis):

$$\boldsymbol{P} = \left[\begin{array}{cc} 0 & 1 \\ -1 & 0 \end{array} \right] \tag{5.6}$$

$$\boldsymbol{P}\boldsymbol{\theta} = \left[\begin{array}{c} \theta_y \\ -\theta_x \end{array} \right] \tag{5.7}$$

Therefore the generalized strains of the shell can be rewritten as:

$$\widehat{\boldsymbol{\varepsilon}} = \begin{bmatrix} \varepsilon_{0,xx} \\ \varepsilon_{0,yy} \\ 2\varepsilon_{0,xy} \\ \kappa_{xx} \\ \kappa_{yy} \\ 2\kappa_{xy} \\ 2\varepsilon_{0,xz} \\ 2\varepsilon_{0,yz} \end{bmatrix} = \begin{bmatrix} \frac{\partial u_x}{\partial x} \\ \frac{\partial u_y}{\partial y} \\ \frac{\partial u_x}{\partial y} + \frac{\partial u_y}{\partial x} \\ \frac{\partial \theta_y}{\partial x} \\ -\frac{\partial \theta_x}{\partial y} \\ \frac{\partial \theta_y}{\partial y} - \frac{\partial \theta_x}{\partial x} \\ \frac{\partial u_z}{\partial x} + \theta_y \\ \frac{\partial u_z}{\partial y} - \theta_x \end{bmatrix} \tag{5.8}$$

5.4 Shell constitutive response: through-the-thickness integrated cross section

With the shell generalized strains $\widehat{\boldsymbol{\varepsilon}}$ at hand, it is possible to calculate the constitutive response of the shell to obtain the generalized stresses:

$$\widehat{\boldsymbol{\sigma}} = \begin{bmatrix} \boldsymbol{N} & \boldsymbol{M} & \boldsymbol{Q} \end{bmatrix}^T = \begin{bmatrix} N_{xx} & N_{yy} & N_{xy} & M_{xx} & M_{yy} & M_{xy} & Q_{xz} & Q_{yz} \end{bmatrix}^T \tag{5.9}$$

where $\boldsymbol{N} = \begin{bmatrix} N_{xx} & N_{yy} & N_{xy} \end{bmatrix}^T$ is the membrane force vector per unit length, $\boldsymbol{M} = \begin{bmatrix} M_{xx} & M_{yy} & M_{xy} \end{bmatrix}^T$ is the bending/twisting moment vector per unit length, and $\boldsymbol{Q} = \begin{bmatrix} Q_{xz} & Q_{yz} \end{bmatrix}^T$ is the transverse shear force vector per unit length. A very simple and general way to obtain the shell constitutive response is by means of a through-the-thickness integration of standard continuum constitutive models.

Defining ζ as the through-the-thickness coordinate, ranging from $-H/2$ to $H/2$ (H being the thickness of the shell), the strain at each coordinate ζ can be defined as:

$$\boldsymbol{\varepsilon}_{(\zeta)} = \boldsymbol{\varepsilon}_0 + \zeta\boldsymbol{\kappa} + \boldsymbol{\gamma}_0 \tag{5.10}$$

or in matrix form:

$$\boldsymbol{\varepsilon}_{(\zeta)} = \boldsymbol{H}_{\varepsilon(\zeta)}\widehat{\boldsymbol{\varepsilon}} \tag{5.11}$$

$$\begin{bmatrix} \varepsilon_{xx} \\ \varepsilon_{yy} \\ 2\varepsilon_{xy} \\ 2\varepsilon_{xz} \\ 2\varepsilon_{yz} \end{bmatrix} = \begin{bmatrix} 1 & 0 & 0 & \zeta & 0 & 0 & 0 & 0 \\ 0 & 1 & 0 & 0 & \zeta & 0 & 0 & 0 \\ 0 & 0 & 1 & 0 & 0 & \zeta & 0 & 0 \\ 0 & 0 & 0 & 0 & 0 & 0 & 1 & 0 \\ 0 & 0 & 0 & 0 & 0 & 0 & 0 & 1 \end{bmatrix} \begin{bmatrix} \varepsilon_{0,xx} \\ \varepsilon_{0,yy} \\ 2\varepsilon_{0,xy} \\ \kappa_{xx} \\ \kappa_{yy} \\ 2\kappa_{xy} \\ 2\varepsilon_{0,xz} \\ 2\varepsilon_{0,yz} \end{bmatrix} \tag{5.12}$$

Then the stress tensor and the constitutive tangent operator at any coordinate ζ in the thickness direction can be calculated from any constitutive model:

$$\boldsymbol{\sigma}_{(\zeta)} = f\left(\boldsymbol{\varepsilon}_{(\zeta)}\right), \boldsymbol{C}_{(\zeta)} = \frac{\partial \boldsymbol{\sigma}_{(\zeta)}}{\partial \boldsymbol{\varepsilon}_{(\zeta)}} \tag{5.13}$$

The generalized stresses and the tangent constitutive matrix for the shell can be finally integrated through the thickness:

$$\widehat{\boldsymbol{\sigma}} = \int_{-\frac{H}{2}}^{\frac{H}{2}} \boldsymbol{H}_{\sigma(\zeta)}\boldsymbol{\sigma}_{(\zeta)}\,\mathrm{d}\zeta \tag{5.14}$$

$$\begin{bmatrix} N_{xx} \\ N_{yy} \\ N_{xy} \\ M_{xx} \\ M_{yy} \\ M_{xy} \\ Q_{xz} \\ Q_{yz} \end{bmatrix} = \int_{-\frac{H}{2}}^{\frac{H}{2}} \begin{bmatrix} 1 & 0 & 0 & 0 & 0 \\ 0 & 1 & 0 & 0 & 0 \\ 0 & 0 & 1 & 0 & 0 \\ \zeta & 0 & 0 & 0 & 0 \\ 0 & \zeta & 0 & 0 & 0 \\ 0 & 0 & \zeta & 0 & 0 \\ 0 & 0 & 0 & k & 0 \\ 0 & 0 & 0 & 0 & k \end{bmatrix} \begin{bmatrix} \sigma_{xx} \\ \sigma_{yy} \\ \sigma_{xy} \\ \sigma_{xz} \\ \sigma_{yz} \end{bmatrix} \mathrm{d}\zeta \tag{5.15}$$

$$\widehat{\boldsymbol{C}} = \frac{\partial \widehat{\boldsymbol{\sigma}}}{\partial \widehat{\boldsymbol{\varepsilon}}} = \int_{-\frac{H}{2}}^{\frac{H}{2}} \boldsymbol{H}_{\sigma(\zeta)}\boldsymbol{C}_{(\zeta)}\boldsymbol{H}_{\varepsilon(\zeta)}\,\mathrm{d}\zeta \tag{5.16}$$

where k is the transverse shear correction factor Cowper (1966).

It should be noted that in Eq. (5.13) the continuum stress tensor $\boldsymbol{\sigma}_{(\zeta)}$ at a certain ζ coordinate in the thickness direction, is obtained as a function of the continuum strain tensor $\boldsymbol{\varepsilon}_{(\zeta)}$ at the same ζ coordinate. However, the strain tensor $\boldsymbol{\varepsilon}_{(\zeta)}$, as defined in Eq. (5.12), is lacking the thickness strain component ε_{zz}, since the standard shell kinematics does not provide it. A simple way to cope with this issue is to obtain the plane-stress part of $\boldsymbol{\sigma}_{(\zeta)}$ ($\boldsymbol{\sigma}^{PS}_{(\zeta)}$) through any general (non-linear) plane stress constitutive law $f^{PS}(\cdot)$, while considering the transverse shear part of $\boldsymbol{\sigma}_{(\zeta)}$ ($\boldsymbol{\sigma}^{TS}_{(\zeta)}$) elastic:

$$\boldsymbol{\sigma}^{PS}_{(\zeta)} = f^{PS}\left(\boldsymbol{\varepsilon}^{PS}_{(\zeta)}\right) \tag{5.17}$$

$$\boldsymbol{\sigma}^{TS}_{(\zeta)} = G\boldsymbol{\varepsilon}^{TS}_{(\zeta)} \tag{5.18}$$

$$\sigma_{zz(\zeta)} = 0 \tag{5.19}$$

This simple approach is applicable only if the transverse shear deformation is negligible, so that one can expect a linear relation between $\boldsymbol{\sigma}^{TS}_{(\zeta)}$ and $\boldsymbol{\varepsilon}^{TS}_{(\zeta)}$. In most general cases this is not necessary true. In masonry, even if one considers a thin wall made of only one layer of bricks, the in-plane dimension of the mortar joint (of the order of $10\,mm$) will always be smaller than the out-of-plane (wall thickness) dimension (of the order of $100\,mm$). If one also considers that in many applications mortar joints are by far softer than units (bricks or stones), it is evident that all shear deformation will concentrate in mortar joints, and it will not be negligible with respect to the in-plane deformation. Thus a nonlinear response for the transverse shear is also necessary to obtain an accurate prediction of the nonlinear response under out-of-plane actions.
In the present work, based on the idea given in De Borst (1991), this goal is achieved by storing in each integration point of the shell domain, and extra internal-like variable ε_{zz} (representing the strain component in the thickness direction, which is not provided by shell kinematics). Its evolution is obtained by imposing the following constraint through a nested iterative procedure:

$$\text{find}\,\varepsilon_{zz}\,\text{such that}\int_{-\frac{H}{2}}^{\frac{H}{2}} \sigma_{zz(\zeta)}\mathrm{d}\zeta = 0 \tag{5.20}$$

5.5 Down-scaling or macro-micro transition

The macroscopic generalized strain $\widehat{\boldsymbol{\varepsilon}}_m$, in each point $\boldsymbol{x}_m$ of the macro-scale domain and at each instant t, can be obtained as the surface average of the microscopic generalized strain field $\widehat{\boldsymbol{\varepsilon}}_\mu$ defined at each point $\boldsymbol{x}_\mu$ of the micro-scale domain and at each instant t:

$$\widehat{\boldsymbol{\varepsilon}}_m(\boldsymbol{x}_m, t) = \frac{1}{A_\mu} \int_{\Omega_\mu} \widehat{\boldsymbol{\varepsilon}}_\mu(\boldsymbol{x}_\mu, t)\, \mathrm{d}A \tag{5.21}$$

where A_μ is the surface area of the shell domain at the micro-scale.
To account for the heterogeneity of the micro-structure, the microscopic displacement field $\widehat{\boldsymbol{u}}_\mu$ can be additively split into a coarse scale contribution $\widehat{\boldsymbol{u}}_m$ (arising from the macroscopic generalized strain field), and a fine scale contribution $\widehat{\tilde{\boldsymbol{u}}}_\mu$ (obtained from the solution of the micro-scale problem). Accordingly, the microscopic generalized strain field is split in the same way:

$$\widehat{\boldsymbol{\varepsilon}}_\mu(\boldsymbol{x}_\mu, t) = \widehat{\boldsymbol{\varepsilon}}_m(\boldsymbol{x}_m, t) + \widehat{\tilde{\boldsymbol{\varepsilon}}}_\mu(\boldsymbol{x}_\mu, t) \tag{5.22}$$

Inserting Eq. (5.22) into Eq. (5.21) and taking into account that $\widehat{\boldsymbol{\varepsilon}}_m$ is constant over the RVE, the minimal kinematic constraint that a microscopic generalized displacement fluctuation field should satisfy to be kinematically admissible is:

$$\int_{A_\mu} \widehat{\tilde{\boldsymbol{\varepsilon}}}_\mu\left(\boldsymbol{x}_\mu, t\right)\, \mathrm{d}A = 0 \tag{5.23}$$

In order to write this constraint as a function of the microscopic generalized displacement fluctuation field, it is useful to split Eq. (5.23) into membrane $\tilde{\boldsymbol{\varepsilon}}_{0,\mu}$, bending $\tilde{\boldsymbol{\kappa}}_\mu$, and shear $\tilde{\boldsymbol{\gamma}}_{0,\mu}$ components. For the membrane and bending components, using the Gauss theorem, the surface integrals can be rewritten as boundary integrals over the RVE boundary ∂A_μ:

$$\int_{A_\mu} \tilde{\boldsymbol{\varepsilon}}_{0,\mu}\, \mathrm{d}A = \int_{A_\mu} \nabla^s \tilde{\boldsymbol{u}}_{0,\mu}\, \mathrm{d}A = \int_{\partial A_\mu} \tilde{\boldsymbol{u}}_{0,\mu} \otimes_s \boldsymbol{n}\, \mathrm{d}S = 0 \tag{5.24}$$

$$\int_{A_\mu} \tilde{\boldsymbol{\kappa}}_\mu\, \mathrm{d}A = \int_{A_\mu} \nabla^s \left(\boldsymbol{P}\tilde{\boldsymbol{\theta}}_\mu\right)\, \mathrm{d}A = \int_{\partial A_\mu} \left(\boldsymbol{P}\tilde{\boldsymbol{\theta}}_\mu\right) \otimes_s \boldsymbol{n}\, \mathrm{d}S = 0 \tag{5.25}$$

Eq. (5.24) and Eq. (5.25) provide the minimal kinematic constraint to be applied to the micro in-plane displacement fluctuations $\tilde{\boldsymbol{u}}_{0,\mu}$ and to the micro out-of-plane rotation fluctuations $\tilde{\boldsymbol{\theta}}_\mu$.

As regarding the shear component, the following minimal constraint has to be satisfied:

$$\int_{A_\mu} \tilde{\gamma}_{0,\mu}\, \mathrm{d}A = \int_{A_\mu} \nabla \tilde{u}_{z,\mu} + \boldsymbol{P}\tilde{\boldsymbol{\theta}}_\mu\, \mathrm{d}A = 0 \tag{5.26}$$

This constraint can be either imposed directly as a surface integral, or, if periodic conditions for the vertical displacement fluctuation $\tilde{u}_z$ are to be used, only the following constraint should be applied as a surface integral over the RVE domain:

$$\int_{A_\mu} \tilde{\boldsymbol{\theta}}_\mu\, \mathrm{d}A = 0 \tag{5.27}$$

The previously defined minimal conditions can be imposed using different kinds of boundary conditions. In the present work, taking advantage of the periodic nature of the considered micro-structure, the following set of constraints have been adopted:

$$\tilde{\boldsymbol{u}}_{0,\mu}(\boldsymbol{x}_\mu^+, t) = \tilde{\boldsymbol{u}}_{0,\mu}(\boldsymbol{x}_\mu^-, t) \quad \forall\, pair\, \{\boldsymbol{x}_\mu^+,\, \boldsymbol{x}_\mu^-\} \in \partial A_\mu \tag{5.28}$$

$$\tilde{\boldsymbol{\theta}}_\mu(\boldsymbol{x}_\mu^+, t) = \tilde{\boldsymbol{\theta}}_\mu(\boldsymbol{x}_\mu^-, t) \quad \forall\, pair\, \{\boldsymbol{x}_\mu^+,\, \boldsymbol{x}_\mu^-\} \in \partial A_\mu \tag{5.29}$$

$$\tilde{u}_{z,\mu}\left(\boldsymbol{x}_\mu^+, t\right) = \tilde{u}_{z,\mu}\left(\boldsymbol{x}_\mu^-, t\right) \quad \forall\, pair\, \left\{\boldsymbol{x}_\mu^+,\, \boldsymbol{x}_\mu^-\right\} \in \partial A_\mu \tag{5.30}$$

$$\int_{A_\mu} \tilde{\boldsymbol{\theta}}_\mu\left(\boldsymbol{x}_\mu, t\right)\, \mathrm{d}A = 0 \tag{5.31}$$

Eq. (5.28), Eq. (5.29) and Eq. (5.30) impose periodicity on the microscopic fluctuation fields. This assumption showed a very good performance in a previous work by the authors on in-plane multiscale analysis of masonry Petracca et al. (2016), and further details on RVE boundary conditions, with special focus on strain localization can be found in Appendix C. Eq. (5.31) is an extra constraint arising from the definition of the transverse shear strain.

5.6 Solution of the micro-scale BVP

Assuming that inertia forces are negligible, and in absence of body forces and boundary traction, the *Principle of Virtual Work* for the 3D continuum case at the micro-scale

(RVE) reads:

$$\int_{\Omega_\mu} \boldsymbol{\sigma}_\mu \colon \delta\tilde{\boldsymbol{\varepsilon}}_\mu \, \mathrm{d}V = 0 \tag{5.32}$$

Considering that the shell works with generalized strains and stresses obtained from a through-the-thickness integration, Eq. (5.32) can be rewritten in terms of these generalized quantities:

$$\int_{A_\mu} \left\{ \int_{-\frac{H}{2}}^{\frac{H}{2}} \boldsymbol{\sigma}_\mu(\zeta) : \delta\tilde{\boldsymbol{\varepsilon}}_\mu(\zeta) \, \mathrm{d}\zeta \right\} \mathrm{d}A = 0 \tag{5.33}$$

$$\int_{A_\mu} \left\{ \int_{-\frac{H}{2}}^{\frac{H}{2}} \boldsymbol{\sigma}_\mu(\zeta) : \left(\delta\tilde{\boldsymbol{\varepsilon}}_{0,\mu} + \zeta\delta\tilde{\boldsymbol{\kappa}}_\mu + \delta\tilde{\boldsymbol{\gamma}}_{0,\mu} \right) \mathrm{d}\zeta \right\} \mathrm{d}A = 0 \tag{5.34}$$

$$\begin{aligned} \int_{A_\mu} \Bigg\{ \int_{-\frac{H}{2}}^{\frac{H}{2}} \Big[& \sigma_{\mu,xx} \left(\delta\tilde{\varepsilon}_{0,\mu,xx} + \zeta\delta\tilde{\kappa}_{\mu,xx} \right) + \sigma_{\mu,yy} \left(\delta\tilde{\varepsilon}_{0,\mu,yy} + \zeta\delta\tilde{\kappa}_{\mu,yy} \right) + \\ & \sigma_{\mu,xy} \left(2\delta\tilde{\varepsilon}_{0,\mu,xy} + 2\zeta\delta\tilde{\kappa}_{\mu,xy} \right) + \\ & \sigma_{\mu,xz} \left(2\delta\tilde{\varepsilon}_{0,\mu,xz} \right) + \sigma_{\mu,yz} \left(2\delta\tilde{\varepsilon}_{0,\mu,yz} \right) \Big] \, \mathrm{d}\zeta \Bigg\} \mathrm{d}A = 0 \end{aligned} \tag{5.35}$$

$$\int_{A_\mu} \left[\boldsymbol{N}_\mu \colon \delta\tilde{\boldsymbol{\varepsilon}}_{0,\mu} + \boldsymbol{M}_\mu \colon \delta\tilde{\boldsymbol{\kappa}}_\mu + \boldsymbol{Q}_\mu \colon \delta\tilde{\boldsymbol{\gamma}}_{0,\mu} \right] \mathrm{d}A = 0 \tag{5.36}$$

$$\int_{A_\mu} \widehat{\boldsymbol{\sigma}}_\mu \colon \delta\widehat{\tilde{\boldsymbol{\varepsilon}}}_\mu \, \mathrm{d}A = 0 \tag{5.37}$$

5.7 Up-scaling or micro-macro transition

The last step in the homogenization procedure consists in finding the homogenized macroscopic generalized stress tensor (and if required the homogenized tangent operator) after the RVE equilibrium is found. As shown in Hernández et al. (2012), Ortolano et al. (2013), a definition of the homogenized stress tensor can be derived directly from the Hill-Mandel Principle Hill (1965), Mandel (1971) using the additive split of the microscopic strain. The Hill-Mandel Principle can be written in terms of generalized stresses and strains as:

$$\widehat{\boldsymbol{\sigma}}_m : \widehat{\dot{\boldsymbol{\varepsilon}}}_m = \frac{1}{A_\mu} \int_{A_\mu} \widehat{\boldsymbol{\sigma}}_\mu : \widehat{\dot{\boldsymbol{\varepsilon}}}_\mu \, \mathrm{d}A \tag{5.38}$$

Inserting the split of the microscopic generalized strain given in Eq. (5.22), into the Hill-Mandel Principle Eq. (5.38), the following relation is obtained:

$$\widehat{\boldsymbol{\sigma}}_m : \widehat{\dot{\boldsymbol{\varepsilon}}}_m = \frac{1}{A_\mu} \int_{A_\mu} \widehat{\boldsymbol{\sigma}}_\mu : \widehat{\dot{\varepsilon}}_m \, \mathrm{d}A + \frac{1}{A_\mu} \int_{A_\mu} \widehat{\boldsymbol{\sigma}}_\mu : \widehat{\dot{\tilde{\boldsymbol{\varepsilon}}}}_\mu \, \mathrm{d}A \tag{5.39}$$

$$\widehat{\boldsymbol{\sigma}}_m : \widehat{\dot{\boldsymbol{\varepsilon}}}_m = \frac{1}{A_\mu} \int_{A_\mu} \widehat{\boldsymbol{\sigma}}_\mu : \widehat{\dot{\varepsilon}}_m \, \mathrm{d}A + \frac{1}{A_\mu} \int_{A_\mu} \widehat{\boldsymbol{\sigma}}_\mu : \boldsymbol{\mathcal{L}} \widehat{\dot{\tilde{\boldsymbol{u}}}}_\mu \, \mathrm{d}A \tag{5.40}$$

where

$$\boldsymbol{\mathcal{L}} \widehat{\dot{\tilde{\boldsymbol{u}}}}_\mu = \begin{bmatrix} \nabla^s \widehat{\dot{\tilde{\boldsymbol{u}}}}_{0,\mu} \\ \nabla^s \boldsymbol{P} \widehat{\dot{\tilde{\boldsymbol{\theta}}}}_\mu \\ \nabla \widehat{\dot{\tilde{u}}}_{z,\mu} + \boldsymbol{P} \widehat{\dot{\tilde{\boldsymbol{\theta}}}}_\mu \end{bmatrix} \tag{5.41}$$

Eq. (5.40) is valid for any kinematically admissible $\widehat{\dot{\tilde{\boldsymbol{u}}}}_\mu$. Specifically, in the case of $\widehat{\dot{\tilde{\boldsymbol{u}}}}_\mu = 0$, the following relation is obtained:

$$\widehat{\boldsymbol{\sigma}}_m : \widehat{\dot{\boldsymbol{\varepsilon}}}_m = \frac{1}{A_\mu} \int_{A_\mu} \widehat{\boldsymbol{\sigma}}_\mu : \widehat{\dot{\varepsilon}}_m \, \mathrm{d}A \quad \forall \dot{\varepsilon}_m \tag{5.42}$$

which is valid for any macroscopic strain rate field, leading to:

$$\widehat{\boldsymbol{\sigma}}_m = \frac{1}{A_\mu} \int_{A_\mu} \widehat{\boldsymbol{\sigma}}_\mu \, \mathrm{d}A \tag{5.43}$$

Thus the homogenized macroscopic generalized stress tensor can be obtained as the surface average of the microscopic generalized stress field of the RVE. From a computational point of view, it is more convenient to obtain the homogenized generalized stresses from the reactions obtained on the RVE boundaries upon equilibrium Coenen et al. (2010):

$$\boldsymbol{N} = \frac{1}{A_\mu} \sum_{i=1}^{n} \boldsymbol{f}_{r,i} \otimes^s \boldsymbol{x}_{\mu,i} \tag{5.44}$$

$$\boldsymbol{M} = \frac{1}{A_\mu}\boldsymbol{P}\sum_{i=1}^{n}\boldsymbol{m}_{r,i}\otimes^{s}\boldsymbol{x}_{\mu,i} - \frac{1}{A_\mu}\sum_{i=1}^{n}f_{rz,i}\boldsymbol{x}_{\mu,i}\otimes\boldsymbol{x}_{\mu,i} \tag{5.45}$$

$$\boldsymbol{Q} = \frac{1}{A_\mu}\sum_{i=1}^{n}f_{rz,i}\boldsymbol{x}_{\mu,i} \tag{5.46}$$

where $i = 1, 2, ..., n$ is the boundary node index, $\boldsymbol{x}_{\mu,i} = \begin{bmatrix} x_{\mu,i} & y_{\mu,i} \end{bmatrix}^T$ is the position vector of the boundary node i, $\boldsymbol{f}_{r,i} = \begin{bmatrix} f_{rx,i} & f_{ry,i} \end{bmatrix}^T$ is the in-plane reaction force vector, $\boldsymbol{m}_{r,i} = \begin{bmatrix} m_{rx,i} & m_{ry,i} \end{bmatrix}^T$ is the out-of-plane reaction moment vector, and $f_{rz,i}$ is the vertical reaction force. The permutation matrix $\boldsymbol{P}$ in Eq. (5.45), is the same introduced in Eq. (5.6). The explicit expression for each homogenized macro generalized stress component is:

$$\widehat{\boldsymbol{\sigma}}_m = \begin{bmatrix} N_{xx} \\ N_{yy} \\ N_{xy} \\ M_{xx} \\ M_{yy} \\ M_{xy} \\ Q_{xz} \\ Q_{yz} \end{bmatrix} = \frac{1}{A_\mu}\sum_{i=1}^{n}\begin{bmatrix} f_{rx,i}x_{\mu,i} \\ f_{ry,i}y_{\mu,i} \\ \frac{1}{2}\left(f_{rx,i}y_{\mu,i} + f_{ry,i}x_{\mu,i}\right) \\ m_{ry,i}x_{\mu,i} - \frac{1}{2}f_{rz,i}x_{\mu,i}^2 \\ -m_{rx,i}y_{\mu,i} - \frac{1}{2}f_{rz,i}y_{\mu,i}^2 \\ \frac{1}{2}\left(m_{ry,i}y_{\mu,i} - m_{rx,i}x_{\mu,i}\right) - \frac{1}{2}f_{rz,i}x_{\mu,i}y_{\mu,i} \\ f_{rz,i}x_{\mu,i} \\ f_{rz,i}y_{\mu,i} \end{bmatrix} \tag{5.47}$$

5.8 Typical deformation modes obtained from the shell homogenization framework

This section shows the eight deformation modes obtained from the proposed homogenization framework for thick shells in terms of coarse scale displacements/rotations, fine scale displacement/rotation fluctuations, and total displacements/rotations. In the proposed method, the unknowns at the micro-scale are the fluctuations, so the total dis-

placements/rotations are just computed and displayed as a post-process for visualization purposes.

The total microscopic displacement/rotation vector is defined as the sum of the coarse scale contribution and the fine scale contribution (fluctuations):

$$\widehat{\boldsymbol{u}}_\mu = \widehat{\boldsymbol{u}}_m + \widehat{\tilde{\boldsymbol{u}}}_\mu \tag{5.48}$$

$$\begin{bmatrix} \boldsymbol{u}_{0,\mu} & u_{z,\mu} & \boldsymbol{\theta}_\mu \end{bmatrix}^T = \begin{bmatrix} \boldsymbol{u}_{0,m} & u_{z,m} & \boldsymbol{\theta}_m \end{bmatrix}^T + \begin{bmatrix} \tilde{\boldsymbol{u}}_{0,\mu} & \tilde{u}_{z,\mu} & \tilde{\boldsymbol{\theta}}_\mu \end{bmatrix}^T \tag{5.49}$$

$$\begin{bmatrix} u_{x,\mu} & u_{y,\mu} & u_{z,\mu} & \theta_{x,\mu} & \theta_{y,\mu} \end{bmatrix}^T = \begin{bmatrix} u_{x,m} & u_{y,m} & u_{z,m} & \theta_{x,m} & \theta_{y,m} \end{bmatrix}^T + \begin{bmatrix} \tilde{u}_{x,\mu} & \tilde{u}_{y,\mu} & \tilde{u}_{z,\mu} & \tilde{\theta}_{x,\mu} & \tilde{\theta}_{y,\mu} \end{bmatrix}^T \tag{5.50}$$

The microscopic displacement/rotation fluctuations $\widehat{\tilde{\boldsymbol{u}}}_\mu$ are obtained by the solution of the microscopic boundary value problem, while the displacement/rotation vector due to the coarse scale contribution $\widehat{\boldsymbol{u}}_m$ can be calculated as a post-process from the macroscopic generalized strains $\widehat{\boldsymbol{\varepsilon}}_m$:

$$\boldsymbol{u}_{0,m} = \boldsymbol{\varepsilon}_{0,m}\boldsymbol{x}_\mu \tag{5.51}$$

$$\boldsymbol{\theta}_m = \boldsymbol{P}^T\boldsymbol{\kappa}_m\boldsymbol{x}_\mu \tag{5.52}$$

$$u_{z,m} = -\frac{1}{2}\left(\boldsymbol{\kappa}_m\boldsymbol{x}_\mu\right)\cdot\boldsymbol{x}_\mu + \boldsymbol{\gamma}_m\cdot\boldsymbol{x}_\mu \tag{5.53}$$

In Eq. (5.52), the permutation matrix $\boldsymbol{P}$ is still the one defined in Eq. (5.6) to take into account the sign convention of rotations. In Eq. (5.53), the first term represents the deflection due to the bending deformation, while the second term represents the deflection due to the shear deformation. Figure 5.2 to Figure 5.9 show all the eight deformation modes associated with the eight deformation components of the macroscopic generalized strain vector. In all of them, (a) shows the displacement/rotation field $\widehat{\boldsymbol{u}}_m$ arising from the associated average macroscopic deformation mode representing the coarse-scale contribution, (b) shows the microscopic displacement/rotation fluctuation field $\widehat{\tilde{\boldsymbol{u}}}_\mu$(unknown

of the microscopic BVP) that represents the fine-scale contribution accounting for the heterogeneity (bricks and mortar), and (c) represents the total microscopic displacement/rotation $\widehat{\boldsymbol{u}}_\mu$as the superposition of coarse and fine scale contributions. Figure 5.2, Figure 5.3 and Figure 5.4 show the three membrane deformation modes. Figure 5.5, Figure 5.6 and Figure 5.7 show the three bending deformation modes. Figure 5.8 and Figure 5.9 show the two transverse shear deformation modes.

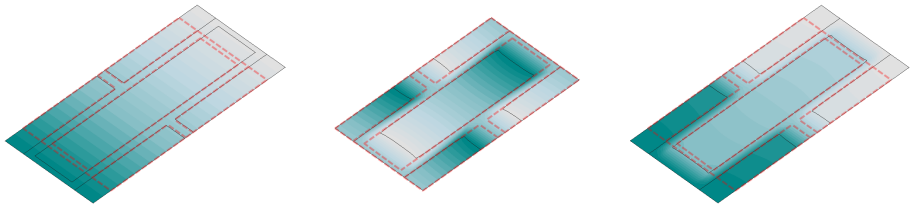

(a) (b) (c)

Figure 5.2: deformation mode due to ε_{xx}. (a) coarse scale, (b) fine scale, (c) total

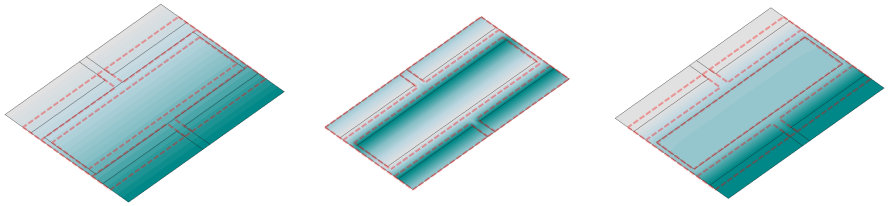

(a) (b) (c)

Figure 5.3: deformation mode due to ε_{yy}. (a) coarse scale, (b) fine scale, (c) total

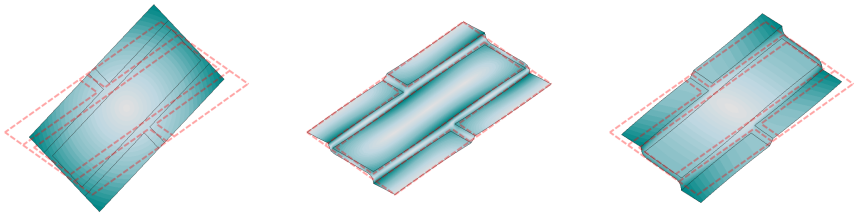

(a) (b) (c)

Figure 5.4: deformation mode due to ε_{xy}. (a) coarse scale, (b) fine scale, (c) total

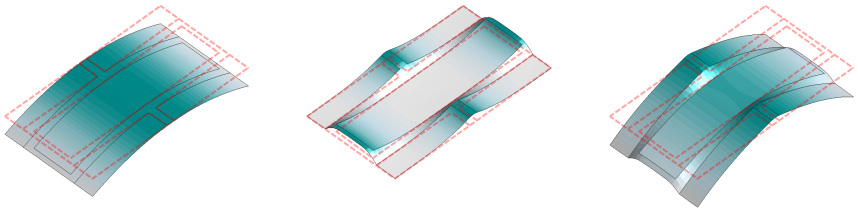

(a) (b) (c)

Figure 5.5: deformation mode due to κ_{xx}. (a) coarse scale, (b) fine scale, (c) total

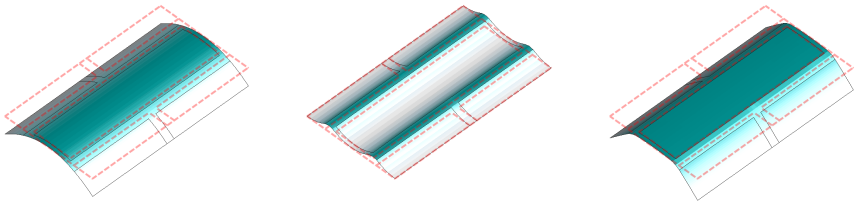

(a) (b) (c)

Figure 5.6: deformation mode due to κ_{yy}. (a) coarse scale, (b) fine scale, (c) total

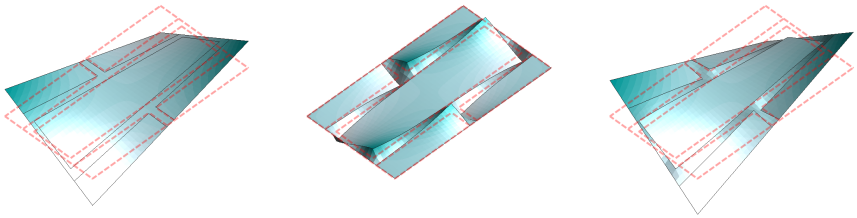

(a) (b) (c)

Figure 5.7: deformation mode due to κ_{xy}. (a) coarse scale, (b) fine scale, (c) total

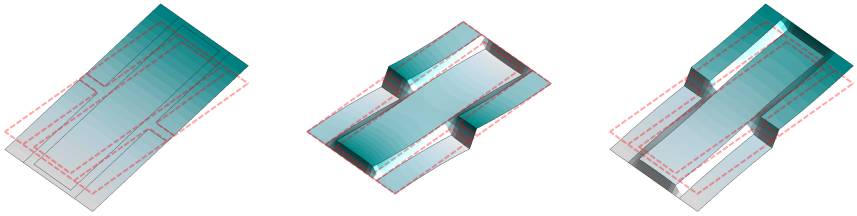

(a) (b) (c)

Figure 5.8: deformation mode due to γ_{xz}. (a) coarse scale, (b) fine scale, (c) total

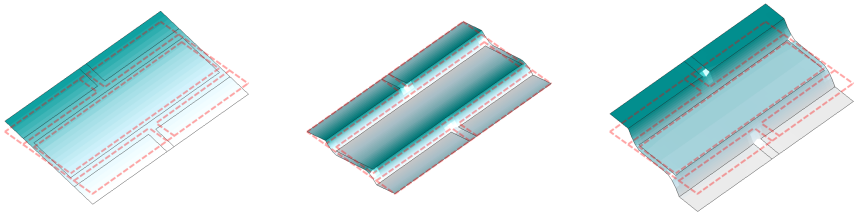

(a) (b) (c)

Figure 5.9: deformation mode due to γ_{yz}. (a) coarse scale, (b) fine scale, (c) total

This page is intentionally left blank

Chapter 6

Multiscale analysis of out-of-plane loaded masonry walls

In this chapter, the proposed method is used to simulate the out-of-plane behavior of brick-masonry walls. Experimental tests on Unreinforced Masonry Walls (URM) presented in Griffith and Vaculik (2007) are considered here for the numerical assessment of the method. First, a brief description of the selected experimental test is given in Section 6.1. The nonlinear behavior of both bricks and mortar joints is accounted for by means of a constitutive model based on Continuum-Damage Mechanics, described in Chapter 2-Section 2.2, while the adopted RVE and material parameters used for each micro-structural constituent are described in Section 6.2. Before proceeding with the Multiscale simulation, a Direct Numerical Simulation (DNS) was performed to check the capability of the constitutive model to emulate the specific local responses of the masonry wall under out-of-plane loadings, and the results are discussed in Section 6.3. Finally, the results obtained from the multiscale simulations are compared with both the experimental results and the DNS results in Section 6.4.

The analysis was performed using Kratos Multiphysics Dadvand et al. (2010, 2013), a free open-source framework for the development of multidisciplinary solvers, developed at CIMNE, while pre and post-processing were done in GiD Melendo et al. (2015), also developed at CIMNE.

6.1 Experimental test

Experimental tests on Unreinforced Masonry Walls (URM) have been presented in Griffith and Vaculik (2007). Eight full-scale clay brick URM walls were subjected to quasi-static displacement-controlled loading to investigate their load-deflection behavior beyond their point of maximum strength. Of the eight walls analyzed in the experimental campaign, only one is considered here. The wall measures $4\,m \times 2.5\,m$, with bricks of $230\,mm \times 76\,mm \times 110\,mm$, and mortar joints of $10\,mm$. After the first stage where a vertical pre-compression of $0.1\,N/mm^2$ is applied, the wall is subjected to a uniform pressure under displacement control. In order to provide a realistic full moment connection along the vertical edges, $450\,mm$ long return walls were built in as part of the tested wall. Figure 6.1 shows the wall geometry and the obtained failure pattern on the main face of the wall, and on the lateral turning walls.

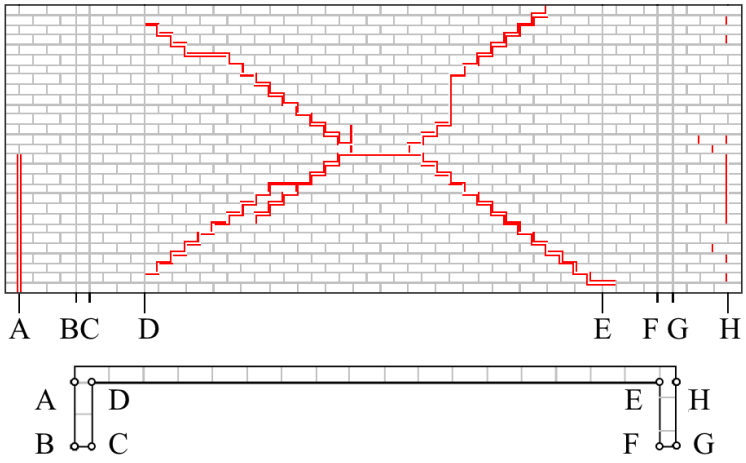

Figure 6.1: Tested wall geometry and obtained failure pattern Griffith and Vaculik (2007)

6.2 RVE and material parameters

The geometry of the adopted RVE is shown in Figure 6.2. The boundary conditions for the RVE are those listed from Eq. (5.28) to Eq. (5.31), i.e. periodicity of all displacement

and rotation fluctuations, plus the extra constraint on the volume average of rotation fluctuations arising from the definition of transverse shear deformation.

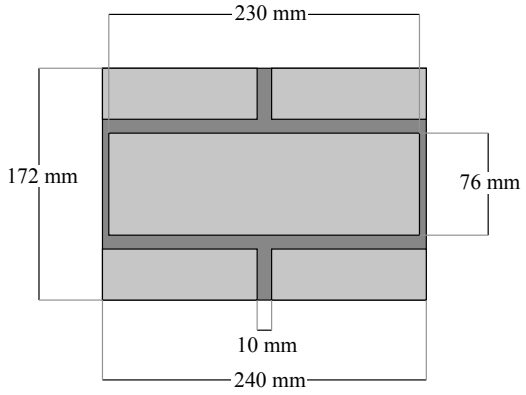

Figure 6.2: RVE geometry.

The constitutive model used for both bricks and mortar joints is based on Continuum Damage Mechanics, and it has been described in Section 2.2.
Material properties for bricks and mortar are summarized in Table 6.1. These material properties are used for both DNS and Multiscale simulations.

E	ν	σ_t	G_t	σ_0	σ_p	σ_r	G_c	ε_p	k_b	k_1	γ
52700.0	0.15	2.0	0.08	9.0	18.0	2.5	40.0	0.003	1.2	0.0	3.0
$\frac{N}{mm^2}$	-	$\frac{N}{mm^2}$	$\frac{N}{mm}$	$\frac{N}{mm^2}$	$\frac{N}{mm^2}$	$\frac{N}{mm^2}$	$\frac{N}{mm}$	-	-	-	-

(a)

E	ν	σ_t	G_t	σ_0	σ_p	σ_r	G_c	ε_p	k_b	k_1	γ
1000.0	0.15	0.15	0.003	1.0	2.5	0.5	30.0	0.02	1.2	0.16	1.0
$\frac{N}{mm^2}$	-	$\frac{N}{mm^2}$	$\frac{N}{mm}$	$\frac{N}{mm^2}$	$\frac{N}{mm^2}$	$\frac{N}{mm^2}$	$\frac{N}{mm}$	-	-	-	-

(b)

Table 6.1: Material properties for (a) bricks and (b) mortar joints

6.3 Direct numerical simulation

In the DNS the entire micro-structure is discretized in the computational model with shell elements, taking advantage of the fact that the micro-structure is heterogeneous in the in-plane direction but homogeneous in the thickness direction (1-layer of bricks). The geometry of the micro-model is shown in Figure 6.3. Due to the symmetry of both geometry and boundary conditions, only the left-half of the wall has been modeled.

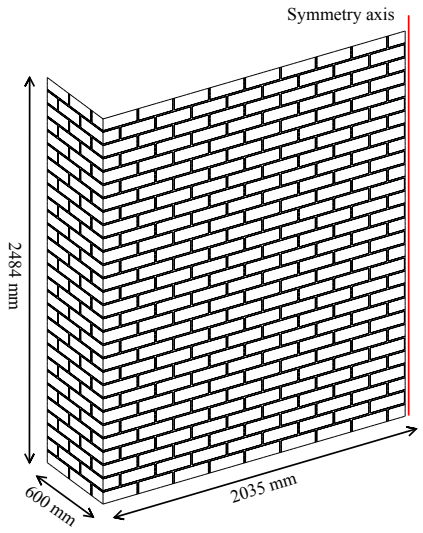

Figure 6.3: Micro-model geometry

Figure 6.4 shows the pressure-deflection curve obtained from the DNS and compared with the experimental results. The deflection is measured at the center of the wall, where the maximum value is attained. Overall the micro-model simulation shows a good agreement with the experiment. Figure 6.5 shows the deformed shape at the end of the analysis, with a good agreement in the prediction of the failure mode shown in Figure 6.1.

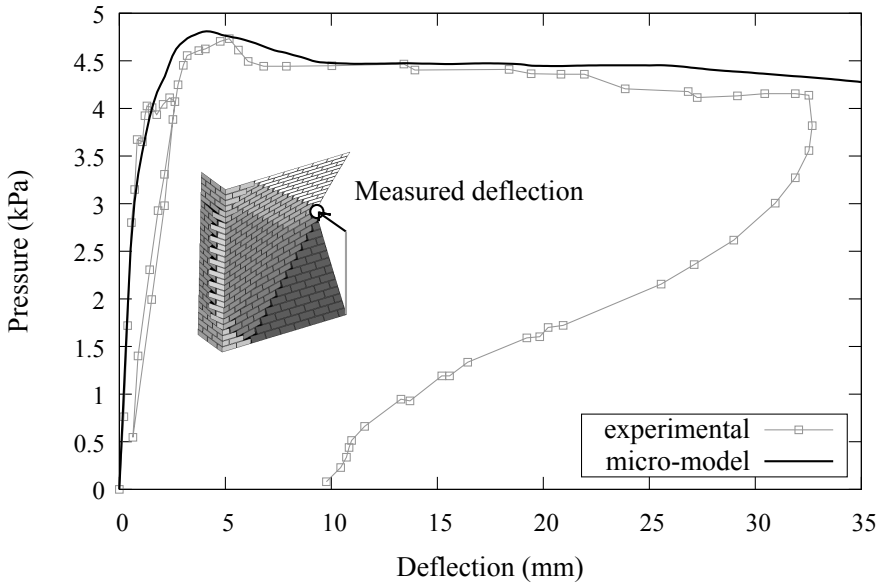

Figure 6.4: pressure-deflection curve obtained from the micro-model analysis

The most important feature shown by the experimental campaign, as reported in Griffith and Vaculik (2007), is the "apparent" plastic behavior of the tested walls: after reaching the wall strength at deflections between 2.0 and 5.0 mm, a first loss of bearing capacity is shown, soon followed by an almost constant strength plateau up to a deflection of 25.0 mm. As discussed by the authors of the experimental campaign, this apparent plastic behavior may be attributed to a redistribution of bending moment along diagonal cracks to horizontal bending along the vertical edges, where the bending restraint provided by the return walls has additional capacity to accept transfer of load from the diagonal bending mechanism. Table 6.2 shows the evolution of tensile and compressive damage during the first stages of the analysis, where the wall strength is attained, and the damage pattern at the end of the simulation.

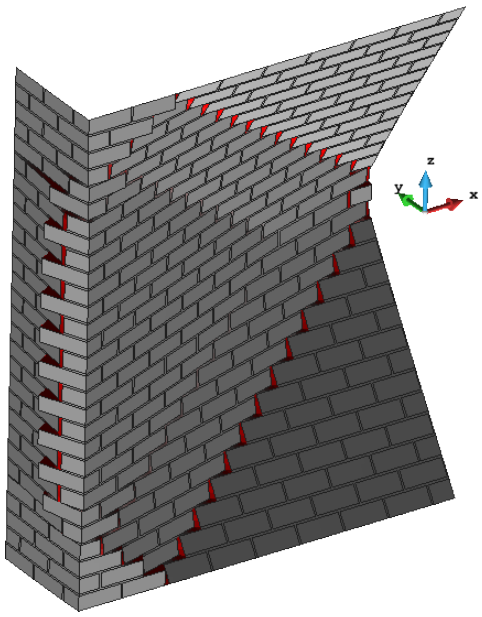

(a)

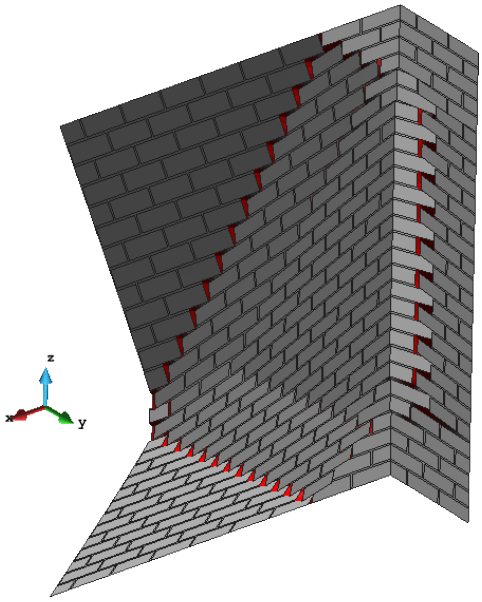

(b)

Figure 6.5: final deformed shape, (a) front and (b) back view from the micro-model analysis

Deflection $[mm]$	d^+	d^-
0.7	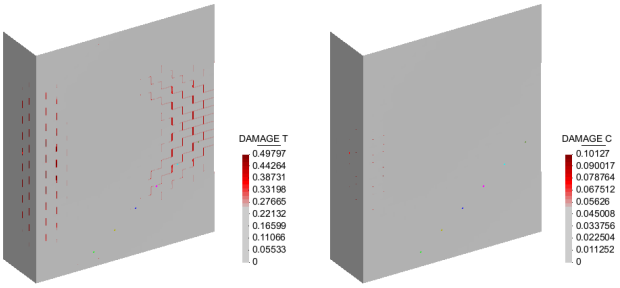	
2.9	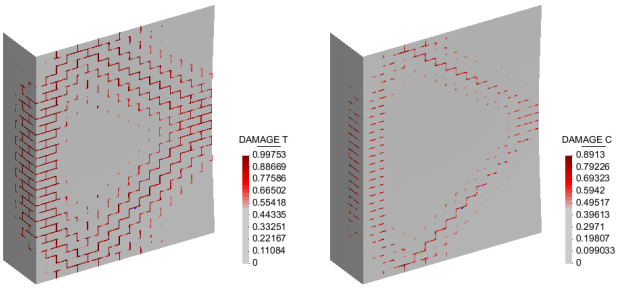	
4.0	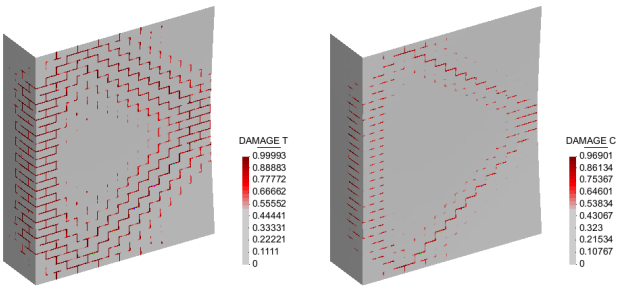	
35.0	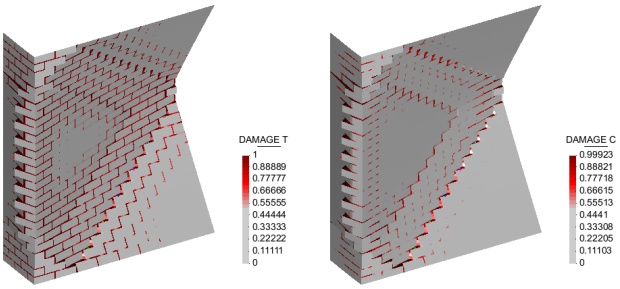	

Table 6.2: Tensile and Compressive damage evolution at different load stages from micro-model analysis

As a last note, the importance of adopting a 3D constitutive model instead of a plane-stress one, as already pointed out in Section 5.4, is clearly shown in Figure 6.6, where a detail of the bottom-left corner of the structure is given. The in-plane strain along local X-direction at the top of the shell $\varepsilon_{xx(+H/2)} = \varepsilon_{0,xx} + \kappa_{xx}\frac{H}{2} \cong 0.11 + 0.0026 \times 110/2 = 0.253$ is larger but comparable to the transverse shear strain $\varepsilon_{0,xz} = 0.157$. It is evident that the transverse shear deformation cannot be neglected. The failure mode depicted in Figure 6.6 can be considered as an overall bending state of deformation along the local X-direction, if one thinks about the overall behavior of the "composite" masonry material. However, due to the arrangement of the micro-structure, and the strong difference in mechanical properties of units and mortar, a significant amount of transverse shear appears in the (softer) mortar joints, in order to allow units to bend around the vertical axis of the wall.

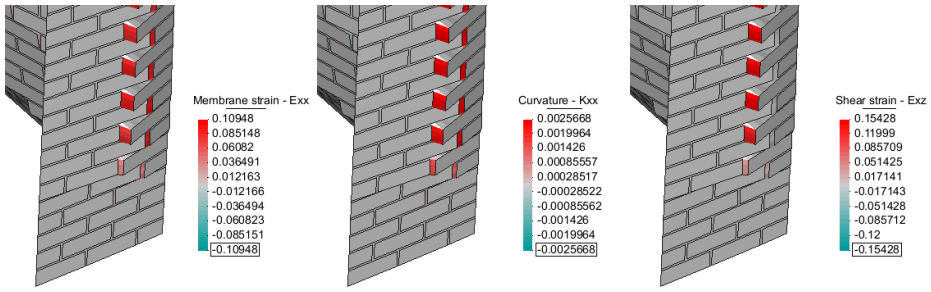

(a) $\varepsilon_{0,xx}$ (b) κ_{xx} (c) ε_{xz}

Figure 6.6: Comparison of membrane, bending and shear strains in micro-model analysis

6.4 Multiscale simulation

In this section the proposed computational homogenization framework for shells is assessed, comparing it with the results obtained by the DNS presented in Section 6.3. For the multiscale simulations three macro-scale discretizations are used, in order to check the regularization properties of the method with respect to the mesh size. It should be noted that the regularization procedure presented in Petracca et al. (2016) and briefly reported in Section 3.6 is only meant to provide objective results in terms of amount of

dissipated energy with respect to the mesh size (i.e. to alleviate the mesh-*size* dependency). For problems related to mesh bias dependency Cervera et al. (2010a), Benedetti et al. (2015), Cervera et al. (2010b), Pelà et al. (2014b), Saloustros et al. (2015a) (i.e. dependency on the mesh orientation), the adopted procedure should be accompanied with enhanced FE formulations at the macro-scale. In the present work, the used Shell FE has an enhancement in the membrane strain field following the EAS method Simo and Rifai (1990), and in the transverse shear field following the MITC plate formulation Dvorkin and Bathe (1984), Bathe and Dvorkin (2005). The adopted element seems to be sufficiently accurate with respect to mesh orientation dependency. The adopted meshes are given in Figure 6.7, with a discretization size of 300 mm, 150 mm and 75 mm respectively.

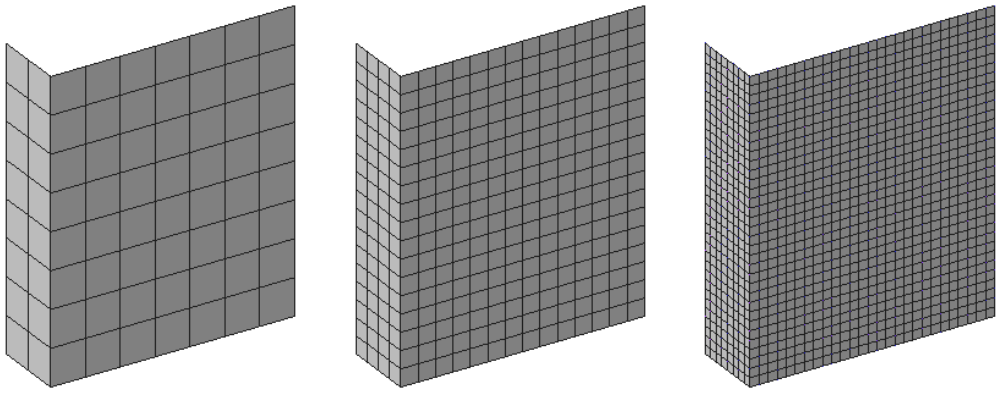

(a) $h = 300mm$ (b) $h = 150mm$ (c) $h = 75mm$

Figure 6.7: macro-scale meshes used for the multiscale simulations

Figure 6.8 shows the pressure-deflection curves obtained from the three multiscale analyses, compared to the DNS and experimental results.

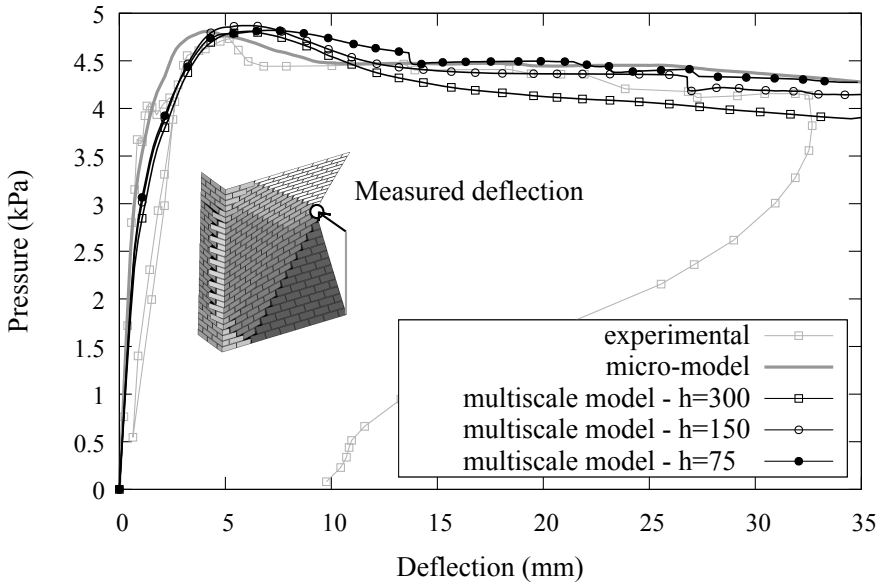

Figure 6.8: pressure-deflection curves obtained from the multiscale analyses

A satisfactory agreement can be seen between the homogenized responses and the micro-model response. Also the regularization of the response seems satisfactory, converging to a meaningful solution upon mesh refinement. A slight difference between the homogenized response and the DNS response can be seen for pressure values ranging from $3\,kPa$ to the peak load, with the homogenized models showing a softer response, thus leading to a slight overestimation of the displacement at peak strength, while the peak force is correctly predicted. This is believed to be due to the response given by connection (corner) between the main wall and the turning wall: in the micro-model, bricks from the front and lateral walls are physically connected. On the contrary, in the homogenized model this doesn't happen, with the RVEs being only *weakly* connected with one another (i.e. by means of the macroscopic homogenized strain), thus offering a slightly softer response. However, this initial small difference didn't seem to affect the overall response of the wall for the subsequent stages of the analysis.

Next, a detailed comparison between the DNS results and the Multiscale results is given. Figure 6.9 shows a comparison between the tensile and compressive damage patterns obtained from the three meshes used for the multiscale analyses, and those obtained

from the DNS. The failure modes are in very good agreement with the predictions of the DNS, both in terms of crack-direction and in terms of initial spread of non-linearity (i.e. before localization into a well defined rotational hinge). Note that the damage index displayed in the homogenized results is defined as the volume average of the damage indexes in the RVE, thus can never reach the unity, unless all the elements in RVE are completely damaged. However this definition of damage has no physical meaning, and it has been used just for post-process purposes. Real damage values can be retrieved only from the RVE. The vertical hinge formed in the turning wall near the intersection with the front wall, developed with a narrow damaged zone, while the diagonal hinges on the front wall involved a significantly larger damaged zone. This behavior is mainly due to the redistribution of compressive stresses, initially uniform over the entire wall, and progressively increasing towards the center of the front wall, as shown in Figure 6.10. In fact, as shown in Figure 6.11, the moment curvature response monitored along the diagonal hinge (compared to the response monitored on the vertical hinge) showed a more ductile behavior with a considerable initial hardening, since the shell cross section was there subjected to significant compressive stresses. Figure 6.12 shows a comparison in terms of rotations and out-of-plane deflection. A remarkable agreement can be seen for rotations, both qualitatively and quantitatively, properly capturing the position and orientation of the vertical (along the corner) and diagonal (on the front face) rotational hinges, as predicted by the micro-model analysis. Figure 6.13 shows a comparison in terms of shell moments. In this case a satisfactory agreement is found in the overall bending moments distribution, while, obviously, from a quantitative point of view the peak values showed by the micro-model are smoothed-out in the multiscale model, since they are average values obtained from the homogenized response of the RVE.
Finally, Figure 6.14 shows a last comparison in terms of tensile damage obtained from the micro-model, the homogenized model, and the actual damage distribution in some relevant RVEs. It can be noticed how all the relevant failure modes highlighted by the micro-model are correctly captured by the homogenized one. RVE 1 shows a bending failure mechanism about the head joints (vertical) direction. RVE 2, in the bottom-left corner of the wall, shows a transition from uniaxial bending about the head joints direction to diagonal bending. RVE 3 and RVE 4 show the damage pattern obtained from diagonal bending, with RVE 4 being on the localization band defined by the diagonal rotational hinge. RVE 5, in the center of the wall, shows a bending failure mechanism about the bed joints (horizontal) direction.

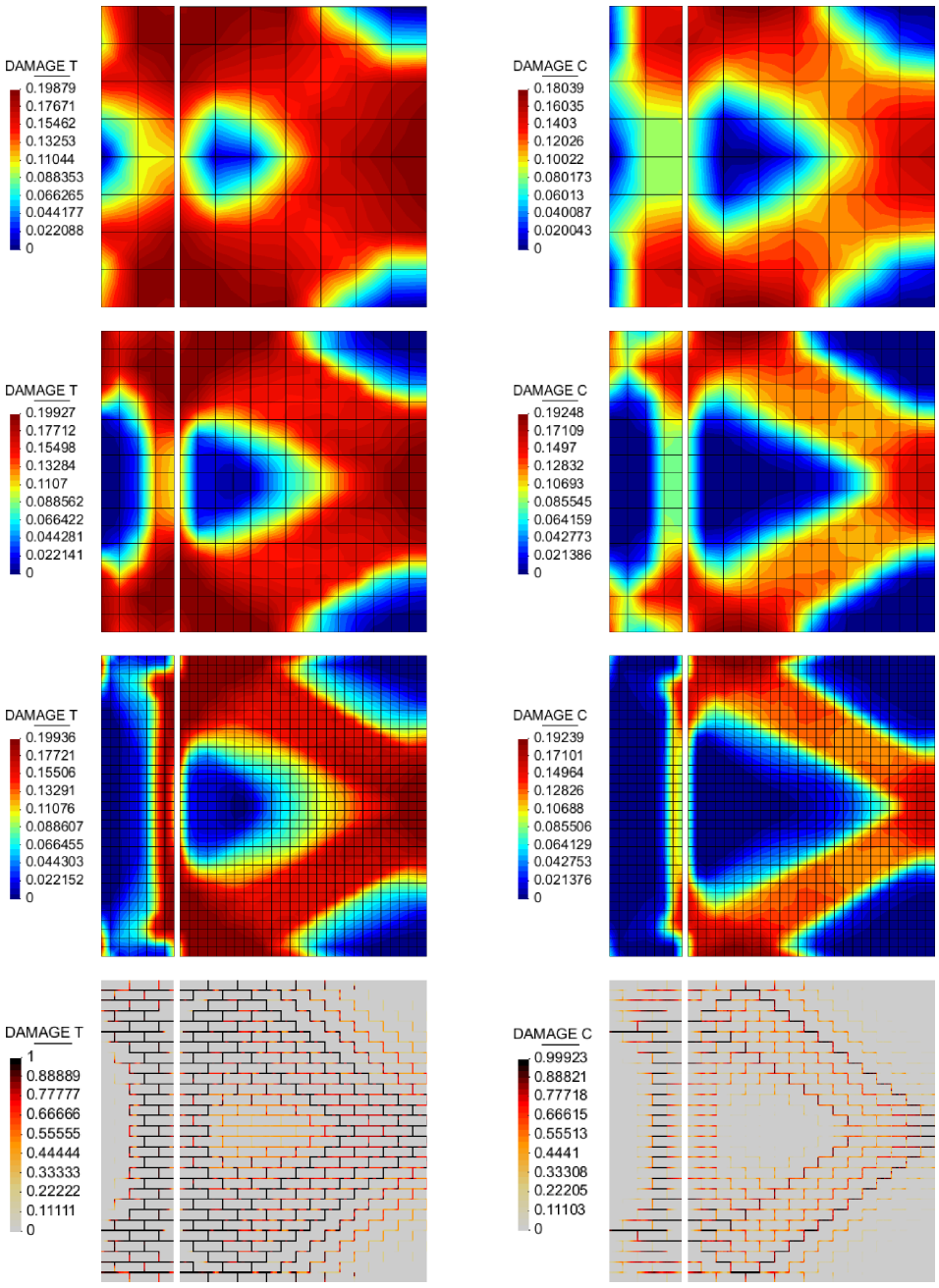

Figure 6.9: Comparison of tensile and compressive damage. Multiscale (first three rows) vs. DNS (last row)

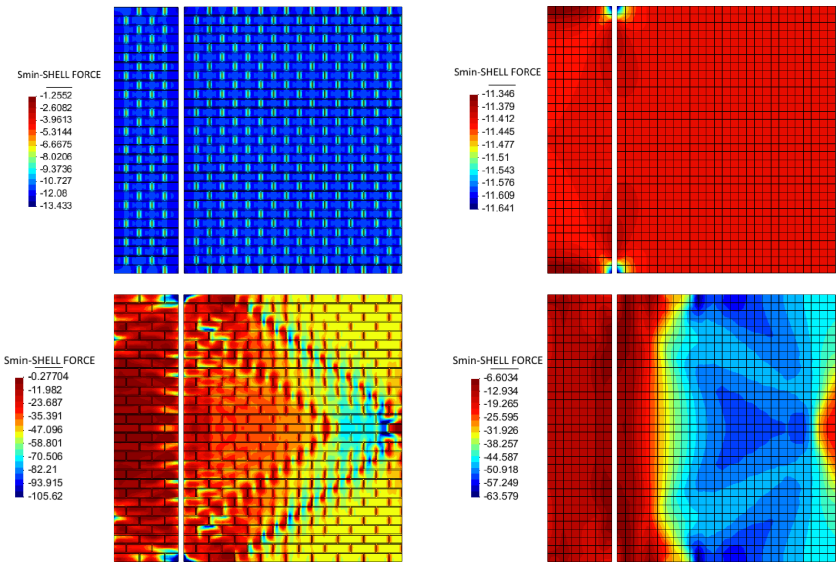

Figure 6.10: Comparison of minimum principal shell forces [N/mm], after the initial pre-compression (row 1) and at the end of the analysis (row 2). DNS (column 1) vs. Multiscale (column 2).

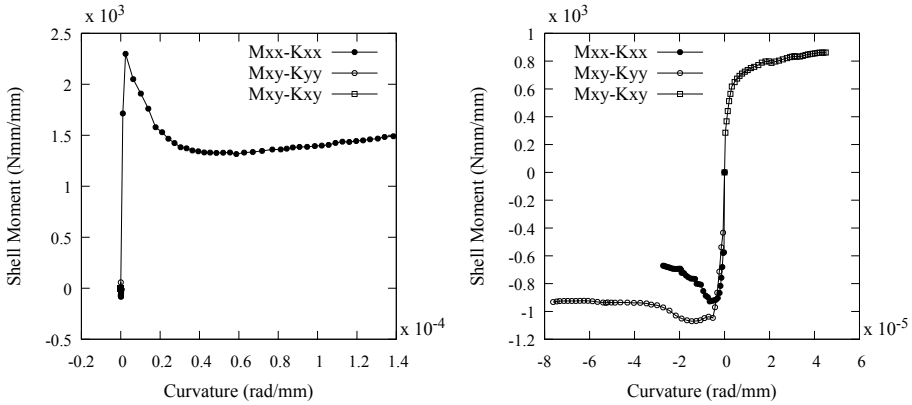

Figure 6.11: homogenized moment-curvature response: (a) at the center of the vertical hinge; (b) at the center of the bottom diagonal hinge

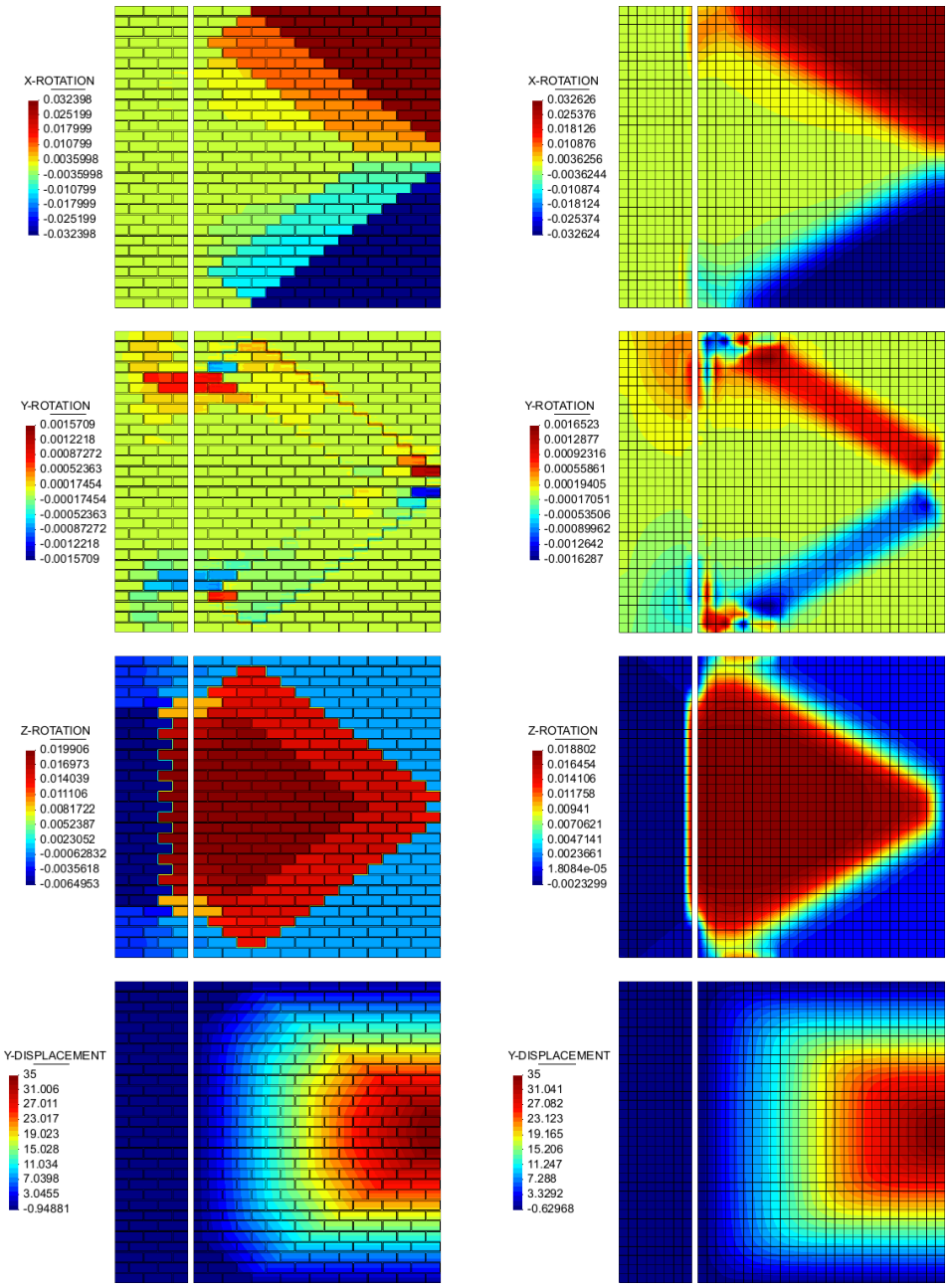

Figure 6.12: Comparison of rotations $[rad]$ (rows 1,2,3) and deflection $[mm]$ (row 4). DNS (column 1) vs. Multiscale (column 2).

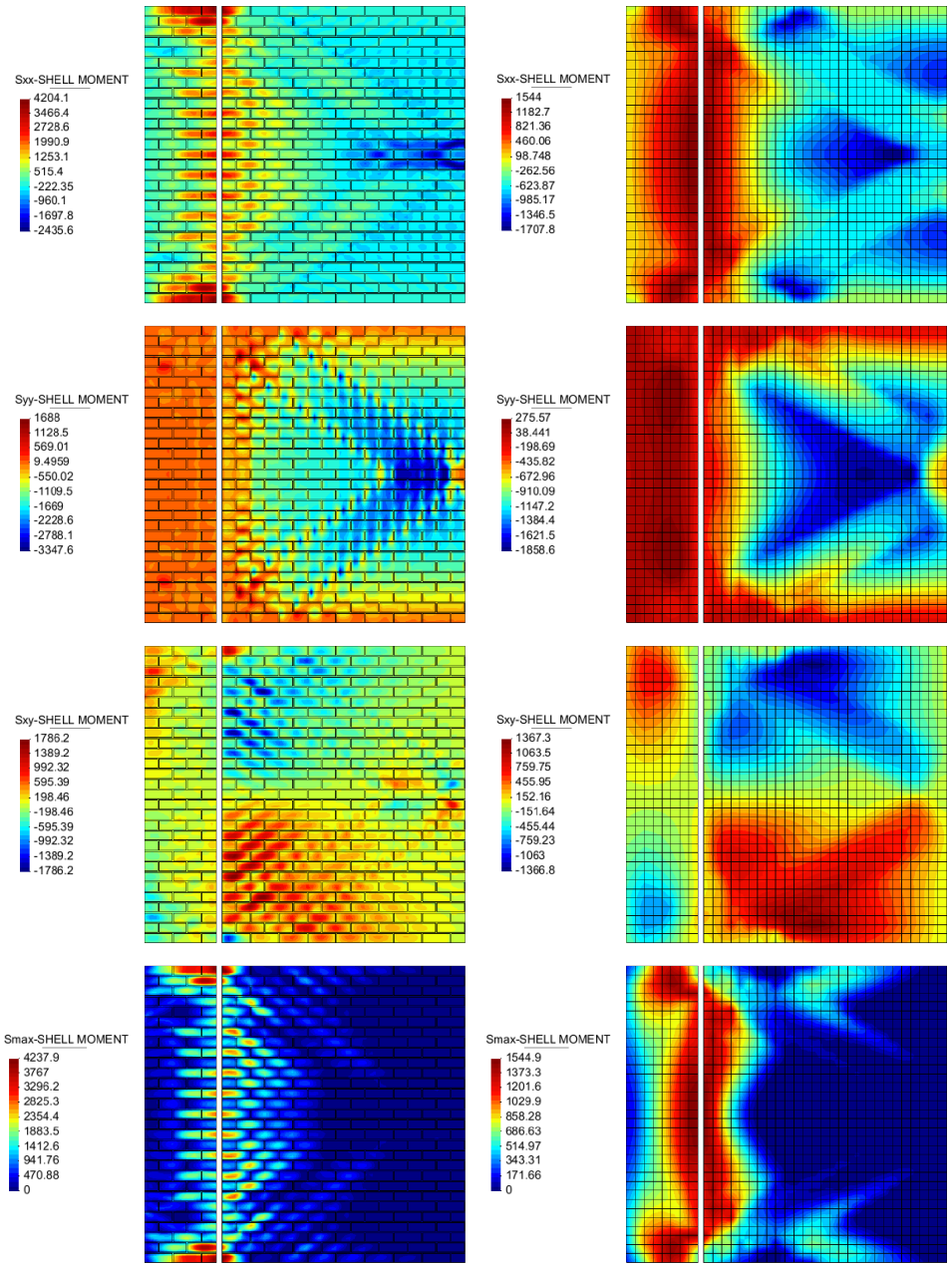

Figure 6.13: Comparison of shell moments [$^{\mathrm{Nmm}}/_{\mathrm{mm}}$]. DNS (column 1) vs. Multiscale (column 2).

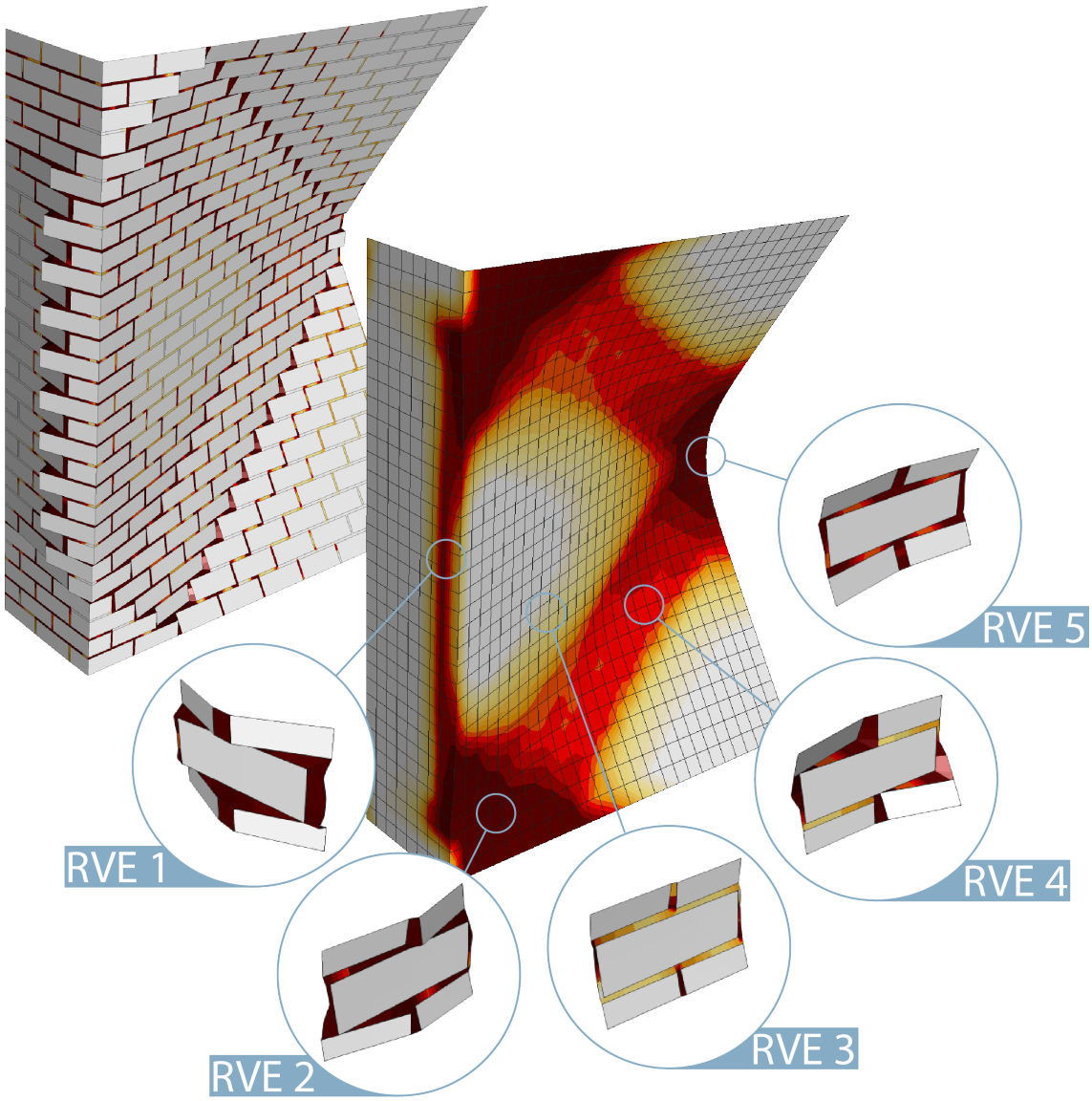

Figure 6.14: Distribution of tensile damage in some significant RVEs

This page is intentionally left blank

Chapter 7

Conclusions

7.1 Summary

The principal aim of this research was the development of a multiscale technique based on computational homogenization, tailored to the analysis of masonry structures under quasi-static in-plane and out-of-plane actions. The motivation for this research resides in the need for representing in an accurate way the mechanical behavior of masonry. From a structural point of view, masonry can be seen as a composite material, with a heterogeneous micro-structure consisting of units and joints. Large differences in elastic and inelastic properties, and diverse types of arrangement of units, give rise to very complex nonlinear behaviors and failure mechanisms. The overall response obtained at the structural scale is therefore highly influenced by the complex behavior of micro-structural phenomena.

A direct consequence of the complex heterogeneous micro-structure of masonry, is that the formulation of closed-form phenomenological constitutive models that treat masonry as an equivalent homogeneous medium is a considerably challenging task. Despite the initial orthotropy and initial strength domain, that could be eventually formulated based on results from experimental tests on masonry specimens, all subsequent non-linearities, damage-induced anisotropy and stress redistribution among constituents, are difficult to include into standard algorithms for nonlinear constitutive models. Furthermore, the huge variability in micro-structural configurations, would require a reformulation of the model for each new type of micro-structure. However these phenomenological macro-models are still a suitable solution for the analysis of large-scale structures due to their

reduced computational costs.

A way of accounting for the heterogeneity of the micro-structure is the so called micro-modeling, also known as Direct Numerical Simulation. With this numerical approach all the constituents of the micro-structure are physically modeled into the computational domain. Effective continuum and interface constitutive models for masonry constituents, with special emphasis on mortar joints, have been developed and deeply studied in the literature. In Chapter 2, a comparative analysis has been performed on typically used micro-modeling strategies for masonry structures, and a continuum damage model has been proposed, capable of satisfactorily representing the shear behavior of mortar joints. However the unaffordable costs of this modeling approach make it suitable only for detailed analyses of small-scale structures such as single structural members.

In the last years, with an ever-growing computational power, analytical homogenization methods have been complemented, in the context of multiscale analysis, with Computational Homogenization Methods. Computational Homogenization joins features of both macro-modeling and micro-modeling. The problem is split in two (or more) scales. The structural scale is treated as an equivalent homogeneous medium, while the complex behavior of the heterogeneous micro-structure is taken into account solving a nested micro-scale problem on a representative sample of the micro-structure (RVE). At the macro-scale no assumption is required on the constitutive behavior of the micro-structure, since it is fully obtained from the solution micro-scale problem. Classical computational homogenization assumes a Cauchy continuum theory at both scales, and it is referred to as First Order Computational Homogenization. A description of first order computational homogenization has been given in Chapter 3.

Due to its flexibility, first order computational homogenization has been used to model a large range of micro-structures, including material and geometric non-linearities. However, it has been soon recognized that this method performs poorly when strain-softening is considered in the micro-structure. When this happens, the RVE looses its representativeness, failing to give a homogenized response which is objective with respect to the RVE size and to the macro-FE size. Several enhancements to the first order homogenization have been proposed in the last years to overcome this problem, including discontinuous-continuous homogenization methods, and homogenization methods based on generalized continua. This research has proposed, in Chapter 3, an extension of the well known fracture energy based regularization to the two-scale homogenization problem, allowing the usage of first order homogenization for problems involving brit-

tle failure. The resulting regularized first order homogenization has been used in the numerical simulation of in-plane loaded shear walls made of periodic brick-masonry, as described in Chapter 4. The proposed method proved accurate in predicting the main in-plane failure mechanisms encountered in the experimental tests and reproduced by the micro-models. Furthermore the regularization capabilities of the proposed 2-scale fracture energy regularization have been assessed.
The subsequent step in this research was towards the analysis of the out-of-plane behavior of masonry walls. For this purpose, the homogenization method presented in the first part of this work has been extended to shell theory in Chapter 5. A computational homogenization framework for thick shells has been proposed, that is tailored to the analysis of heterogeneous surfaces, which are however homogeneous in the thickness direction. This assumption, which holds, for example, for single-leaf masonry walls, leads to a coupling between micro- and macro-scales both governed by the same (shell) theory. In Chapter 6 the numerical simulation of experimental results on out-of-plane loaded masonry walls has been carried out. The experimental results have been first simulated with micro-modeling, where the continuum damage model proposed in Section 2.2 has been used in conjunction with a through-the-thickness integration to obtain a constitutive model for shells. It has been particularly highlighted how, even if the wall can be considered as a thin structure, the effects of transverse shear deformation cannot be neglected, and therefore they should be included into the nonlinear constitutive response. Then the same analysis has been performed with the proposed computational homogenization method for shells, and a detailed comparison between micro-model and multiscale model results has been done. The proposed method has shown to be an effective tool to capture the nonlinear response of masonry under out-of-plane actions. A good agreement among experimental, micro-model and multiscale model results has been obtained. Also in this case the objectivity of the response with respect to the discretizations size has been verified.

7.2 Main contributions

The main novelties presented in this research mainly resided in the following contributions:

- The formulation of a regularized first order computational homogenization method.

The simple format of classical first order computational homogenization is retained in the proposed approach, since the regularization method only acts at the level of constitutive models at the micro-scale. At the same time, it satisfactorily accounts for the different characteristic lengths entering the 2-scale homogenization problem.

- The extension of the previously mentioned regularized homogenization for standard 2D/3D continua, to the case of thick shells. In this regard, the proposed homogenization allows an efficient coupling of a macro-scale and a micro-scale both described by the same shell theory.

- The formulation of a bi-dissipative continuum damage model, able to correctly represent the dilatancy of mortar joints, as opposed to standard isotropic damage models. The proposed model is based on the original d^+/d^- damage model, and it takes advantage of the *interaction* between tensile and compressive failure surfaces to control dilatancy.

- A fruitful discussion and comparison of three different micro-modeling strategies typically used for masonry. In this context, the proposed damage model has been validated and compared to well-established interface constitutive models present in literature.

7.3 Suggestions for future works

Overall, the proposed multiscale technique has shown to be rather accurate in predicting all the relevant failure mechanisms exhibited by a complex heterogeneous material such as masonry, both for the in-plane and for the out-of-plane cases. Computational Homogenization has proven to be a promising tool to study and deeply understand the complex behavior of masonry. Obviously there is still room for improvements. Some ideas for future works are listed here:

- In all the analyses shown in this work, an effective reduction of computational costs with respect to micro-modeling has been noticed. However, this seemed not sufficient for large scale simulations. In the present work, all macroscopic finite elements are equipped with RVEs from the very beginning of the analysis. It should be noted however that a performance boost can be obtained with a selective switch

between classical 1-scale constitutive models to RVE-based constitutive models only in those parts of the structure violating some pre-defined criteria.

- In the shell homogenization, periodicity conditions have been used for all the components of the micro-displacement/rotation vector. This has been motivated by the good results obtained from the 2D homogenization for shear walls with periodicity conditions. However further detailed studies on different types of boundary conditions for rotations and deflection are necessary.

- The proposed shell homogenization relies on the assumption that the heterogeneous mid-surface is homogeneously extruded in the thickness direction. This is true for single-leaf masonry walls, but not in the general case. In the general case, a full 3D RVE discretizing the entire thickness of the shell might be required. Further study on this subject are to be done.

- In all multiscale analyses shown in this work, only a continuum description of both bricks and mortar has been used, in particular with the proposed continuum damage model. A comparison with a discrete description of the micro-structure by means of interface elements has been performed only for micro-modeling. The same comparison in the context of multiscale analysis might be of interest.

- In the same line of thought, a formulation of an interface element for shells (featuring displacement and rotation jumps) might be an interesting topic, together with a discussion on its usage in micro-model analyses and shell homogenization analyses.

This page is intentionally left blank

Appendices

The following appendices collect some in-depth discussions about the concepts explained in the preceding chapters, in terms of numerical aspects and implementation details. All these considerations were postponed to these appendices in order to streamline the discussion in the previous chapters, without focusing on specific matters. Appendix A explains the problem of mesh-bias dependency induced by strain softening, since this aspect cannot be solved by the regularization procedure presented in Chapter 3. Appendix B focuses on a general usage of fracture energy regularization in different contexts, where a trivial implementation can lead to poor results. Finally Appendix C presents the issues arising from the different RVE boundary conditions when strain softening appears, and the motivations that led to the use of periodic boundary conditions in all the numerical examples shown in this work.

Appendix A

On the dependency on mesh orientation

Throughout this work, due to the brittle nature of masonry, the issue of strain softening in the discrete (FEM) problem has been a major concern. In the previous chapters, the dependency of the solution on the spatial discretization was generally referred to as *mesh dependency*. It should be observed, however, that the regularization procedure presented in Chapter 3 can only solve the problem of *mesh size dependency*. In this sense the proposed regularization, following the idea of Bažant Bažant and Oh (1983), only addresses the dependence of the solution on the mesh size and aims at ensuring that the total amount of dissipated energy is objective with respect to the *discretization size*. Nevertheless, another (probably harder to solve) kind of mesh dependency is known to spoil the solution: the so called *mesh bias* or *mesh orientation dependency*. When this issue occurs, the solution is biased by the orientation of the spatial discretization, i.e. the strain localization band tends to follow preferred directions dictated by the mesh orientation. This problem has been studied in detail in several works Cervera et al. (2010a), Benedetti et al. (2015), Cervera and Chiumenti (2006), Cervera et al. (2010b), Pelà et al. (2014b), Oliver et al. (2014c), Saloustros et al. (2015a). In Cervera and Chiumenti (2006), Cervera et al. (2010b), Pelà et al. (2014b), Oliver et al. (2014c), Saloustros et al. (2015a) tracking techniques for the propagation of material failure have been used, while in Cervera et al. (2010a), Benedetti et al. (2015) an efficient mixed FE formulation has been presented, showing a very accurate response both in terms of stress prediction and in terms of strain localization direction.

This is a very involved topic, and it is not the main subject of this work, so the reader should refer to the previously cited works for major details. However this problem cannot be neglected. Therefore this section presents the FE formulation adopted throughout this work in order to alleviate the mesh bias dependency.

A.1 Enhanced Assumed Strain method

The FE formulation adopted in all the numerical examples shown in this work, both for the 2D plane stress case and the 3D shell case, is an irreducible (displacement-based) 4-node finite element with an enhancement of the strain field according to the Enhanced Assumed Strain (EAS) formulation presented in Simo and Rifai (1990). For the 2D plane stress case, this enhancement involves the entire strain field, while for the shell case this enhancement has been used only for the membrane part. Furthermore for the thick shell formulation, a further enhancement is required to avoid the well-known problem of transverse shear locking, and the Mixed Interpolation of Tensorial Components (MITC) formulation Bathe and Dvorkin (2005) has been used (observe that in Simo and Rifai (1990) it has been shown how the enhanced transverse shear strain given by the MITC formulation can be equivalently obtained through the EAS formulation).
Focusing now on the 2D plane stress case (which obviously applies to the membrane part of the shell), the EAS assumes that the strain field can be defined as a sum of a compatible strain component and an enhancing strain component:

$$\boldsymbol{\varepsilon} = \nabla^s \boldsymbol{u} + \tilde{\boldsymbol{\varepsilon}} \tag{A.1}$$

In the EAS the enhancing strain is assumed in the iso-parametric space, and then transformed to the physical space (see Simo and Rifai (1990) for major details). The enhancing strain $\tilde{\boldsymbol{E}}$ in iso-parametric space, as originally proposed in Simo and Rifai (1990), is

$$\tilde{\boldsymbol{E}} = \mathbf{E}(\boldsymbol{\xi})\boldsymbol{\alpha} = \begin{bmatrix} \xi & 0 & 0 & 0 & \xi\eta \\ 0 & \eta & 0 & 0 & -\xi\eta \\ 0 & 0 & \xi & \eta & \xi^2 - \eta^2 \end{bmatrix} \boldsymbol{\alpha}; \qquad \boldsymbol{\alpha} \in \mathbb{R}^5 \tag{A.2}$$

where $\mathbf{E}(\boldsymbol{\xi})$ is the enhancing strain interpolation matrix, and $\boldsymbol{\alpha}$ is a vector containing the 5 enhancing strain parameters (internal DOFs). Such a definition of the enhancing

strains, corresponds to an assumed stress field $\boldsymbol{\Sigma}(\boldsymbol{\xi})$ in iso-parametric space of the form

$$\boldsymbol{\Sigma}(\boldsymbol{\xi}) = \begin{bmatrix} 1 & 0 & 0 & \eta & 0 \\ 0 & 1 & 0 & 0 & \xi \\ 0 & 0 & 1 & 0 & 0 \end{bmatrix} \boldsymbol{\beta}; \qquad \boldsymbol{\beta} \in \mathbb{R}^5 \tag{A.3}$$

This element with 5 enhanced strain parameters (from now on called Q4E5) solves the two major errors produced by a compatible bi-linear quadrilateral element (Q4) when subjected to pure bending, namely the appearance of spurious shear stresses (shear locking) and the appearance of transverse (to the direction of bending) stresses due to Poisson's ratio effect. The stress field produced by this element has the Σ_{xx} and Σ_{yy} components linear in η and ξ respectively, while the shear stress Σ_{xy} is constant. However, when strain softening is present, this element may localize in only two of the four Gauss points when subjected to mode I failure, due to the linear enhanced direct strain components, spoiling the convergence of the solution when strain softening appears, as it will be shown in the following numerical examples. To avoid this issue, a different assumed strain field has been used in the present work:

$$\tilde{\boldsymbol{E}} = \mathbf{E}(\boldsymbol{\xi})\boldsymbol{\alpha} = \begin{bmatrix} 0 & 0 \\ 0 & 0 \\ \xi & \eta \end{bmatrix} \boldsymbol{\alpha}; \qquad \boldsymbol{\alpha} \in \mathbb{R}^2 \tag{A.4}$$

This element with 2 enhanced strain parameters (from now on called Q4E2) only solves the problem of shear locking, producing a stress field with constant shear stress. This element is thus slightly less accurate than the Q4E5 in the general case, but in the particular case of strain softening it has shown the desired effect of alleviating the mesh bias dependency, without the undesired effect of localizing in only half of the Gauss points.

A.2 Numerical example

In the following, the performance of the Q4E2 element with respect to strain localization and mesh-bias dependency is assessed, and the results are compared to those obtained from the standard displacement-based Q4 element and the Q4E5 element. The numerical test adopted here is the one studied in Cervera et al. (2010a). The model consists of

a rectangular strip under uniaxial vertical stretch. The geometry and dimensions are shown in Figure A.1. Ideally this problem should show a constant state of deformation. To perturb this uniform state and to trigger localization, two notches are inserted at the ends of the central axis of the model. The nonlinear constitutive model used here is an isotropic damage model with a Rankine criterion (see Section 3.7), with the following material parameters: Young's modulus $E = 2000\,\mathrm{N/mm^2}$, Poisson's ratio $\nu = 0$, tensile strength $f_t = 1\,\mathrm{N/mm^2}$, and fracture energy $G_f = 0.25\,\mathrm{N/mm}$. The expected crack is a horizontal line between the two notches. To assess the ability of the tested elements with respect to mesh-bias, two meshes are used. The first one consists of elements aligned with the theoretical crack direction, while the second one consists of elements whose horizontal edges are distorted, with an angle of -13° from the horizontal theoretical crack direction. In both cases the typical size of the elements is about $2.25\,mm$.

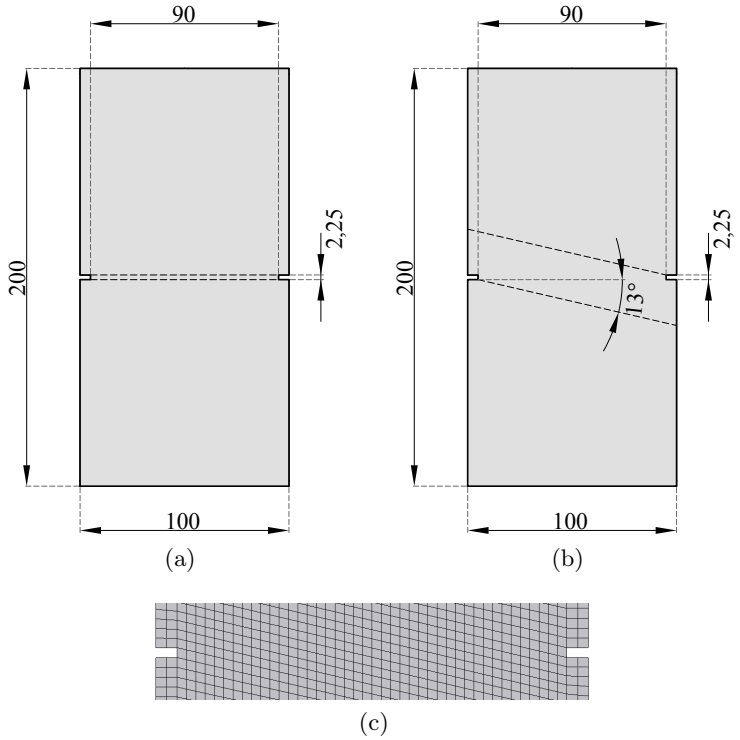

Figure A.1: Geometry. (a) Aligned, (b) Distorted. All units are in [mm]. (c) Detail of the distorted mesh.

The results obtained by the standard Q4 element with the aligned mesh are shown in Table A.1. As highlighted in Cervera et al. (2010a), despite its basic formulation, the standard Q4 element is able to represent the exact solution when the mesh is aligned with the theoretical crack direction. The initial state of stress is almost uniform (apart from the small perturbations given by the notches), and it remains so at the end of the simulation.

	d	ε_{max}	σ_{max}
(a)	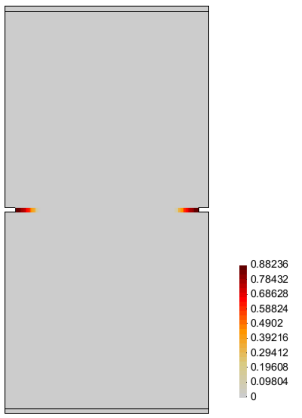	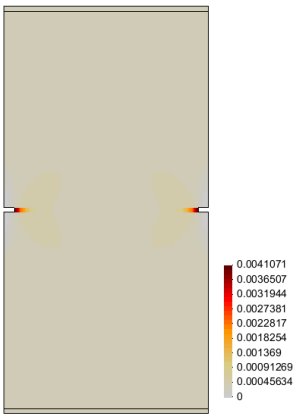	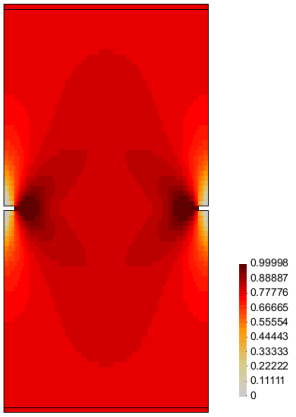
(b)	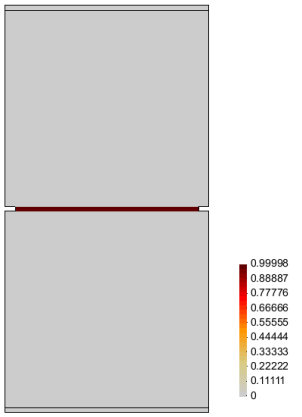	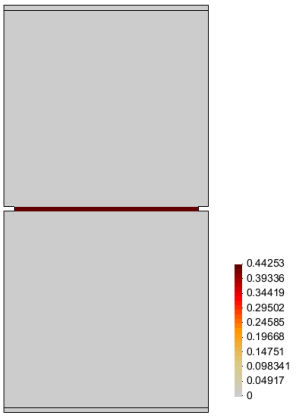	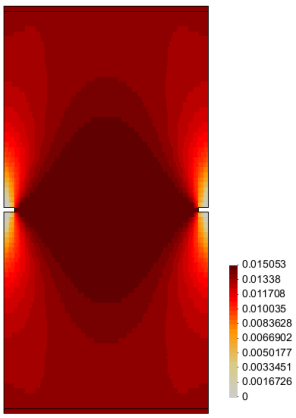

Table A.1: Q4 element. Aligned mesh. (a) Onset of localization, (b) localized solution

However, as soon as the mesh is distorted from the crack direction, the localization band follows preferential directions dictated by the mesh orientation, thus substantially deviating from the exact solution, as shown in Table A.2.

	d	ε_{max}	σ_{max}
(a)	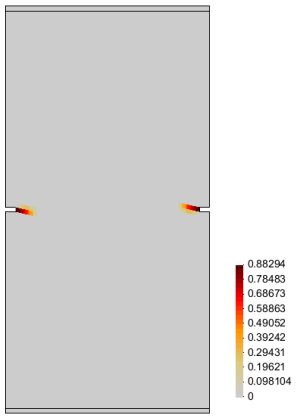	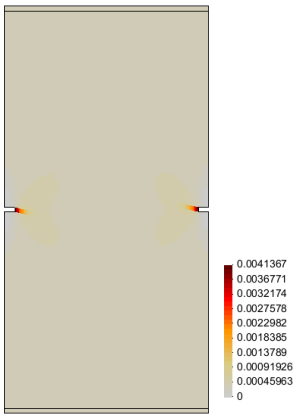	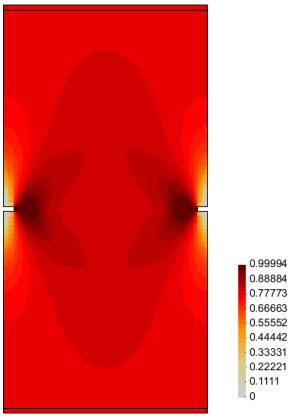
(b)	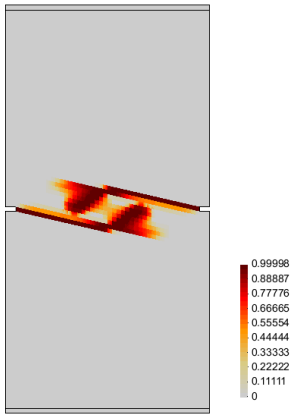	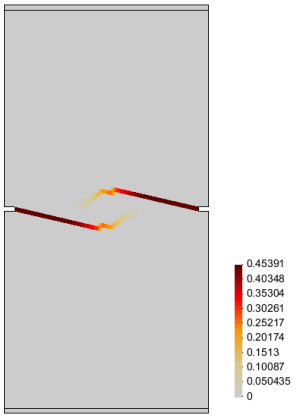	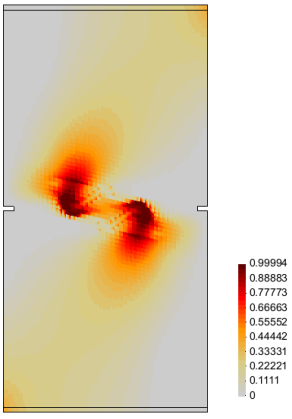

Table A.2: Q4 element. Distorted mesh. (a) Onset of localization, (b) localized solution

Next the Q4E5 element (Eq. (A.2)) is analyzed. The obtained results are shown in Table A.3. It can be noticed that, compared to the Q4, the overall predicted direction of the localization band is closer to the horizontal line. However it is also evident how the linear nature of the enhanced extensional strain components induces a strain localization

only in half of each element. This behavior has shown some collateral issues. The half-element-localization itself is not a problem, but since the enhanced strains are local to each element, there's no guarantee that the same half-portion of two adjacent elements localizes. This has shown to generate spurious stress concentrations and subsequent spread of damage.

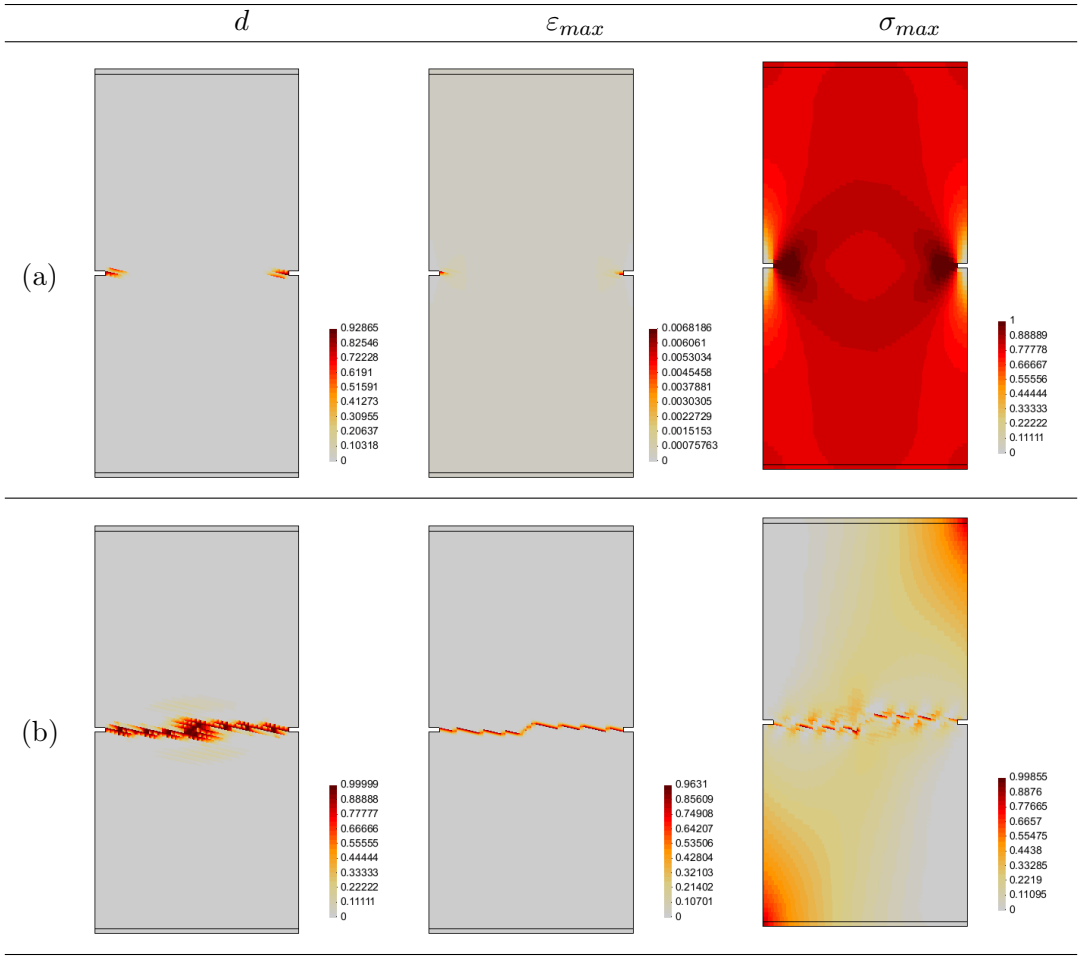

Table A.3: Q4E5 element. Distorted mesh. (a) Onset of localization, (b) localized solution

However the Q4E2 element (Eq. (A.4)) does not show this half-element-localization, and the direction of the predicted localization band is sufficiently acceptable. The localization

band follows few distorted elements (3 or 4 in this example), and then jumps to the next distorted row of elements, in the attempt of approximating the theoretical horizontal crack. The spurious spread of damage shown by the Q4E5 element is greatly reduced. Also reduced are the spurious stresses around the crack. Now only some elements show spurious stress concentrations, namely those located at the jump between two adjacent distorted rows of elements. This is mainly due to the excessive distortion that a FE should undergo in order to move the localization band to the next row of elements.

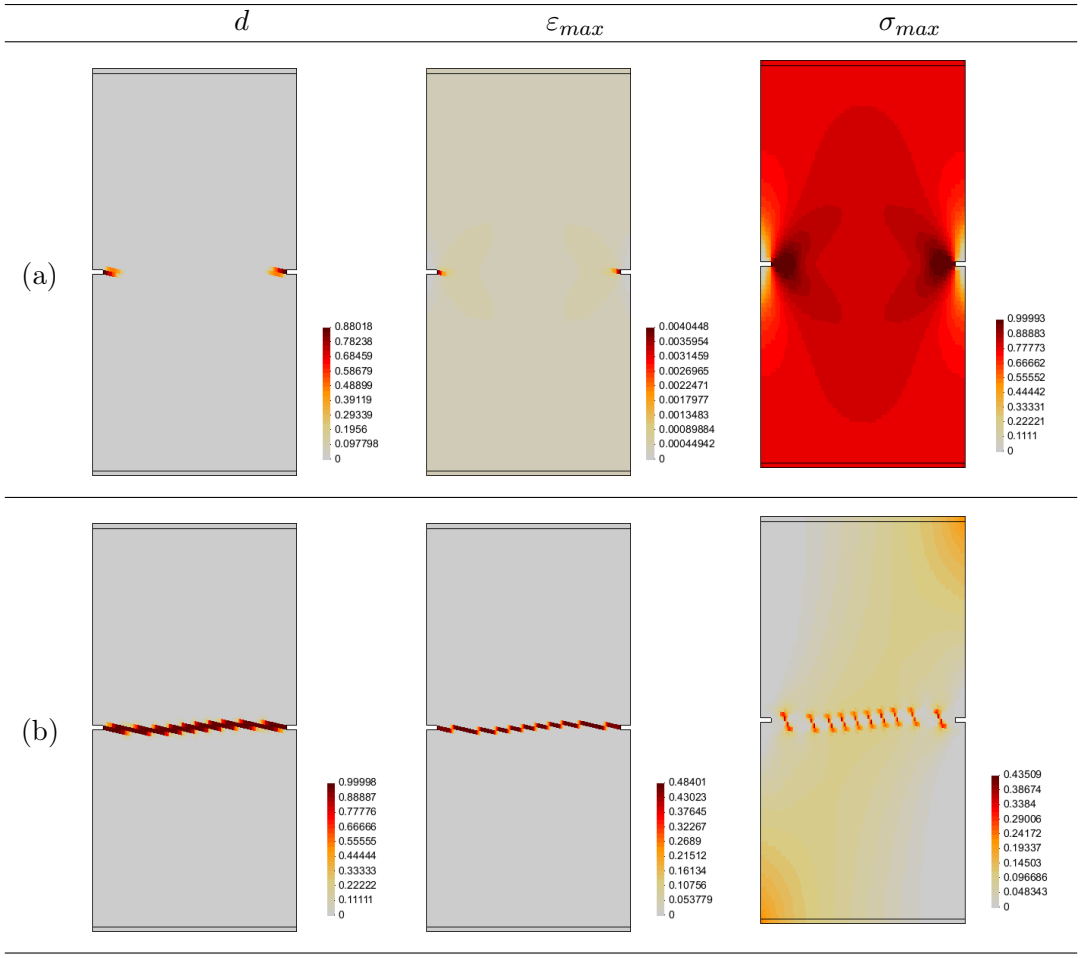

Table A.4: Q4E2 element. Distorted mesh. (a) Onset of localization, (b) localized solution

Finally Figure A.2 compares the response of previously discussed results, in terms of vertical displacement and base reaction. The Q4 element with distorted mesh shows the higher overestimation with respect to the reference solution given by the Q4 element with aligned mesh. The Q4E2 shows a better behavior, also slightly better than the Q4E5. However a certain overestimation in the amount of dissipated energy is still visible. This is mainly due to the fact that the localization band follows a zig-zag path, in order to approximate the exact horizontal crack, thus dissipating slightly more energy.

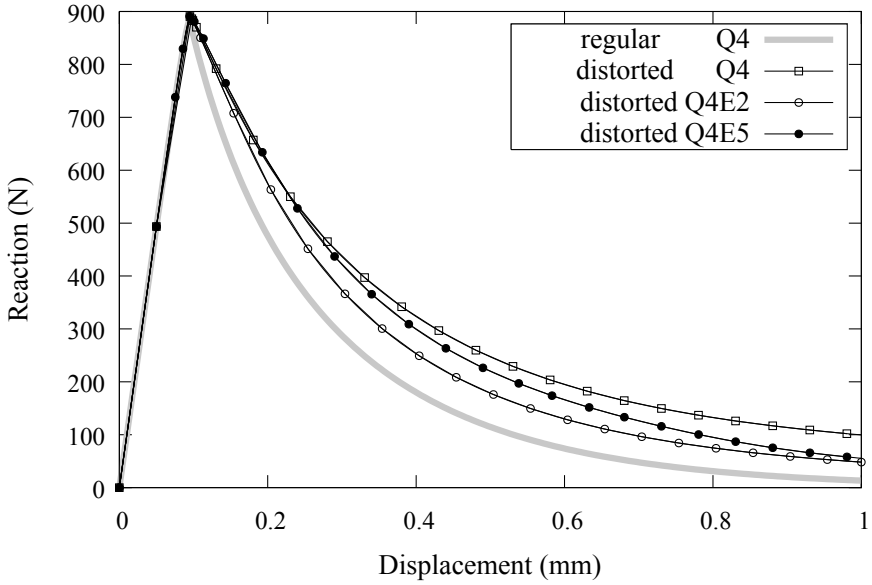

Figure A.2: Load displacement curves

Appendix B

On fracture energy regularization in 1-scale and 2-scale problems

In the FEM context, regularization of fracture energy with respect to the element size, was proposed first in Bažant and Oh (1983), and later on addressed by several authors (Cervera and Chiumenti (2006), Oliver (1989), Oller (2001), among others). The computational width of the fracture process is computed in each element depending on its geometry and dimension. This computational width is known as the element characteristic length l_{ch}. According to this model, the softening law depends on both the material fracture energy per unit of crack surface area G_f and the element characteristic length l_{ch}, in such a way that the following relation holds:

$$G_f = \frac{W}{A} = \frac{W}{V} l_{ch} = g_f \, l_{ch} \tag{B.1}$$

In Chapter 3 it was shown how this method has been extended to the 2-scale problem based on Computational Homogenization, by substituting the characteristic length of the element containing the localizing constitutive law, with a generalized characteristic length that accounts for all the *characteristic lengths* entering the problem: the size of the microscopic element containing the localized constitutive law, the size of the localized RVE, and the size of the macroscopic element showing the localizing homogenized constitutive response.

Despite the simple format of this method, its effectiveness strongly relies on the computational implementation. In the following, it will be shown how a basic implementation

may fail to give acceptable results in certain particular cases.

B.1 The trivial case

Fracture energy regularization, in the framework of the smeared crack approach, consists in evaluating the hardening/softening uniaxial law using the fracture energy per unit volume $g_f = G_f/l_{ch}$ in place of the fracture energy per unit area G_f. A trivial implementation performs this regularization from the very beginning of the analysis, as soon as the peak strength is reached in the uniaxial hardening/softening law. Indeed this assumption holds if strain localization happens (approximately) when this peak is reached. This can be considered true in standard 1-scale analyses using continuum elements. Typical cases commonly encountered in engineering practice are:

- linear elastic response, followed by strain softening (for example tensile behavior of masonry)
- linear elastic response, followed by initial strain hardening and final softening (for example compressive behavior of masonry)

Fracture energy regularization in 1-scale problems is very well-known, at least for the tensile case. In literature, regularization of strain softening in compression has been sometimes disregarded, probably due to the presence of an initial strain hardening. It should be noted however that from a numerical point of view both tension and compression need to be regularized when they experience softening. This is even more necessary when continuum constitutive models such as the one presented in Section 2.2 are used, where the shear behavior is not explicitly given, but it results from a combination of tensile and compressive responses.
This section shows how to perform such a regularization. A procedure for the regularization of the most-general piece-wise linear hardening/softening law is presented, and a simple validation uniaxial example is given. For the sake of generality, the hardening/softening law will consider initial hardening followed by softening and final residual constant stress plateau.
Let us assume an experimental test with a specimen with height H_{spec} (see Figure B.1a). The specimen, subjected to uniaxial tension, gives a stress-displacement response (see Figure B.1a) from which we can calculate the fracture energy per unit area G_f. Let us

now obtain a stress-strain response (see Figure B.1b) dividing the displacement by H_{spec}. This is the non-regularized (input) curve, where the energy per unit volume $g_f = \frac{G_f}{H_{spec}}$. The regularization process is as follows.

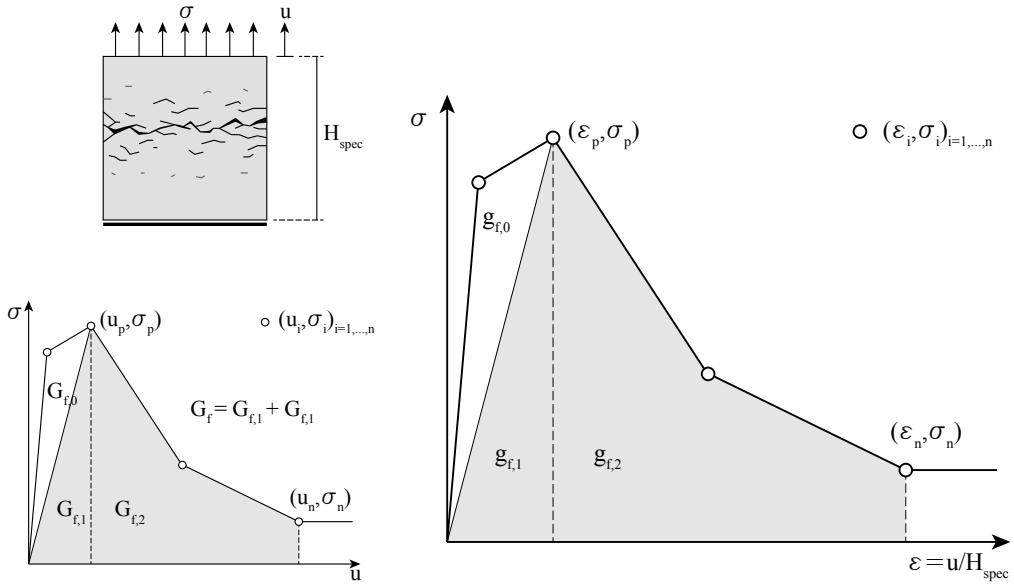

(a) stress-displacement curve (b) stress-strain curve

Figure B.1: General piece-wise linear hardening/softening law.

Given a piece-wise linear curve, of the type given in Figure B.1b, described by n pairs $(\varepsilon_i, \sigma_i)_{i=1,\dots,n}$, under the following assumptions:

- abscissas ε_i are monotonically increasing: $\varepsilon_1 < \varepsilon_2 < \cdots < \varepsilon_n$;
- p is the index of the peak value $(\varepsilon_p, \sigma_p)$;
- $\frac{\sigma_1}{\varepsilon_1} = E_0$ is the Young's modulus;

The hardening variable $\Sigma(\xi)$ at a certain strain abscissa ξ can be easily evaluated by linear interpolation of the piece-wise linear hardening/softening law, using $\Sigma(\xi) = \sigma_n$ if $\xi > \varepsilon_n$ that will eventually consider a final residual plateau if $\sigma_n > 0$. The fracture energy per unit volume g_f of the non-regularized (input) curve, corresponding to the shaded area shown in Figure B.1b can be calculated as follows:

$$g_f = g_{f,1} + g_{f,2} = \frac{\varepsilon_p \sigma_p}{2} + \sum_{i=p+1}^{n} \left[\frac{(\sigma_i + \sigma_{i-1})(\varepsilon_i - \varepsilon_{i-1})}{2} \right] \tag{B.2}$$

Eq. (B.2) calculates the area $g_{f,2}$ underneath the curve from the peak $(\varepsilon_p, \sigma_p)$ to the last point$(\varepsilon_n, \sigma_n)$ before the the residual stress. The term $g_{f,1} = \frac{\varepsilon_p \sigma_p}{2}$ is added according to the secant unloading typical of damage models. In case of plasticity models this term should be computed as $g_{f,1} = \frac{\sigma_p^2}{2E_0}$, according to the elastic unloading. Note that only $g_{f,1}$ and $g_{f,2}$ are considered in the regularization process. $g_{f,0}$ in Figure B.1b is not considered since this part of energy is dissipated during the strain hardening regime, thus before the onset of strain regularization. This concept is graphically represented in Figure B.2.

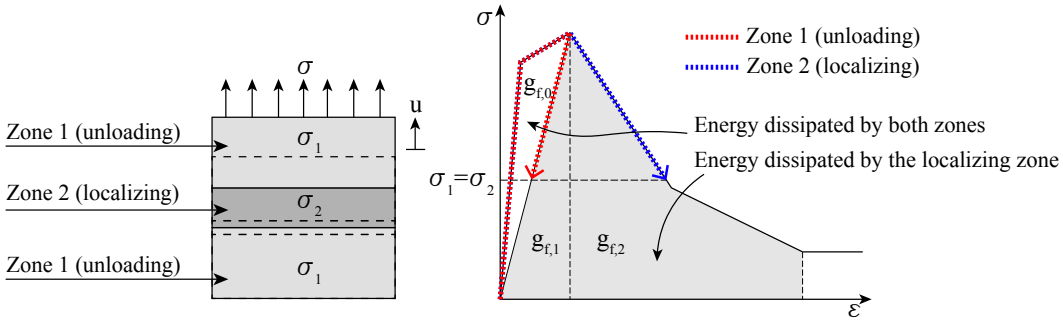

Figure B.2: Energy dissipated during strain hardening and during strain softening, according to damage models (secant unloading).

With damage models such as that presented in Section 2.2, the damage threshold r, is a stress-like variable. So its strain-like counterpart ξ can be computed as

$$\xi = \frac{r}{E} \tag{B.3}$$

and once evaluated the hardening variable $\Sigma(\xi)$ from the hardening/softening law, the damage variable $d(r)$ can be computed as

$$d(r) = 1 - \frac{\Sigma(\xi)}{r} \tag{B.4}$$

In the discrete problem, to guarantee invariance of the dissipated energy with respect to the size of the spatial discretization, the fracture energy $g_f = \frac{G_f}{H_{spec}}$ underneath the curve should be replaced with $\tilde{g}_f = \frac{G_f}{l_{dis}}$. For the general case of a piece-wise linear hardening/softening law, this scaling of the fracture energy can be performed *"stretching"* the strain abscissas by a stretch factor $\mathcal{S}$, to obtain the stretched abscissas $\tilde{\varepsilon}_i$:

$$\tilde{\varepsilon}_i = \varepsilon_i + \mathcal{S}\left(\varepsilon_i - \varepsilon_p\right), \qquad i = p+1, \ldots, n \tag{B.5}$$

Rewriting Eq. (B.2) in terms of the stretched post-peak abscissas $\tilde{\varepsilon}_i$, and equating it with the regularized fracture energy $\tilde{g}_f$, the following equation is obtained

$$\frac{G_f}{l_{dis}} = g_{f,1} + \tilde{g}_{f,2} = \frac{\varepsilon_p \sigma_p}{2} + \sum_{i=p+1}^{n} \left[\frac{\left(\sigma_i + \sigma_{i-1}\right)\left(\tilde{\varepsilon}_i - \tilde{\varepsilon}_{i-1}\right)}{2} \right] \tag{B.6}$$

By a straightforward manipulation of Eq. (B.6), the stretch factor is obtained as:

$$\mathcal{S} = \frac{\dfrac{G_f}{l_{dis}} - g_{f,1}}{g_f - g_{f,1}} - 1 \tag{B.7}$$

For $l_{dis} = H_{spec}$, the stretching factor $\mathcal{S}$ is equal to 0, thus providing no change in the abscissas ε_i. For values of $l_{dis} > H_{spec}$, the stretching factor will have negative values, thus stretching the abscissas ε_i towards the peak abscissa ε_p. However $\mathcal{S}$ should be greater than -1.0 to avoid a constitutive snap-back. In fact for a stretch factor $\mathcal{S} = -1.0$ every post-peak strain-abscissa would collapse to the peak strain ε_p, leading to a sudden fall of the uniaxial curve. To avoid this, the characteristic length l_{dis} should satisfy the following restriction:

$$l_{dis} < \frac{2G_f}{\sigma_p \varepsilon_p} \tag{B.8}$$

To assess the regularization with respect to the size of the spatial discretization, a simple uniaxial example is given here. A bar of unit length $L = 1$ and unit cross sectional area $A = 1$ is considered, so that the expected global displacement-reaction response should coincide with the input hardening/softening curve. The bar is discretized with 1,2,4,8 and 16 elements, to check the regularization of the response. One element has been assigned a slight 1% reduction of the tensile peak strength to perturb the uniform

state of deformation and to trigger strain localization. Note that during the following simulations, the case with one element will always give the exact solution, regardless of the regularization process ($l_{dis} = L = 1$).

Figure B.3 shows the response without any regularization, which, as expected, produces divergent responses, with finer discretizations showing more brittleness. Figure B.4 shows the response of the bar using the proposed regularization, regularizing a fracture energy $g_f = g_{f,1} + g_{f,2}$. Figure B.5 instead shows the response of the proposed regularization performed in an incorrect way, i.e. considering, during the regularization process, the whole area under the curve, including the energy dissipated during strain hardening. In both cases the responses converge to a unique solution. However, when incorrectly considering the energy under the hardening part, the converged solution is not the exact one (given by the 1 element mesh).

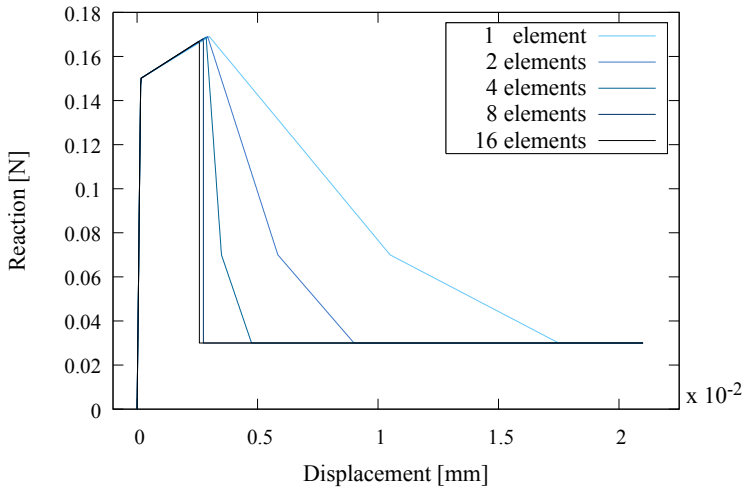

Figure B.3: Reaction-Displacement curve. Non regularized response.

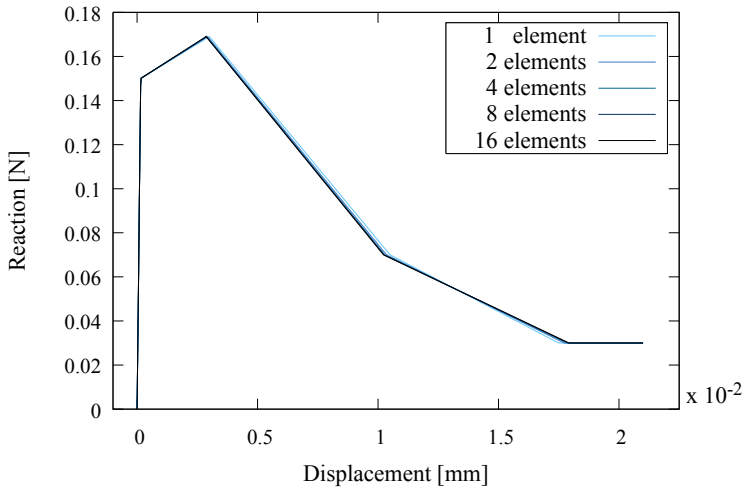

Figure B.4: Reaction-Displacement curve. Regularized response with $\frac{G_f}{l_{dis}} = g_{f,1} + \tilde{g}_{f,2}$.

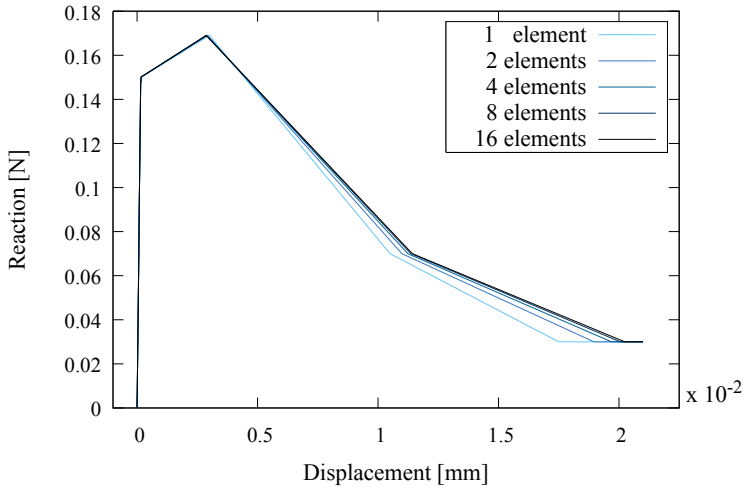

Figure B.5: Reaction-Displacement curve. Incorrectly regularized response with $\frac{G_f}{l_{dis}} = g_{f,0} + g_{f,1} + \tilde{g}_{f,2}$.

B.2 Initial strain hardening induced by the micro-structure

In Computational Homogenization simulations, it generally happens that, due to the heterogeneity of the micro-structure, the appearance of strain-softening in some micro-scale elements in the RVE does not suddenly lead to a strain localization of the RVE, and so the macro-scale homogenized response remains stable, showing just some strain hardening. This phenomenon coincides with the formation of micro-cracks in the RVE. Only when these micro-cracks coalesce into a single well defined macro-crack, the RVE response becomes unstable, and the macro-scale finite element eventually starts showing strain localization. However, if the 2-scale fracture energy regularization is applied from the beginning of the analysis, i.e. using a constant characteristic length $l_{dis} = \tilde{l}_{ch} = l_{ch,\mu}\frac{l_{ch,m}}{l_{ch,RVE}}$, there would be an incorrect regularization with respect to the RVE size and macro-scale finite element size, when the homogenized response is still stable and in strain-hardening. A correct implementation, instead, should be able to handle a variable characteristic length, so that $l_{dis} = l_{ch,\mu}$ is used when only micro-scale finite elements show strain-softening (micro-cracking), while $l_{dis} = \tilde{l}_{ch} = l_{ch,\mu}\frac{l_{ch,m}}{l_{ch,RVE}}$ is used when the homogenized RVE response becomes unstable (macro-cracking).

To verify this statement, five RVEs of increasing size are subjected to shear under vertical compression. Figure B.6 shows the responses obtained using a constant characteristic length equal to the size of the micro-scale finite elements. This approach, as already described in Chapter 3, works only for a standard 1-scale analysis. In a 2-scale analysis the homogenized response is objective only as far as the RVE response remains stable, then upon strain-localization of the RVE, all five responses start diverging from one another, with larger RVEs being more brittle.

Figure B.7 shows the responses obtained using the modified characteristic length according to the 2-scale fracture energy regularization proposed in Chapter 3. In this case the modified characteristic length is used from the very beginning of the analysis (i.e. also during micro-cracking before RVE localization). The post-localization response is satisfactorily objective in terms of energy dissipation, however a drawback can be noticed: the homogenized response during micro-cracking is incorrectly "over" regularized. This is a direct consequence of regularizing with respect to the RVE size and with respect to the macro-scale finite element size, while only the micro-scale finite element response is unstable (micro-cracking).

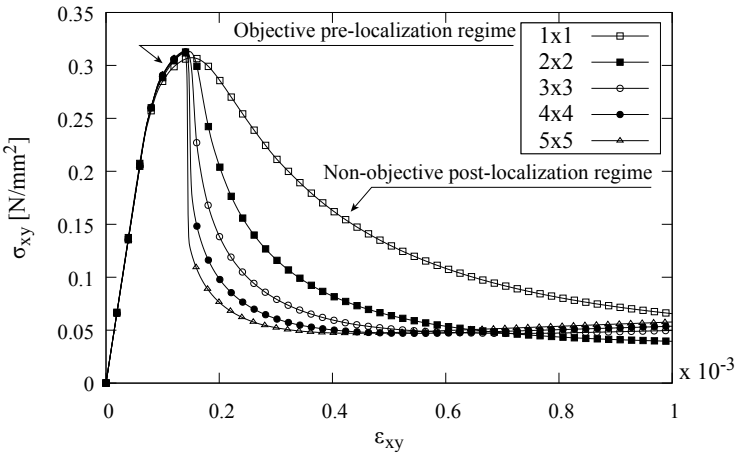

Figure B.6: Stress-strain response for different RVE sizes. Constant $l_{dis} = l_{ch,\mu}$

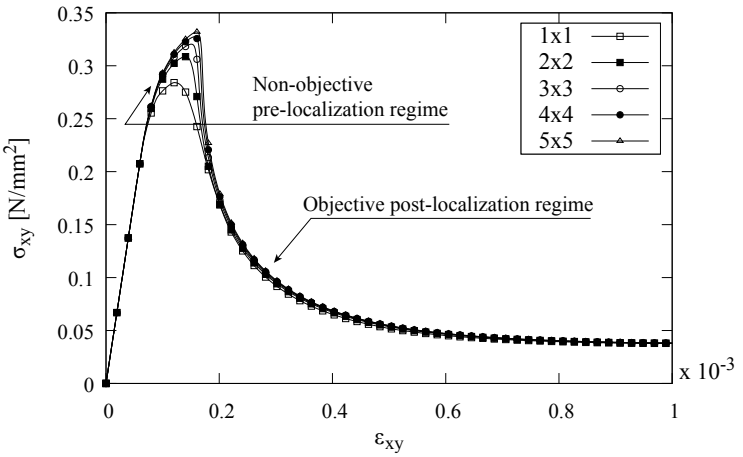

Figure B.7: Stress-strain response for different RVE sizes. Constant $l_{dis} = \tilde{l}_{ch} = l_{ch,\mu}\frac{l_{ch,m}}{l_{ch,RVE}}$

A consistent application of an adaptive characteristic length is shown in Figure B.8. In this case the analysis starts using the micro-scale finite element size as a characteristic length, and only when the entire homogenized response becomes unstable, the modified characteristic length of the 2-scale regularization proposed in Chapter 3 is used. This

shows a completely objective homogenized response, both in the pre- and in the post-peak regime.

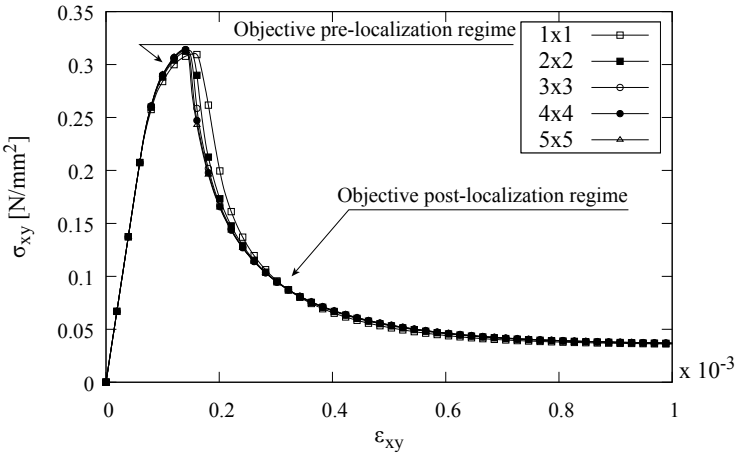

Figure B.8: Stress-strain response for different RVE sizes. Adaptive $l_{dis} = l_{ch,\mu}$ in pre-localization, $l_{dis} = \tilde{l}_{ch} = l_{ch,\mu}\frac{l_{ch,m}}{l_{ch,RVE}}$ in post-localization.

Figure B.9 shows two snapshots of the RVE state in terms of tensile damage and maximum principal strain during the homogenized strain hardening due to micro-cracking, and after the RVE localization due to the formation of an unstable macro-crack. It is evident that initially, even if all damaging mortar joints are showing strain softening (an exponential softening is used), due to the presence of strong inclusions (units), all these micro-cracks are still separated, and increasing stresses can be transferred between units, with the RVE showing a substantially uniform state of deformation. In this stage, the homogenized response is still stable under strain hardening, thus no dependency of the response on the RVE size (and so on the macro-scale finite element size) is present. Therefore the correct characteristic length to be used in the micro-constitutive laws is the characteristic length of the (locally unstable) micro-scale elements ($l_{dis} = l_{ch,\mu}$), as per standard 1-scale problems. Only when these micro-cracks join into a single macro-crack, the RVE is split into two unloading bodies, and a further localizing band. In this case an increasing stress transfer between the two parts of the RVE is not possible anymore, and the RVE homogenized response becomes unstable showing strain-softening.

It is in this stage that the homogenized response starts showing dependency on the RVE size, and consequently (instability of the homogenized response) also on the macro-scale element size. Therefore, in this post-localization stage, the correct characteristic length to be used in the micro-scale constitutive laws is the modified characteristic length of the 2-scale fracture energy regularization ($l_{dis} = \tilde{l}_{ch} = l_{ch,\mu}\frac{l_{ch,m}}{l_{ch,RVE}}$). It is obvious that this modified characteristic length should be used to regularize only the remaining part of the energy available to each micro-scale constitutive law, since a first part has already been dissipated by all damaging elements during micro-cracking.

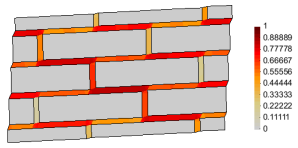

(a) d^+, pre-peak regime

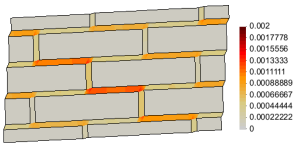

(b) $\tilde{\varepsilon}_{max,\mu}$, pre-peak regime

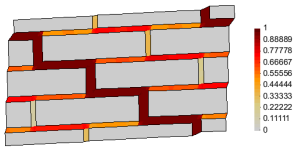

(c) d^+, post-peak regime

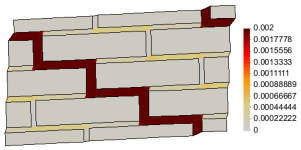

(d) $\tilde{\varepsilon}_{max,\mu}$, post-peak regime

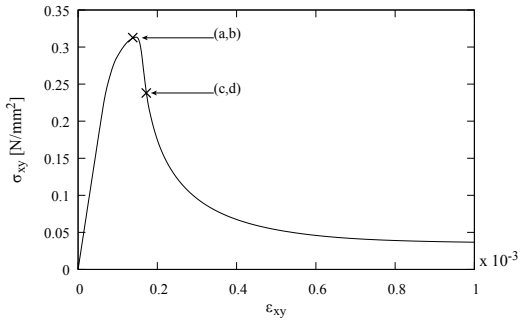

(e) homogenized stress-strain response

Figure B.9: Evolution of (a,c) tensile damage and (b,d) maximum principal strain fluctuation in a RVE subjected to shear, (a,b) before and (c,d) after localization of the homogenized response

It is clear that, in order to switch from the 1-scale to the 2-scale fracture energy regularization, the onset of strain localization in the RVE should be identified. In one-dimensional problems, strain localization happens as soon as the peak strength of the uniaxial stress-strain response is reached. However, in the general three-dimensional case, the problem is more involved, and the onset of strain localization can be obtained resorting to classical localization analysis Rizzi et al. (1995), Rudnicki and Rice (1975), Ottosen and Runesson (1991). At each iteration of the macro-scale problem, and at each point of the macro-scale domain with macro-scale strain tensor $\boldsymbol{\varepsilon}_m$, the nested RVE problem is solved. Upon RVE equilibrium, the homogenized tangent constitutive tensor $\boldsymbol{C}_{RVE,tan}(\boldsymbol{\varepsilon}_m)$ is obtained. To check whether the RVE domain is crossed by a discontinuity surface of normal vector $\boldsymbol{n}$, the following condition must be met:

$$\det\left(\boldsymbol{Q}\left(\boldsymbol{\varepsilon}_m, \boldsymbol{n}\right)\right) \leq 0 \tag{B.9}$$

where $\boldsymbol{Q}(\boldsymbol{\varepsilon}_m, \boldsymbol{n})$ is the so called *localization* or *acoustic tensor*, defined as:

$$\boldsymbol{Q}\left(\boldsymbol{\varepsilon}_m, \boldsymbol{n}\right) = \boldsymbol{n} \cdot \boldsymbol{C}_{RVE,tan}\left(\boldsymbol{\varepsilon}_m\right) \cdot \boldsymbol{n} \tag{B.10}$$

So the problem consists in finding the normal vector $\boldsymbol{n}$ which gives the minimum determinant of the acoustic tensor, and checking whether this minimum determinant is ≤ 0. Since in the computational homogenization problems a closed-form solution for the localization analysis is not available, in this work the vector $\boldsymbol{n}$, giving the minimum determinant, is sought in a discrete set of possible orientations. When the localization condition in Eq. (B.9) is met, the RVE is marked as *localized*, and the switch from 1-scale regularization to 2-scale regularization is performed.
A schematic representation of the procedure to switch from the 1-scale to the 2-scale regularization is given in Figure B.10.

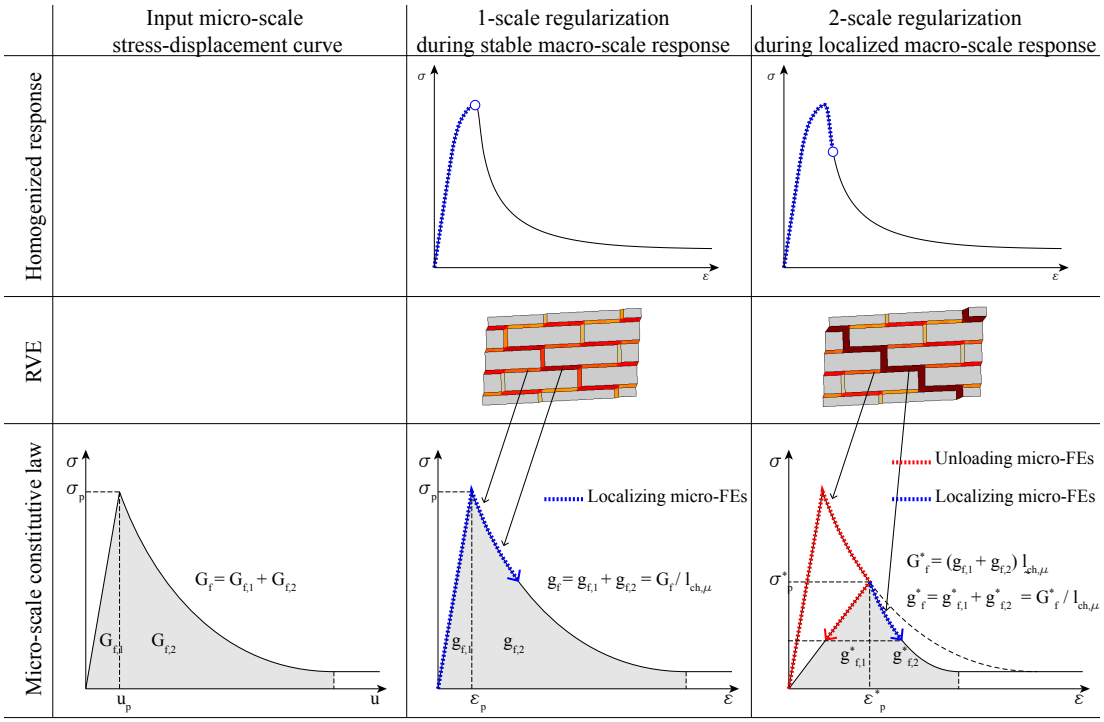

Figure B.10: Switch from 1-scale to 2-scale fracture energy regularization upon RVE localization.

Appendix C

On the choice of RVE boundary conditions

As already discussed in Chapter 3, the strain equivalence between the micro-scale and the macro-scale can be enforced by means of different boundary conditions. It is well-known that, as far as the RVE response is stable, the homogenized response of the RVE converges to the same solution as the RVE size increases. Typically the zero boundary displacement fluctuations provides an upper bound of the response, while the minimally constraint displacement fluctuations provides a lower bound. Periodic boundary conditions generally provides the best response, that is even more true when the RVE shows a real periodic micro-structure like in masonry (see Figure C.1).

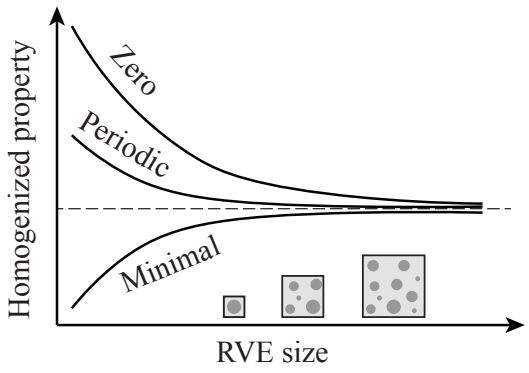

Figure C.1: Typical convergence of a homogenized property as a function of the RVE size, under different types of boundary conditions

It is also well known that when the RVE shows a softening behavior, these considerations do not hold anymore and, depending on the problem, one boundary condition may be preferred over the others. The following part of this section presents the results obtained from a study on the effects of different RVE boundary conditions. The study considers a periodic brick masonry RVE, subjected to shear under a vertical compression $\sigma_{yy} = -0.05\,\mathrm{N/mm^2}$, and zero horizontal strain $\varepsilon_{xx} = 0$. Masonry micro-structure consists of 210 mm $\times$ 52 mm $\times$ 100 mm solid bricks, and 10 mm thick mortar joints. The damage model described in Section 2.2 has been used for both bricks and mortar, and material parameters are given in Table C.1. Zero, Periodic, and Minimally Constrained boundary fluctuations are considered. For each type of boundary condition, five RVEs of increasing size (named 1×1, 2×2, 3×3, 4×4 and 5×5, see Figure C.2) are considered, in order to assess the regularization of the response upon strain localization.

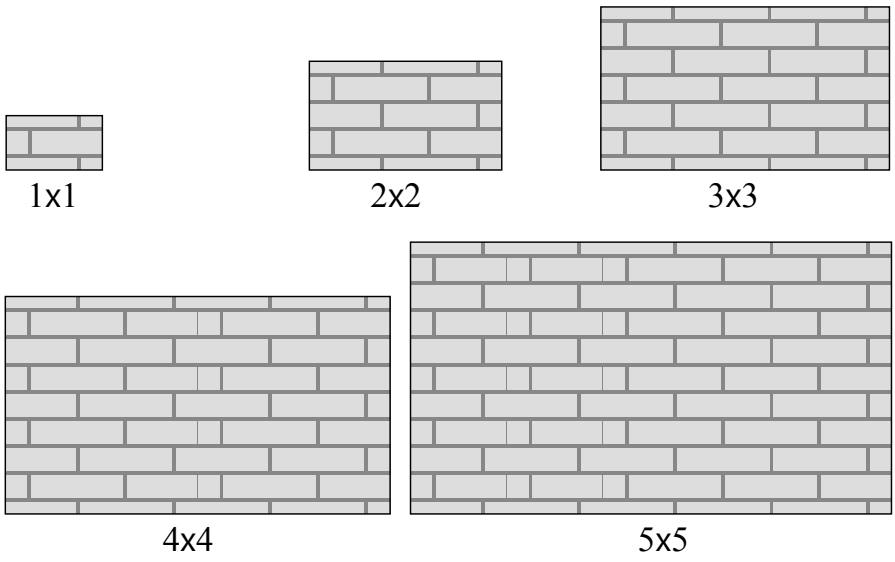

Figure C.2: Considered RVE samples of increasing size

E	ν	σ_t	G_t	σ_0	σ_p	σ_r	G_c	ε_p	k_b	k_1
850.0	0.15	0.25	0.016	8.0	10.0	1.0	6.0	0.02	1.16	0.16
$\frac{N}{mm^2}$	-	$\frac{N}{mm^2}$	$\frac{N}{mm}$	$\frac{N}{mm^2}$	$\frac{N}{mm^2}$	$\frac{N}{mm^2}$	$\frac{N}{mm}$	-	-	-

(a)

E	ν	σ_t	G_t	σ_0	σ_p	σ_r	G_c	ε_p	k_b	k_1
16700.0	0.15	2.0	0.08	8.0	11.0	1.0	6.0	0.003	1.16	0.0
$\frac{N}{mm^2}$	-	$\frac{N}{mm^2}$	$\frac{N}{mm}$	$\frac{N}{mm^2}$	$\frac{N}{mm^2}$	$\frac{N}{mm^2}$	$\frac{N}{mm}$	-	-	-

(b)

Table C.1: Material properties for mortar joints; (b) Material properties for bricks

C.1 Results for zero boundary fluctuations

The constraint of Zero Boundary Fluctuations imposes a null fluctuations on the RVE boundary, so that the total displacement field on the boundary is the linear one associated with the constant macroscopic strain field. In this way the fine-scale effect (fluctuations) are visible only at a certain distance from the boundary, being maximum at the center of the RVE. This means that with this constraint the RVE response will converge to a unique solution only for relatively large RVEs, so that the zone affected by the boundary conditions are minimal. However, with strain localization, a further issue arises. Neglecting fluctuations on the boundary prevents the strain localization band to cross the RVE boundaries (see Figure C.4). From the homogenized stress-strain curve in Figure C.3, it can be seen how the response converges very slowly to a unique solution, with considerable overestimation of both strength and dissipated energy for small-size RVEs.

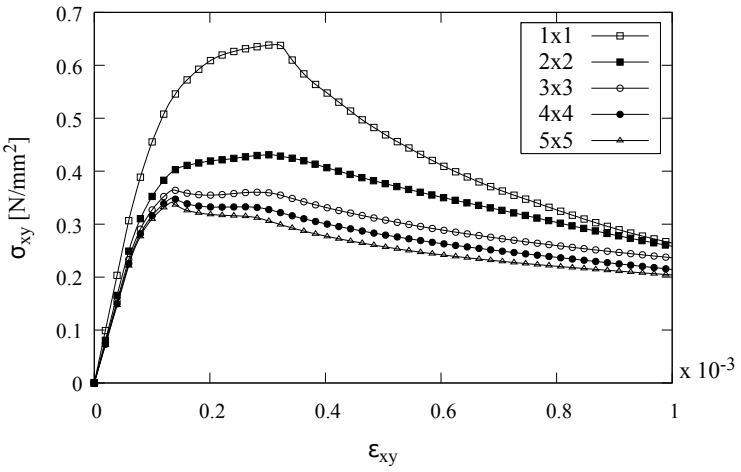

Figure C.3: Stress-strain response with Zero Boundary Fluctuations, for different RVE sizes

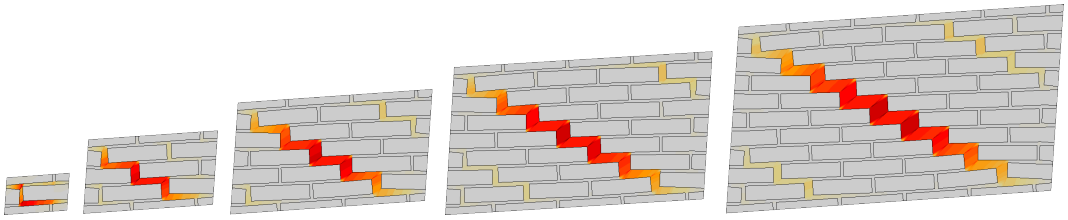

Figure C.4: Localized solution with Zero Boundary Fluctuations, for different RVE sizes

C.2 Results for periodic boundary fluctuations

The constraint of Periodic Boundary Fluctuations imposes equal fluctuations on opposite sides of the RVE, thus simulating the presence of surrounding material. The strain localization is allowed to cross the boundaries, but in a periodic way (see Figure C.6). While some authors have denoted this aspect as a drawback of this kind of boundary conditions (see Coenen et al. (2012), where a rotating periodic boundary condition has been proposed), for the type of micro-structure analyzed in this work this is not a real

issue: due to the periodic micro-structure, cracks will mainly develop along mortar joints, thus following the periodic micro-structure. Figure C.5 shows how this boundary condition provided a homogenized stress-strain response which is efficiently objective with respect to RVE size (or equivalently macro-FE size), both in terms of peak strength and dissipated energy. Note that even for small RVEs, the response rapidly converges to a unique meaningful solution. This is the main reason that led to the adoption of this boundary condition in all the analyses shown throughout this thesis.

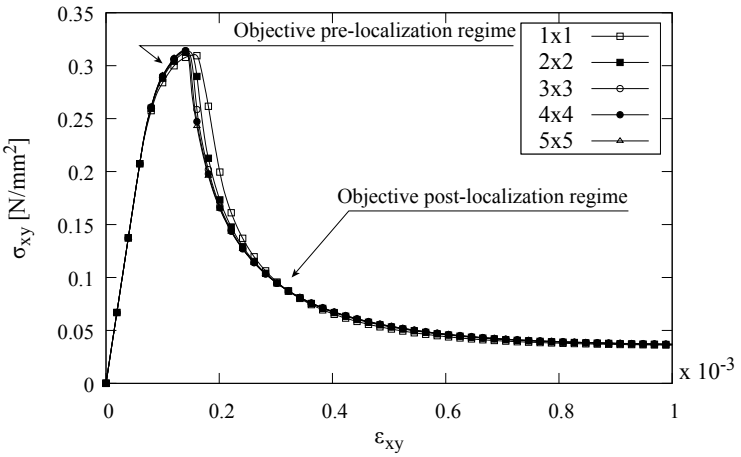

Figure C.5: Stress-strain response with Periodic Boundary Fluctuations, for different RVE sizes

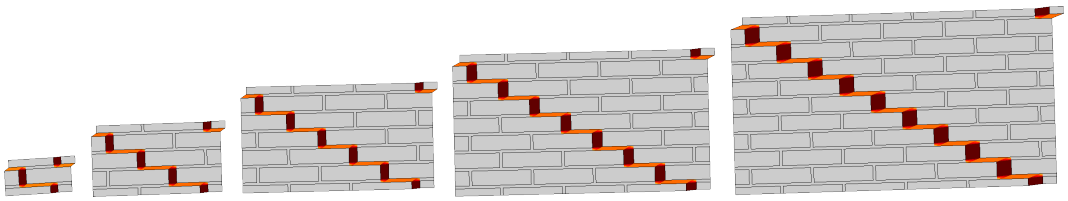

Figure C.6: Localized solution with Periodic Boundary Fluctuations, for different RVE sizes

C.3 Results for minimally constrained boundary fluctuations

The Minimally Constrained Boundary Fluctuations imposes a constraint only on the volume average of the microscopic strain field, thus providing the weakest constraint. The strain localization is allowed to cross the boundaries, not necessarily following periodic paths. However, with strain localization, this *soft* constraint may produce undesired effects of non-physical deformation modes (see Figure C.8), at least in the studied cases where a strong difference in mechanical properties of the micro-structural constituents is present. Figure C.7 shows how the pre-peak regime is very well captured and similar for all RVE sizes. This similarity is also visible in terms of dissipated energy in last part of the analysis. However, in the immediate post-peak, snap-backs appeared, and the 5x5 RVE failed to converge.

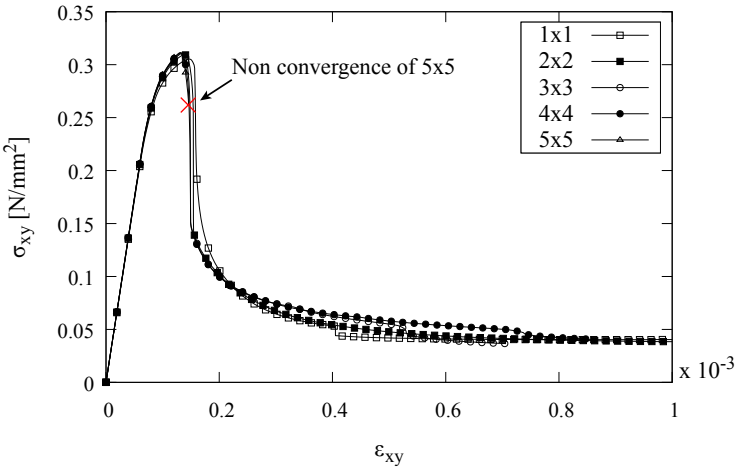

Figure C.7: Stress-strain response with Minimally Constrained Boundary Fluctuations, for different RVE sizes

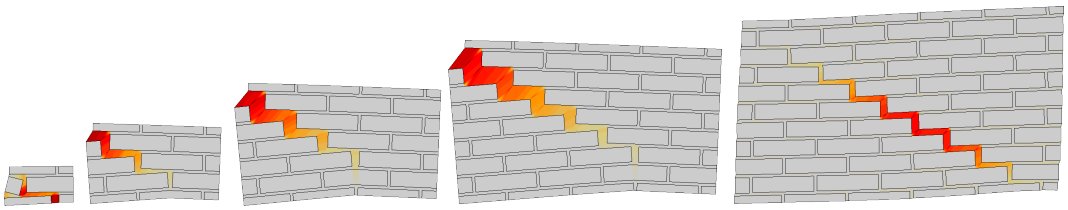

Figure C.8: Localized solution with Minimally Constrained Boundary Fluctuations, for different RVE sizes

C.4 Robustness of RVE boundary conditions with respect to strain localization

Another important criterion that has been followed in this work to assess the performance of different RVE boundary conditions, is the robustness of the response with respect to strain localization. The analyzed micro-structure is a perfectly periodic one, thus, in order to trigger strain localization, small imperfections have been used. What we expect from a robust RVE boundary condition, is to provide results that are almost insensitive to small perturbations. In the analyses presented in the previous three sections, an imperfection of 10% is applied in the center of the RVE. This represents the best case that can happen when random imperfections are used: a weakening in the center of the RVE promotes the formation of cracks from the center of the RVE, thus reducing the effects that boundary conditions have on the crack propagation. On the contrary a weakening near the boundaries should provide the worst case, maximizing the effect of boundary conditions on crack propagation.

The example shown in the previous three sections, is here re-analyzed (for the sake of conciseness only with the 3x3 RVE) to compare Periodic and Minimally Constrained Boundary Fluctuations. A bell-shaped imperfection field is applied on the RVE, with a maximum imperfection value of 10% located near the bottom-left corner, as shown in Figure C.9. This imperfection is applied to the tensile strength of each microscopic constitutive model.

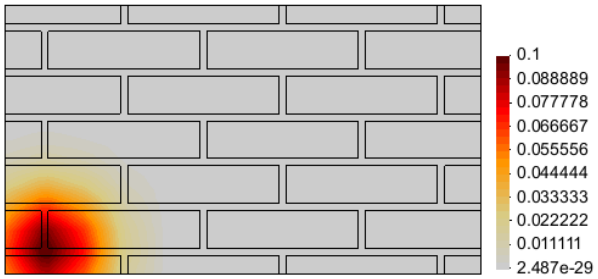

Figure C.9: Distribution of imperfection field applied to the tensile strength: $\tilde{f}_t = (1 - \text{imperfection})\, f_t$

Figure C.10 shows the obtained failure for the two RVE boundary conditions. Both of them seem to be affected by the location of the imperfection, since the crack appears at the bottom-left corner, rather than at the center of the RVE. However, periodic conditions enforce the displacement fluctuations to be the same for each periodic pair of nodes located at opposite sides, thus the same crack propagates also on the top-right part of the RVE, complementing the crack appeared at the bottom-left corner. As a result, the cumulative length of the two cracks equals the length of the crack obtained with the imperfection located at the center, and shown in Figure C.6.

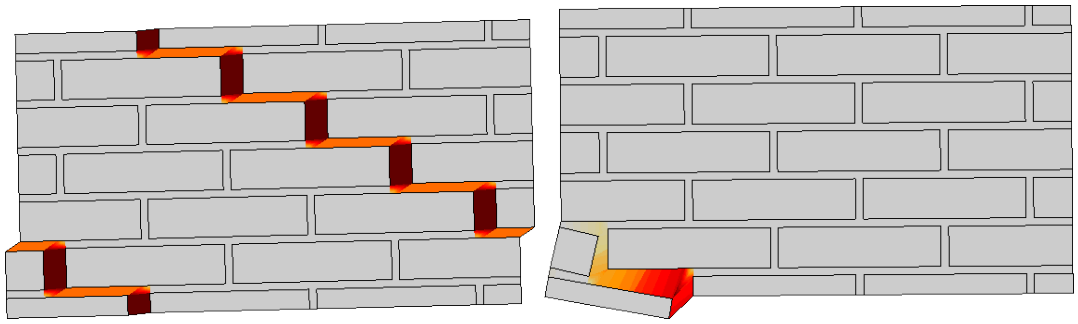

(a) (b)

Figure C.10: Obtained localized solution for (a) Periodic Boundary Fluctuations and (b) Minimally Constrained Boundary Fluctuations, with imperfection located near the bottom-left corner of the RVE.

This constraint on crack propagation is therefore beneficial for the homogenized stress-strain response, since the preservation of the total crack length guarantees (assuming that the fracture energy regularization described in Chapter 3 has been used) the same dissipation of energy, regardless of the relative position of the crack inside the RVE. Figure C.11 shows the stress-strain response of the 3x3 RVEs under Periodic and Minimally Constrained Fluctuations, with central and corner imperfections. It should be noted as Periodic Fluctuations give a homogenized response which is practically objective with respect to the location of imperfections. The same does not happen with Minimally Constrained Fluctuations, where the length of the crack is much smaller when located near the boundary, thus providing a more brittle response. These results are consistent with the formulation of the 2-scale fracture energy regularization presented in Chapter 3, where the assumption is made that the crack propagates for a length comparable to the RVE size.

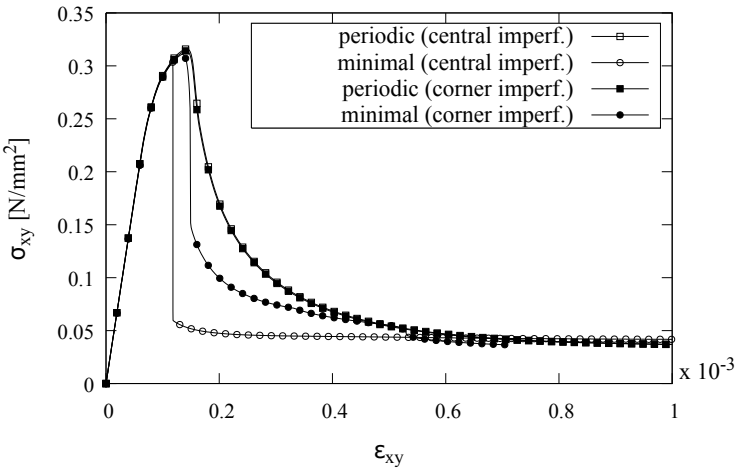

Figure C.11: Stress-strain response obtained with the imperfection located near the bottom-left corner, compared to those obtained with a central imperfection

C.5 Concluding remarks

All the results presented in this appendix, led to the adoption of periodic boundary fluctuations for all numerical examples shown throughout this work. In the specific case of the masonry micro-structure under consideration, minimally constrained boundary fluctuations show spurious localizations near the boundaries, thus providing unphysical results. It is to be noted that however this effect might be due to the high mechanical differences between mortar and units considered in this work, while these boundary conditions might provide the best response for other kind of applications. On the contrary, zero boundary displacement fluctuations show a correct prediction of the crack direction. However, due the fact that no fluctuation is allowed along the boundaries of the RVE, the crack cannot reach the boundaries. This means that these boundary conditions might be suitable for larger RVE sizes. Periodic boundary conditions show the overall best response. It is to be noted however that this is true in the present application due to the periodic micro-structure of masonry, and thus it is not a general rule.

This page is intentionally left blank

Bibliography

D. Addessi and E. Sacco. A kinematic enriched plane state formulation for the analysis of masonry panels. *European Journal of Mechanics-A/Solids*, 44:188–200, 2014.

D. Addessi, E. Sacco, and A. Paolone. Cosserat model for periodic masonry deduced by nonlinear homogenization. *European Journal of Mechanics-A/Solids*, 29(4):724–737, 2010.

R.H. Atkinson, B.P. Amadei, S. Saeb, and S. Sture. Response of masonry bed joints in direct shear. *Journal of Structural Engineering*, 115(9):2276–2296, 1989.

H.P. Backes. On the behavior of masonry under tension in the direction of the bed joints. *PhD. Thesis, Aachen University of Technology*, 1985.

H.A. Badillo. *Numerical modelling based on the multiscale homogenization theory. Application in composite materials and structures.* PhD thesis, Universitat Politécnica de Catalunya BarcelonaTech, 3 2012.

K.J. Bathe and E.N. Dvorkin. A four-node plate bending element based on mindlin/reissner plate theory and a mixed interpolation. *International Journal for Numerical Methods in Engineering*, 21(2):367–383, 2005.

Z.P. Bažant and B.H. Oh. *Crack Band Theory for Fracture of Concrete.* Bordas-Dunod, 1983.

T. Belytschko, S. Loehnert, and J.H. Song. Multiscale aggregating discontinuities: a method for circumventing loss of material stability. *International Journal for Numerical Methods in Engineering*, 73(6):869–894, 2008.

L. Benedetti, M. Cervera, and M. Chiumenti. Stress-accurate mixed fem for soil failure under shallow foundations involving strain localization in plasticity. *Computers and Geotechnics*, 64:32–47, 2015.

E. Bosco, V.G. Kouznetsova, and M.G.D. Geers. Multi-scale computational homogenization–localization for propagating discontinuities using x-fem. *International Journal for Numerical Methods in Engineering*, 102(3-4):496–527, 2015.

E. Car, F. Zalamea, S. Oller, J. Miquel, and E. Oñate. Numerical simulation of fiber reinforced composite materials—-two procedures. *International journal of solids and structures*, 39(7):1967–1986, 2002.

M. Cervera and M. Chiumenti. Mesh objective tensile cracking via a local continuum damage model and a crack tracking technique. *Computer Methods in Applied Mechanics and Engineering*, 196(1):304–320, 2006.

M. Cervera, J. Oliver, and R. Faria. Seismic evaluation of concrete dams via continuum damage models. *Earthquake engineering & structural dynamics*, 24(9):1225–1245, 1995.

M. Cervera, M. Chiumenti, and R. Codina. Mixed stabilized finite element methods in nonlinear solid mechanics. part ii: Strain localization. *Computer Methods in Applied Mechanics and Engineering*, 199(37):2571–2589, 2010a.

M. Cervera, L. Pelà, R. Clemente, and P. Roca. A crack-tracking technique for localized damage in quasi-brittle materials. *Engineering Fracture Mechanics*, 77(13):2431–2450, 2010b.

C. Citto. *Two-dimensional interface model applied to masonry structures*. ProQuest, 2008.

E.W.C. Coenen, V.G. Kouznetsova, and M.G.D. Geers. Computational homogenization for heterogeneous thin sheets. *International Journal for Numerical Methods in Engineering*, 83(8-9):1180–1205, 2010.

E.W.C. Coenen, V.G. Kouznetsova, and M.G.D. Geers. Novel boundary conditions for strain localization analyses in microstructural volume elements. *International Journal for Numerical Methods in Engineering*, 90(1):1–21, 2012.

Y. Cong, S. Nezamabadi, H. Zahrouni, and J. Yvonnet. Multiscale computational homogenization of heterogeneous shells at small strains with extensions to finite displacements and buckling. *International Journal for Numerical Methods in Engineering*, 104 (4):235–259, 2015.

G.R. Cowper. The shear coefficient in timoshenko's beam theory. *Journal of applied mechanics*, 33(2):335–340, 1966.

P. Dadvand, R. Rossi, and E. Oñate. An object-oriented environment for developing finite element codes for multi-disciplinary applications. *Archives of computational methods in engineering*, 17(3):253–297, 2010.

P. Dadvand, R. Rossi, M. Gil, X. Martorell, J. Cotela, E. Juanpere, S.R. Idelsohn, and E. Oñate. Migration of a generic multi-physics framework to hpc environments. *Computers & Fluids*, 80:301–309, 2013.

M.L. De Bellis. A cosserat based multi-scale technique for masonry structures. In *PHD Thesis*. 2009.

M.L. De Bellis and D. Addessi. A cosserat based multi-scale model for masonry structures. *International Journal for Multiscale Computational Engineering*, 9(5), 2011.

R. De Borst. The zero-normal-stress condition in plane-stress and shell elastoplasticity. *Communications in applied numerical methods*, 7(1):29–33, 1991.

E.A. De Souza Neto and R.A. Feijóo. Variational foundations of multi-scale constitutive models of solid: Small and large strain kinematical formulation. *LNCC Research and Development*, (16), 2006.

A. Drougkas, L. Pelà, and P. Roca. Numerical modelling of masonry shear walls failure mechanisms. In *Proceedings of 9th International Masonry Conference*, Guimarães, Portugal, 2014.

R.G. Drysdale, A.A. Hamid, L.R. Baker, et al. *Masonry structures: behavior and design*. Prentice Hall, 1994.

E.N. Dvorkin and K.J. Bathe. A continuum mechanics based four-node shell element for general non-linear analysis. *Engineering computations*, 1(1):77–88, 1984.

Y. Endo, L. Pelà, P. Roca, F. da Porto, and C. Modena. Comparison of seismic analysis methods applied to a historical church struck by 2009 l'aquila earthquake. *Bulletin of Earthquake Engineering*, 13(12):3749–3778, 2015.

R. Faria, J. Oliver, and M. Cervera. A strain-based plastic viscous-damage model for massive concrete structures. *International Journal of Solids and Structures*, 35(14): 1533–1558, 1998.

F. Fritzen, S. Forest, D. Kondo, and T. Böhlke. Computational homogenization of porous materials of green type. *Computational Mechanics*, 52(1):121–134, 2013.

L. Gambarotta and S. Lagomarsino. Damage models for the seismic response of brick masonry shear walls. part i: The mortar joint model and its applications. *Earthquake Engineering & Structural Dynamics*, 26(4):423–439, 1997.

H.R. Ganz and B. Thürlimann. Tests on the biaxial strength of masonry. *Rep. No. 7502*, 3, 1982.

M.G.D. Geers, V. Kouznetsova, and W.A.M. Brekelmans. Multiscale first-order and second-order computational homogenization of microstructures towards continua. *International Journal for Multiscale Computational Engineering*, 1(4), 2003.

M.G.D. Geers, E.W.C. Coenen, and V.G. Kouznetsova. Multi-scale computational homogenization of structured thin sheets. *Modelling and Simulation in Materials Science and Engineering*, 15(4):S393, 2007.

M.G.D. Geers, V.G. Kouznetsova, and W.A.M. Brekelmans. Multi-scale computational homogenization: Trends and challenges. *Journal of computational and applied mathematics*, 234(7):2175–2182, 2010.

M. Griffith and J. Vaculik. Out-of-plane flexural strength of unreinforced clay brick masonry walls. *TMS Journal*, 25(1):53–68, 2007.

R. Grytz and G. Meschke. Computational homogenization in multi-scale shell analysis at large strains. In *III European Conference on Computational Mechanics (ECCM 2006)*, page 592, 2006.

R. Guggisberg and B. Thürlimann. Experimental determination of masonry strength parameters. Technical report, Report, 1987.

A.W. Hendry. *Structural masonry*. Macmillan Education, Limited, 1990.

J.A. Hernández, J. Oliver, A.E. Huespe, and M. Caicedo. *High-Performance Model Reduction Procedures in Multiscale Simulations*. Number 127. Monograph CIMNE, 2012.

R. Hill. A self-consistent mechanics of composite materials. *Journal of the Mechanics and Physics of Solids*, 13(4):213–222, 1965.

H.K. Hilsdorf. Investigation into the failure mechanism of brick masonry loaded in axial compression. *Designing, engineering and constructing with masonry products*, pages 34–41, 1969.

P. Hofmann and S. Stockl. Tests on the shear-bond behaviour in the bed-joints of masonry. *MASONRY INT. Masonry Int.*, (9):1, 1986.

T.J.R. Hughes, G.R. Feijóo, L. Mazzei, and J.B. Quincy. The variational multiscale method-a paradigm for computational mechanics. *Computer methods in applied mechanics and engineering*, 166(1):3–24, 1998.

V. Kouznetsova, M.G.D. Geers, and W.A.M. Brekelmans. Multi-scale constitutive modelling of heterogeneous materials with a gradient-enhanced computational homogenization scheme. *International Journal for Numerical Methods in Engineering*, 54(8): 1235–1260, 2002.

V.G. Kouznetsova, M.G.D. Geers, and W.A.M. Brekelmans. Multi-scale second-order computational homogenization of multi-phase materials: a nested finite element solution strategy. *Computer Methods in Applied Mechanics and Engineering*, 193:5525–5550, 2004.

O. Lloberas-Valls. *Multiscale domain decomposition analysis of quasi-brittle materials*. PhD thesis, 2013.

O. Lloberas-Valls, D.J. Rixen, A. Simone, and L.J. Sluys. Domain decomposition techniques for the efficient modeling of brittle heterogeneous materials. *Computer Methods in Applied Mechanics and Engineering*, 200(13):1577–1590, 2011.

O. Lloberas-Valls, D.J. Rixen, A. Simone, and L.J. Sluys. Multiscale domain decomposition analysis of quasi-brittle heterogeneous materials. *International Journal for Numerical Methods in Engineering*, 89(11):1337–1366, 2012.

H.R. Lotfi and P.B. Shing. Interface model applied to fracture of masonry structures. *Journal of structural engineering*, 120(1):63–80, 1994.

P.B. Lourenço. *Computational strategies for masonry structures*. PhD thesis, TU Delft, Delft University of Technology, 1996.

P.B. Lourenço and J.G. Rots. Multisurface interface model for analysis of masonry structures. *Journal of engineering mechanics*, 123(7):660–668, 1997.

J. Lubliner, J. Oliver, S. Oller, and E. Oñate. A plastic-damage model for concrete. *International Journal of solids and structures*, 25(3):299–326, 1989.

F. Lurati, H. Graf, and B. Thürlimann. Experimental determination of the strength parameters of concrete masonry. *Rep. No. 8401*, 2, 1990.

J. Mandel. *Plasticité classique et viscoplasticité*. Springer-Verlag, 1971.

T.J. Massart. Multi-scale modeling of damage in masonry structures. 2003.

T.J. Massart, R.H.J. Peerlings, and M.G.D. Geers. An enhanced multi-scale approach for masonry wall computations with localization of damage. *International Journal for Numerical Methods in Engineering*, 69(5):1022–1059, 2007.

A. Melendo, A. Coll, M. Pasenau, E. Escolano, and A. Monros. www.gidhome.com, 2015. [Online; accessed Nov-2015].

B.C.N. Mercatoris and T.J. Massart. A coupled two-scale computational scheme for the failure of periodic quasi-brittle thin planar shells and its application to masonry. *International journal for numerical methods in engineering*, 85(9):1177–1206, 2011.

B.C.N. Mercatoris, Ph. Bouillard, and T.J. Massart. Multi-scale detection of failure in planar masonry thin shells using computational homogenisation. *Engineering fracture mechanics*, 76(4):479–499, 2009.

C. Miehe, J. Schröder, and J. Schotte. Computational homogenization analysis in finite plasticity simulation of texture development in polycrystalline materials. *Computer methods in applied mechanics and engineering*, 171(3):387–418, 1999.

V.P. Nguyen, M. Stroeven, and L.J. Sluys. Multiscale continuous and discontinuous modeling of heterogeneous materials: A review on recent developments. *Journal of Multiscale Modelling*, 3(04):229–270, 2011.

D.V. Oliveira and P.B. Lourenço. Implementation and validation of a constitutive model for the cyclic behaviour of interface elements. *Computers & structures*, 82(17):1451–1461, 2004.

J. Oliver. A consistent characteristic length for smeared cracking models. *International Journal for Numerical Methods in Engineering*, 28(2):461–474, 1989.

J. Oliver, M. Caicedo, E. Roubin, J.A. Hernández, and A. Huespe. Multi-scale (fe2) analysis of material failure in cement/aggregate-type composite structures. *Computational Modelling of Concrete Structures*, page 39, 2014a.

J. Oliver, M. Caicedo, E. Roubin, A.E. Huespe, et al. Continuum approach to computational multi-scale modeling of fracture. *Key engineering materials*, 627:349–352, 2014b.

J. Oliver, I.F. Dias, and A.E. Huespe. Crack-path field and strain-injection techniques in computational modeling of propagating material failure. *Computer Methods in Applied Mechanics and Engineering*, 274:289–348, 2014c.

S. Oller. *Fractura Mecánica: Un Enfoque Global*. Ediciones CIMNE y UPC, 2001.

S. Oller, J. Miquel Canet, and F. Zalamea. Composite material behavior using a homogenization double scale method. *Journal of Engineering mechanics*, 131(1):65–79, 2005.

J.M. Ortolano, J.A. Hernández, and J. Oliver. *A Comparative Study on Homogenization Strategies for Multi-Scale Analysis of Materials*. Number 135. Monograph CIMNE, 2013.

F. Otero, X. Martínez, S. Oller, and O. Salomón. Study and prediction of the mechanical performance of a nanotube-reinforced composite. *Composite Structures*, 94:2920–2930, 2012.

F. Otero, S. Oller, X. Martinez, and O. Salomón. Numerical homogenization for composite materials analysis. comparison with other micro mechanical formulations. *Composite Structures*, 122:405–416, 2015.

N.S. Ottosen and K. Runesson. Properties of discontinuous bifurcation solutions in elasto-plasticity. *International Journal of Solids and Structures*, 27(4):401–421, 1991.

A.W. Page. Finite element model for masonry. *Journal of the Structural Division*, 104 (8):1267–1285, 1978.

A.W. Page. The biaxial compressive strength of brick masonry. 1981.

A.W. Page. A model for the in-plane behaviour of masonry and a sensitivity analysis of its critical parameters. In *Proc. 5 th Int. Brick Masonry Conf.(VIBMaC) held in Washington, DC, 5-10 Oct., 1979. Edited by J. A. Wintz and A. H. Yorkdale. McLean, Virginia*, page 262, 1982.

A.W. Page. The strength of brick masonry under biaxial tension-compression. *Int. J. Masonry Constr*, 3(1):26–31, 1983.

L. Pelà. *Continuum damage model for nonlinear analysis of masonry structures.* PhD thesis, Università degli studi di Ferrara, 2009.

L. Pelà, M. Cervera, and P. Roca. Continuum damage model for orthotropic materials: Application to masonry. *Computer Methods in Applied Mechanics and Engineering*, 200(9-12):917–930, 2011.

L. Pelà, M. Cervera, and P. Roca. An orthotropic damage model for the analysis of masonry structures. *Construction and Building Materials*, 41:957–967, 2013.

L. Pelà, J. Bourgeois, P. Roca, M. Cervera, and M. Chiumenti. Analysis of the effect of provisional ties on the construction and current deformation of mallorca cathedral. *International Journal of Architectural Heritage*, (just-accepted), 2014a.

L. Pelà, M. Cervera, S. Oller, and M. Chiumenti. A localized mapped damage model for orthotropic materials. *Engineering Fracture Mechanics*, 124-125:196–216, 2014b.

M. Petracca, L. Pelà, R. Rossi, S. Oller, G. Camata, and E. Spacone. Regularization of first order computational homogenization for multiscale analysis of masonry structures. *Computational Mechanics*, 57(2):257–276, 2016.

R. Van Der Pluijm. Shear behavior of bed joints. *Proc. 6 th North American Masonry Conf.*, pages 125–136, 1993.

R. Van Der Pluijm. Overview of deformation controlled combined tensile and shear tests. *Rep. tue/cco/98.20, Eindhoven Univ. of Technology, Eindhoven, The Netherlands*, 1998.

R.D. Quinteros, S. Oller, and L.G. Nallim. Nonlinear homogenization techniques to solve masonry structures problems. *Composite Structures*, 94(2):724–730, 2012.

M.L. Raffa, F. Lebon, E. Sacco, and H. Welemane. A multi-level interface model for damaged masonry. In (Editors) B.H.V. Topping, P. Iv/'anyi, editor, *"Proceedings of the Fourteenth International Conference on Civil, Structural and Environmental Engineering Computing"*, Civil-Comp Press, Stirlingshire, UK, 2013.

T.M.J. Raijmakers and A.Th. Vermeltfoort. *Deformation controlled tests in masonry shear walls: report B-92-1156.* 1992.

E. Rizzi, I. Carol, and K. Willam. Localization analysis of elastic degradation with application to scalar damage. *Journal of Engineering Mechanics*, 121(4):541–554, 1995.

P. Roca, M. Cervera, G. Gariup, and L. Pelà. Structural analysis of masonry historical constructions. classical and advanced approaches. *Archives of Computational Methods in Engineering*, 17(3):299–325, 2010.

P. Roca, M. Cervera, L. Pelà, R. Clemente, and M. Chiumenti. Viscoelasticity and damage model for creep behavior of historical masonry structures. *Open Civ Eng J*, 6:188–199, 2012.

P. Roca, M. Cervera, L. Pelà, R. Clemente, and M. Chiumenti. Continuum fe models for the analysis of mallorca cathedral. *Engineering structures*, 46:653–670, 2013.

J.G. Rots. *Computational modeling of concrete fracture.* PhD thesis, Technische Hogeschool Delft, 1988.

J.W. Rudnicki and J.R. Rice. Conditions for the localization of deformation in pressure-sensitive dilatant materials. *Journal of the Mechanics and Physics of Solids*, 23(6): 371–394, 1975.

E. Sacco and J. Toti. Interface elements for the analysis of masonry structures. *International Journal for Computational Methods in Engineering Science and Mechanics*, 11(6):354–373, 2010.

S. Saloustros, L. Pelà, and M. Cervera. A crack-tracking technique for localized cohesive-frictional damage. *Engineering Fracture Mechanics*, 150:96–114, 2015a.

S. Saloustros, L. Pelà, P. Roca, and J. Portal. Numerical analysis of structural damage in the church of the poblet monastery. *Engineering Failure Analysis*, 48:41–61, 2015b.

W. Samarasinghe and A.W. Hendry. The strength of brickwork under biaxial tensile and compressive stress. In *Proc. Br. Ceram. Soc.*, number 30, page 129, 1982.

J.C. Simo and M.S. Rifai. A class of mixed assumed strain methods and the method of incompatible modes. *International Journal for Numerical Methods in Engineering*, 29 (8):1595–1638, 1990.

P. Trovalusci and R. Masiani. Non-linear micropolar and classical continua for anisotropic discontinuous materials. *International Journal of Solids and Structures*, 40(5):1281–1297, 2003.

G. van Zijl. Modeling masonry shear-compression: Role of dilatancy highlighted. *Journal of engineering mechanics*, 130(11):1289–1296, 2004.

J.Y. Wu, J. Li, and R. Faria. An energy release rate-based plastic-damage model for concrete. *International Journal of Solids and Structures*, 43(3):583–612, 2006.

A. Zucchini and P.B. Lourenço. A micro-mechanical model for the homogenisation of masonry. *International Journal of Solids and Structures*, 39(12):3233–3255, 2002.

A. Zucchini and P.B. Lourenço. A micro-mechanical homogenisation model for masonry: Application to shear walls. *International Journal of Solids and Structures*, 46(3):871–886, 2009.